

## Selective integrin targeting with DNA-based nanomaterials

Présentée le 7 octobre 2022

Faculté des sciences et techniques de l'ingénieur  
Laboratoire des biomatériaux programmables  
Programme doctoral en science et génie des matériaux

pour l'obtention du grade de Docteur ès Sciences

par

**Eva Eugene KURISINKAL**

Acceptée sur proposition du jury

Prof. H. Frauenrath, président du jury  
Prof. M. M. C. Bastings, directrice de thèse  
Prof. R. Jungmann, rapporteur  
Prof. M. Tibbitt, rapporteur  
Prof. A. Boghossian, rapporteuse

# Acknowledgments

I would like to express my gratitude to my thesis director, Prof. Maartje Bastings for giving me the opportunity to pursue my Ph.D. in her laboratory. I have relished the opportunity in the setting up the laboratories, projects, and team alongside researching the spatial targeting of integrins.

I would like to thank my thesis committee members Prof. Holger Frauenrath, Prof. Ardemis Boghossian, Prof. Ralf Jungmann, and Prof. Mark Tibbitt for their time and feedback in evaluating my thesis. Thank you to Prof. Martin Weigert for your input on image processing. I also want to thank the staff at BIOP EPFL who have made a lot of this work possible.

To Dr. Uwe Hahn, thank you for mentoring and guiding me towards research. I highly value your tutelage and appreciate the change you have catalysed in my life.

Dear Drs. Hale and Jose Bila, and Daniela Sequeira, it has been a pleasure to grow alongside you and I look forward to better things to come.

I would like to convey my appreciation to my fellow PBL members, for accompanying me on this journey. It has been a great pleasure across work and otherwise. Special mention to Vincenzo Caroprese for the thorough discussions and support throughout these years. Our battle of the languages is far from over. A huge thank you to Kaltrina Paloja, especially for the support during my period of injury. I will fondly remember our antics. Дуже дякую to Artem Kononenko for your scientific support and for teaching me about your beautiful culture. To the ideal officemate, Cem Tekin I have and will always appreciate your timely humour. To Olivia Courbot, it was a pleasure mentoring you and working alongside you in the laboratory. I wish you success in your future endeavours. To Luca Montanelli, thank you for coming on board my project and for the work you have done. I would like to also thank Dr. Marianna Koga and Dr. Diana Morzy for the collaboration and in keeping my spirits and momentum high during the last leg. Thank you to Hugo Rodriguez, Filippo Ceccon, Dr. Joreike Weiden, Wong Siu Ho, Christine Lavanchy, and Eulalia Durussel who have contributed to a pleasant working environment (not forgetting the pranks!) these past years.

I would like to thank fellow colleagues and mentors (past and present) who have journeyed with me, Michael Kessler, Yevhen Hryshunin, Andrea Muchietto, Dr. Akshay Balgarkashi, Dr. Simon Escobar, Andrea Guinto, Dr. Vivek Ramachandran, Enrico Ajanic, Dr. H el ene Chassin, David Fuchs, Kevin Sebastiaan Hof, Dr. Stefano Vianello and Dr. Corey Stevens. To Dr. Aleksandrs

Leitis, thank you for the discussions and for imparting your knowledge to me. Also, thank you to the members of BIOS and SMaL for including me in your activities.

My heartfelt thanks to Valentin Wüest for being an awesome housemate, also for bearing the lockdown and more with me. Also, I would like to thank Marcelo Gonzalez, Eléonore Wild, Samuel Gomez, Eriks Kletnieks and Klaudija Gauja for the great company, food, and sporting activities. I'm especially grateful for my friends, Joachim Goh, Victor Seow, Julian Seow, Sashi Kumar, Daniel Luke, Jeremy Fong, Ryan Stanley, and Isaac Culas for keeping me afloat and awake at all hours due to time differences in our respective locations. You have always kept me in high spirits!

Most importantly, thanks to my family, especially my grandparents Manuel Corea, Teresa Francis, Pius Kurisinkal, Mariamma Achankunju, Celine Francis and Joseph Velieth, parents Eugene Kurisinkal and Emilda Corea, and sisters, Emma and Erica for supporting me throughout the years. Special thanks to my Grand Uncle "Chacha" Rt. Rev. Dato' Seri Sebastian Francis, D.D., D.G.P.N., D.S.P.N., godfather Reynolds Corea, Uncle Shashithran Raman, Aunt Jo-anne Joseph, Aunt Priya Corea, Uncle Dr. Gerard Meachery and Aunt Dr. Gráinne Gorman for supporting and guiding my education. I could not have made it this far without all of you.

## Abstract

Targeting cells specific to type and state remains a challenge in developing effective therapies, sensitive diagnostics, also robust and versatile tissue engineering. A promising strategy is to focus on improving the inherent selectivity of the targeting system through precise orchestration of ligand-receptor interactions. Integrin receptors present themselves as a strategic target as their expression has been reported to be regulated across cell types and states. The principle of super-selectivity permits the selective targeting of integrin receptors above a threshold concentration in high valency and relative low affinity systems, leaving sparser counterparts unaffected. Here, we demonstrate that DNA based scaffolds with rigid ligand nanoscale spatial presentation can be designed to discriminate between adhesions by varying RGD ligand spacing targeting integrin  $\alpha_5\beta_1$  receptors. We begin by modelling integrin  $\alpha_5\beta_1$  receptors nearest neighbour distributions across HUVEC, CHO and HeLa cells. Targeting spacings in the sub-60nm reveal trends in binding efficacies based on cell type and activation state. An ensuing study of HUVEC response to local ligand geometries of varying global inter-geometry spacings presented on higher valency DNA scaffolds randomly immobilised result in two distinct adhesion cluster formations. Our findings open avenues in the design of super-selective targeting elements, besides providing insight on the regulation of integrin receptors on the cell surface across different cell types. Parameters for ligand presentation at the sub-adhesion scale affords selective cell engagement in biomaterial presentation.

### Keywords:

Integrins  $\alpha_5\beta_1$ , multivalency, spacing, selectivity, RGD, cell adhesion, DNA nanomaterials

## Résumé

Le ciblage des cellules spécifiques au type et à l'état reste un défi dans le développement de thérapies efficaces, de diagnostics sensibles, ainsi que d'une ingénierie tissulaire robuste et polyvalente. Une stratégie prometteuse consiste à se concentrer sur l'amélioration de la sélectivité inhérente du système de ciblage grâce à une orchestration précise des interactions ligand-récepteur. Selon les études, les récepteurs d'intégrine se présentent comme une cible stratégique car il leur expression est régulée à travers les types et les états cellulaires. Le principe de super-sélectivité permet le ciblage sélectif des récepteurs d'intégrine au-dessus d'un seuil de concentration dans des systèmes de valence élevée et d'affinité relativement faible, laissant les homologues plus clairsemés non affectés. Ici, nous démontrons que les plateformes à base d'ADN avec une présentation spatiale à l'échelle nanométrique du ligand rigide peuvent être conçus pour faire la distinction entre les adhérences en faisant varier l'espacement des ligands RGD ciblant les récepteurs de l'intégrine  $\alpha_5\beta_1$ . Nous commençons par modéliser les distributions des récepteurs les plus proches voisins de l'intégrine  $\alpha_5\beta_1$  dans les cellules HUVEC, CHO et HeLa. Les espacements de ciblage dans les sous-60 nm révèlent des tendances dans les efficacités de liaison en fonction du type de cellule et de l'état d'activation. Une étude de la réponse HUVEC aux géométries de ligands locaux d'espacements inter-géométrie globaux variables présentés sur des plate-forme polyvalente d'AND immobilisés au hasard aboutit à deux formations de clusters d'adhérence distinctes. Nos découvertes ouvrent des voies dans la conception d'éléments de ciblage super sélectifs, en plus de fournir un aperçu de la régulation des récepteurs d'intégrine à la surface cellulaire dans différents types de cellules. Les paramètres de présentation du ligand à l'échelle de la sous-adhésion permettent un engagement cellulaire sélectif lors de la présentation du biomatériau.

### Mots-clés:

Intégrine  $\alpha_5\beta_1$ , multivalence, espacement, sélectivité, RGD, adhésion cellulaire, Nanomatériaux d'ADN

# Table of Contents

<b>Abstract</b> .....	<b>i</b>
<b>Résumé</b> .....	<b>iv</b>
<b>Table of Figures</b> .....	<b>viii</b>
<b>Table</b> .....	<b>ix</b>
<b>Abbreviations</b> .....	<b>x</b>
<b>Chapter 1      Introduction &amp; motivation</b> .....	<b>1</b>
1.1 Introduction .....	1
1.2 Multivalency & Super-selectivity .....	9
1.3 RGD peptides as ligands .....	10
1.4 DNA nanotechnology .....	10
1.5 Motivation and Outline .....	12
1.6 Bibliography .....	13
<b>Chapter 2      Characterisation of integrin <math>\alpha_5\beta_1</math> expression &amp; distribution</b> .....	<b>19</b>
2.1 Introduction .....	19
2.2 Methods and materials.....	21
2.3 Cell binding assay .....	21
2.3 Integrin $\alpha_5\beta_1$ activation.....	22
2.4 Integrin $\alpha_5\beta_1$ activation with monoclonal antibody SNAKA51 and Mn <sup>2+</sup> .....	22
2.5 Integrin $\alpha_5\beta_1$ activation via DTT disulfide bond reduction of cysteine-rich domain	23
2.6 Integrin $\alpha_5\beta_1$ activation analysis .....	23
2.7 Conclusions .....	32
2.8 Appendix.....	33
2.9 Bibliography .....	38
<b>Chapter 3      Selective integrin <math>\alpha_5\beta_1</math> targeting with rigid DNA scaffolds</b> .....	<b>42</b>
3.1 Introduction .....	43
3.2 Methods and materials.....	43
3.3 Monovalent RGD Binding Assay .....	50
3.4 Bivalent Scaffold.....	52
3.5 Multivalent, Rigid Scaffold.....	60

---

3.6	Conclusions .....	62
3.7	Appendix.....	63
3.8	Bibliography .....	65
<b>Chapter 4</b>	<b>Cell response to RGD-liganded rigid, multivalent DNA scaffolds .....</b>	<b>69</b>
4.1	Introduction .....	69
4.2	Methods and materials.....	71
4.3	HUVEC adhesion to RGD liganded Multivalent Scaffolds .....	73
4.4	Conclusions .....	83
4.5	Appendix.....	85
4.6	Bibliography .....	86
<b>Chapter 5</b>	<b>Conclusions &amp; Outlook.....</b>	<b>90</b>
5.1	Conclusions of this Thesis .....	90
5.2	Discussion and Future Directions .....	91
5.3	Bibliography .....	94
<b>Curriculum Vitae</b>	<b>.....</b>	<b>96</b>

# Table of Figures

Figure 1.1 Active targeting directly engaging markers on tumour cells to deliver therapies. ....	1
Figure 1.2 Integrin signalling and family .....	2
Figure 1.3 Integrin $\alpha_5\beta_1$ structure and conformation .....	4
Figure 1.4 Integrin $\alpha_5\beta_1$ activation methods .....	6
Figure 1.5 Integrin $\alpha_5\beta_1$ binding and clustering .....	7
Figure 1.6 DNA origami Disk with two faces for label attachment.....	11
Figure 2.1 Chapter overview .....	20
Figure 2.2 Methods for integrin activation. ....	24
Figure 2.3 Analysis of integrin $\alpha_5\beta_1$ receptor on HUVEC, CHO and HeLa in “chased” versus resting conditions .....	27
Figure 2.4 SNAKA51 antibody calibration for receptor concentration.....	29
Figure 2.5 Workflow in modelling integrin $\alpha_5\beta_1$ receptors distributions in HUVEC, CHO and HeLa.....	30
Figure 2.6 Confocal microscopy analysis of spatially constrained integrin staining.....	31
Figure 3.1 Chapter overview .....	42
Figure 3.2 Monovalent RGD-CF488 characterisation.....	51
Figure 3.3 Monovalent RGD-CF488 binding concentration regime in HUVEC. ....	51
Figure 3.4 1mM monovalent RGD-CF488 binding to HUVEC, CHO and HeLa .....	52
Figure 3.5 Bivalent scaffolds for binding assays .....	53
Figure 3.6 AFM images of Bivalent-24, Bivalent-36 and Bivalent-Flex.....	54
Figure 3.7 Material characterisation .....	55
Figure 3.8 PAGE characterisation of Bivalent liganded Scaffolds .....	56
Figure 3.9 Bivalent-24-RGD binding on HUVEC in the micromolar regime..	57
Figure 3.10 Confocal microscopy analysis of spatially constrained integrin staining.....	58
Figure 3.11 Multivalent, Rigid, Scaffold.....	60
Figure 3.12 Multivalent Scaffold characterisation.....	61



Figure 3.13 HUVEC staining with Multivalent Scaffolds .....	61
Figure 4.1 Chapter overview. ....	70
Figure 4.2 Top : Multivalent Scaffold ligand geometries and spacings. ....	74
Figure 4.3 Surface immobilisation of RGD-liganded Multivalent Scaffolds.....	75
Figure 4.4 Focal adhesion markers employed .....	76
Figure 4.5 Adhesion marker (integrin $\alpha_5\beta_1$ , talin, f-actin, nucleus) staining of HUVECs adhering to Mono-1-RGD, Multi-3-7-RGD and Multi-3-25-RGD. ....	77
Figure 4.6 Adhesion marker (integrin $\alpha_5\beta_1$ , talin, F-actin, nucleus) staining of HUVECs adhering to Multi-6-7-RGD and Multi-6-20-RGD.....	78
Figure 4.7 Adhesion marker (integrin $\alpha_5\beta_1$ , talin, F-actin, nucleus) staining of HUVECs adhering to Multi-36-7-RGD .....	79
Figure 4.8 Depiction of adhesion cluster formation upon integrin $\alpha_5\beta_1$ receptor binding to different local ligand geometries and global spacings.....	81
Figure 4.9 Calculated minimum inter-ligand geometry spacings for the respective Multivalent Scaffolds.....	84
Figure 5.1 Expanding Multivalent Scaffold assays. ....	93

Figures were created in BioRender.com (2022).

## Tables

Table 1 Analysis of adhesion markers of HUVECs adhering to RGD-liganded Multivalent Scaffolds .....	80
---	----

# Abbreviations

AFM	atomic force microscopy
AGE	agarose gel electrophoresis
CHO	Chinese hamster ovary cells
DBCO	dibenzocyclooctyne
DNA	deoxyribonucleic acid
dsDNA	double-stranded deoxyribonucleic acid
DTT	dithiothreitol
ECM	extracellular matrix
ESI-MS	electrospray ionization mass spectrometry
FA	focal adhesion
FN	fibronectin
HeLa	Henrietta Lack's epithelial adenocarcinoma cells
HUVEC	human umbilical vein endothelial cells
NP	nanoparticle
PAGE	polyacrylamide gel electrophoresis
PEG	polyethylene glycol
RP-HPLC	Reversed-Phase High-Performance Liquid Chromatography
ssDNA	single-stranded deoxyribonucleic acid

# Chapter 1 Introduction & motivation

## 1.1 Introduction

### 1.1.1 Integrins for active targeting

A significant hurdle in the administration of therapies, in particular in combatting infections, cancers and genetic diseases, is in the specific delivery of the therapeutic agent to targeted elements of an organ, tissue or cell type, i.e. active targeting.<sup>1</sup> Whilst active targeting engages the tumour cells directly, passive targeting capitalises on the enhanced retention of targeting elements in the tumour microenvironment, Figure 1.1.<sup>2</sup> Cell receptors are often employed as targeted elements due to varying expression dependent on cell/tissue type and accessibility for binding.<sup>3</sup>

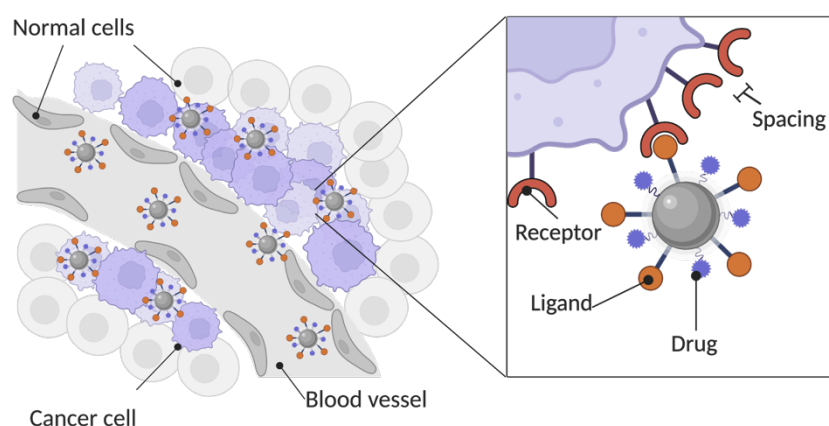


Figure 1.1 Active targeting directly engaging markers on tumour cells to deliver therapies.

Prime candidates amongst cell receptors are integrin transmembrane receptors, reportedly differently regulated in diseases.<sup>4-6</sup> Integrins are bi-directional signalling receptors between the cell and its' extracellular environment, Figure 1.2 (Left), also mediating migration, proliferation and differentiation. The 18  $\alpha$  and 8  $\beta$  integrin subunits associate forming 24 heterodimers that cluster with functional and tissue specificity, Figure 1.2 (Right).<sup>7,8</sup> In general, integrins cluster and interact with the extracellular matrix and the actin cytoskeleton within sites termed focal adhesions (FAs).<sup>9</sup> Here, they anchor cells to the external environment and transmit information across the plasma membrane.<sup>10</sup> In addition, integrins subtypes possess orthogonal functionality that arises from their multiple activation states and propensity in binding specific ligands (short recognition motifs of amino acids) found on proteins of the extracellular matrix (ECM).<sup>11</sup> As such, integrins are spatially regulated and have the capacity to respond to changes in the extracellular environment and transduce such changes to the intracellular environment.<sup>12-15</sup> The increased selectivity in the targeting of cell receptors also promises to shed light on the mechanisms involved in cellular

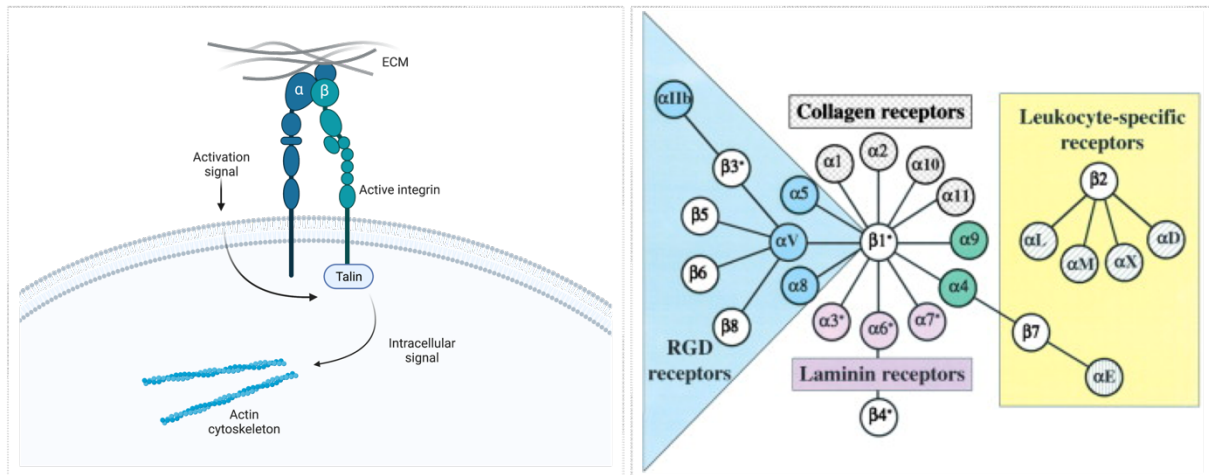


Figure 1.2 Integrin signalling and family. Left : Integrin signalling upon ECM activation. Right : Integrin family classified according to subtype from Hynes.<sup>7</sup>

signalling, the key to triggering specific cellular responses.<sup>16,17</sup> The lack of selectivity in the targeting of cell receptors on the other hand, leads to poor cell differentiation, misdiagnosis from false positive testing, as well as toxicity and side-effects from inefficient and/or off-targeted drug delivery systems.<sup>1,18</sup>

### 1.1.2 Integrins $\alpha_5\beta_1$

The expression of integrins, whilst ubiquitous, is cell-type dependent with respect to the individual heterodimers and accounts for heterodimer function.<sup>19–21</sup> For instance, the integrin  $\alpha_5\beta_1$  has been implicated in several diseases<sup>6</sup> ranging from cancer,<sup>5</sup> cardiac pathophysiology<sup>22,23</sup>, inflammation<sup>21,24</sup>, respiratory diseases,<sup>25</sup> neurological disorders<sup>26</sup> and viruses including ebola<sup>27</sup> and SARS-CoV-2<sup>28</sup> besides being engaged in cell adhesion.<sup>8,29</sup> With respect to types of cancer, the altered expression of the integrin  $\alpha_5\beta_1$ <sup>5,30,31</sup> is linked to poor prognosis for patients with colon,<sup>32–34</sup> breast,<sup>35</sup> ovarian,<sup>36</sup> lung,<sup>37,38</sup> brain<sup>31</sup> and chemotherapeutic resistance and recurrence in cervical cancer.<sup>39,40</sup>

As for cell adhesion, the integrin  $\alpha_5\beta_1$  serves an important role in endothelial cell proliferation and angiogenesis; as such has marked expression levels on endothelial cells.<sup>41</sup> Whilst epithelial cells express high levels of the  $\beta_1$  integrins, the integrin  $\alpha_5\beta_1$  is expressed in lower proportions in comparison due to epithelial basement membrane ECM protein composition.<sup>19,42,43</sup> Of note, upregulation of integrin  $\alpha_5\beta_1$  expression in epithelia is associated with inflammation<sup>25,43,44</sup> and active proliferation.<sup>45</sup> Meanwhile, changes in the polarisation of epithelial integrin expression is reported in transformation from normal to malignant states.<sup>43</sup> Integrin  $\alpha_5\beta_1$  expression on the cell surface versus relocation to the cell interior of fibroblasts have also been implicated in resisting cancer progression.<sup>46</sup> Duly, integrin  $\alpha_5\beta_1$  has been proposed as targets for anti-angiogenic therapies due to its' role in tumour angiogenesis.<sup>47</sup> Altogether, the selective engagement of the integrin  $\alpha_5\beta_1$  subtype could lead to applications spanning the improvement in cellular uptake of drugs<sup>48</sup> and genetic material,<sup>49</sup> diagnostics,<sup>2</sup> the modulation of stem cell differentiation<sup>50</sup> and cell adhesion applications,<sup>29,51</sup> e.g. artificial ECMs.<sup>52–54</sup>

### 1.1.3 Integrin $\alpha_5\beta_1$ structure & conformation

Integrins were first demonstrated to regulate their ligand-binding activity through conformational changes.<sup>55,56</sup> Further investigations of the crystal structures of a subset of integrins detailed the receptor structure with predictions of ligand binding sites.<sup>57–60</sup> Later, clusters of integrins were visualised on the cell surface acting jointly to function besides transitioning in and out of FAs.<sup>61–63</sup> Whilst these studies further improved our understanding of the integrin structure, function and conformational states, they were mostly derived from studies of integrin  $\alpha_{IIb}\beta_3$  and integrin  $\alpha_v\beta_3$ . Resulting models, namely the widely accepted switchblade model<sup>64</sup> and the deadbolt model<sup>65</sup> led to much debate over the nature and pivotal changes of the conformational states.<sup>66,67</sup> Since, data has shown a deviation from a canonical model applied to the entire integrin family, indicative of distinct conformational changes for respective integrin dimers in accordance with their expression and function.<sup>66,68,69</sup>

Additional complexity in elucidating the underlying mechanisms of receptor conformational change stems from the bidirectional nature of integrin activation. Mounting evidence indicates that integrin conformational imparted affinity plays an important role in “inside-out” signalling whilst both receptor clustering and conformational change are requisite for “outside-in” signalling.<sup>70</sup> With the ensemble of integrin conformations and distributions formed on the surface of the cell being a result of both signalling mechanisms.<sup>66,71</sup> The conformation of integrins is also dependent on divalent metal ions, reportedly involved in ligand binding and in some cases conformational change.<sup>72</sup> Furthermore, the interactions of N-glycosylation patterns on integrins have been detailed and are reportedly crucial in integrin function.<sup>73,74</sup>

Pertinent to this study are reports on distinct conformational changes and mechanisms of integrin  $\alpha_5\beta_1$  activation and ligand binding.<sup>66,74–77</sup> The structure of integrin  $\alpha_5\beta_1$ , detailed in Figure 1.3 can be broken down into three domains, (i) an N-terminal ectodomain (site of ligand binding), (ii) a transmembrane domains and (iii) a short C-terminal cytoplasmic domain.<sup>78</sup> Recently reported, isolated integrin  $\alpha_5\beta_1$  has a resting conformation that is half closed-bent, at  $\sim 90^\circ$  angle between its’ headpiece and legs with its’ binding site being still accessible to native ligand fibronectin (FN) binding.<sup>66,74</sup> The closure at rest of integrin  $\alpha_5\beta_1$  is described as being relatively loose, with a dynamic shift between the equilibrium of conformational states.<sup>68</sup>

The extended-open conformation of the integrin  $\alpha_5\beta_1$  was only observed to be dominant as a result of FN binding in the presence of  $Mn^{2+}$  without prior opening of the extended receptor, indicative of ligand induced conformational change.<sup>66,74</sup> Detailed in Figure 1.3  $Mn^{2+}$  functions in priming the metal ion pockets on the integrin  $\beta_1$  subunit, i.e. synergistic metal ion-binding site (SyMBS) otherwise known as ligand-associated metal-binding site (LIMBS), metal-ion dependent binding site (MIDAS) and adjacent to metal-ion dependent binding site (ADMIDAS).<sup>74,79</sup> Here,  $Mn^{2+}$  is reported to increase the affinity of half closed-bent integrin  $\alpha_5\beta_1$  for FN but does not alone induce a conformational change in the receptor.<sup>66,74</sup> The integrin  $\alpha_5\beta_1$  in complex with its native FN ligand displayed stabilising interactions for integrin opening, i.e. at the RGD loop of FN, the synergy site of FN and adjacent ADMIDAS.<sup>74</sup> The flexibility between the heads and legs, termed molecular breathing<sup>64</sup> is hypothesised to increase the probability of resting integrin  $\alpha_5\beta_1$  engaging the three

FN-integrin  $\alpha_5\beta_1$  interaction sites.<sup>74</sup> Of note, the data obtained indicates that the integrin  $\alpha_5\beta_1$  lacks the intrinsic properties for a conformational change upon  $Mn^{2+}$  induced increase in ligand affinity.<sup>66</sup> In terms of structure, FN ligand binding induces the open-extended conformation of integrin  $\alpha_5\beta_1$  through a swing in the  $\beta$ -hybrid region, with results consistent across several studies.<sup>66,74,75</sup> Meanwhile, the isolated integrin  $\alpha_5\beta_1$ -RGD peptide binding did not induce a conformational change in comparison to the unliganded conformation. This is suggested to represent an initial step in adhesion from inactive integrins.<sup>74,80,81</sup> Nevertheless, isolated integrin  $\alpha_5\beta_1$  headpiece were shown to bind to the RGD ligand in both open and closed conformations with RGD binding inducing a change in headpiece conformation for a quarter of the integrins studied in the absence of  $Mn^{2+}$ .<sup>82</sup> These studies confirm that integrin  $\alpha_5\beta_1$  conformations deviate from the classical model correlating integrin conformation and ligand affinity, and switchblade type conformational change.<sup>66,74,75</sup> The ensemble information on integrin  $\alpha_5\beta_1$  conformational changes is vital to our understanding of receptor clustering, i.e. spacing and binding data interpretation.

Distributions of conformational states of isolated integrins preparations and relative ligand binding affinities should not be assumed to be proportional to the cell surface, merely indicative of how the respective stimuli affects integrin  $\alpha_5\beta_1$  receptor function. The integrin  $\alpha_5\beta_1$  distribution and

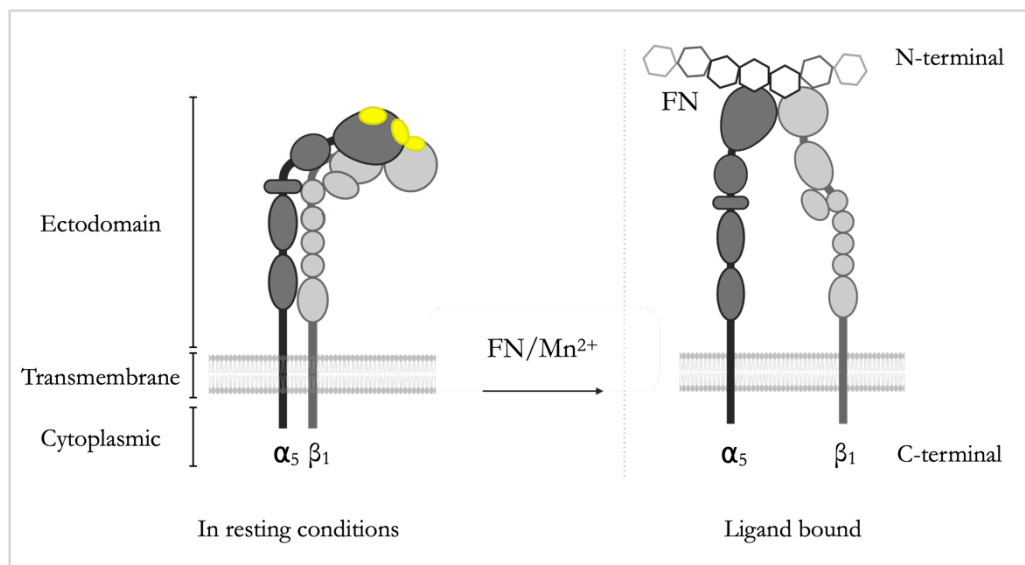


Figure 1.3 Integrin  $\alpha_5\beta_1$  structure and conformation. Adapted from Schumacher et al.<sup>74</sup> Integrin  $\alpha_5\beta_1$  conformations (left : in resting conditions with metal ion pockets highlighted in yellow; right : when FN ligand bound in the presence of  $Mn^{2+}$ ).

binding affinities will likely differ due stabilising mechanisms on the cell, i.e the glycocalyx effect, mechanical forces, intracellular activators and receptor clustering.<sup>66,74,83</sup> Also, isolated integrin  $\alpha_5\beta_1$  studies often employed stabilising antibodies in their methods.<sup>1166,74,75</sup> For instance, around half of the isolated integrin  $\alpha_5\beta_1$  analysed adopted an extended conformation in resting buffer without  $Mn^{2+}$ <sup>74</sup> in contrast to a prior study of integrin  $\alpha_5\beta_1$  conformations on K652 cells being mostly in an inactive state in the absence of an ECM ligand, at resting conditions.<sup>76</sup> Observations in conformations of isolated integrin  $\alpha_5\beta_1$ , i.e. the respective bent and open integrin  $\alpha_5\beta_1$  conformations, are nonetheless confirmed as they have been observed in FRET studies on cells.<sup>74,77</sup>

Conformational states of the isolated integrins<sup>74,82</sup> could shed light on the differences in staining distribution observed on cell surfaces of different activation states and staining methods (activation specific or non-functional)<sup>84</sup> The conformational states adopted would in turn influence the availability of binding sites for integrin targeting and the spatial distribution of receptors within clusters. For instance, on the cell surface, integrin  $\alpha_5\beta_1$  has been reported to segregate into discreet focal adhesion clusters of active and inactive integrins, with active clusters having a higher local order.<sup>62</sup> Integrin  $\alpha_5\beta_1$  was also shown to have nanoscale ligand spatial preferences distinct from other integrin subtypes<sup>85</sup> with different ligand binding behaviours in the range of spacings we investigate (below 60nm).<sup>85,86</sup> Activated integrins by inside-out signalling are also reported to have a localised cell surface distribution, activating only a subset of the integrins overall expressed.<sup>70</sup> Otherwise, super-resolution studies of integrin  $\alpha_v\beta_3$  nascent clusters, show clustering of  $\sim 50$  integrins within 100nm<sup>87</sup> and non-random distribution of clusters at 20-30nm spacings.<sup>88</sup>

The overall conformational changes, i.e. closed-bent at  $\sim 90^\circ$  at rest to open-extended, observed in the integrin  $\alpha_5\beta_1$ , expressed ubiquitously across cell types is proposed to be attributed to its primary function in cell adhesion which would elicit cellular responses slower than that of the immune system.<sup>68</sup> Integrin  $\alpha_v\beta_8$  however, predominantly expressed on immune cells exhibits a closed-extended conformation, presumably for probing for ligands and subsequent quick activation<sup>68,69,89,90</sup> Therefore, we hypothesise that the distribution of integrin subtypes are regulated by cell function, e.g. human umbilical vein endothelial cells (HUVEC) in barrier function,<sup>91</sup> Chinese hamster ovary (CHO) cells in inflammatory response,<sup>92</sup> and Henrietta Lack's epithelial adenocarcinoma cells (HeLa) in cancer resistance.<sup>30</sup>

#### 1.1.4 Integrin $\alpha_5\beta_1$ activation

Integrin clustering and spatial distribution within clusters is preceded by and reliant on activation method.<sup>75,93</sup> Methods for integrin activation, Figure 1.4 reported in literature include the use of divalent cations<sup>94-96</sup>, recombinant integrins,<sup>97,98</sup> activation inducing antibodies<sup>84,99,100</sup> and reducing agents.<sup>101</sup> The native signalling pathways and mechanisms have also been documented over the years.<sup>102-105</sup>

Integrin antibodies can be grouped according to function, i.e. (i) activators or activation-specific that activate or recognise activation specific conformations of the receptor (ii) inhibitors that block and/or bind to the binding pocket or (iii) non-functional.<sup>84</sup> The binding epitopes of the respective integrin  $\alpha_5\beta_1$  activating antibodies, the resulting integrin  $\alpha_5\beta_1$  conformations and the ligand binding abilities are well documented in a study by Su et al.<sup>75</sup> Majority of the available activating antibodies recognise epitopes on the integrin  $\beta_1$  subunit.<sup>84,106</sup> An activating antibody SNAKA51 that primes the integrin  $\alpha_5\beta_1$  for ligand binding was produced by Clark et al., inducing the clustering of integrin  $\alpha_5\beta_1$  and formation of fibrillar (mature) adhesions.<sup>100</sup> Here, the antibody was reported to recognise subsets of activated (extended) integrin conformations.<sup>75,100</sup> Improved affinities of the antibody binding was reported in the presence of  $Mn^{2+}$  and its ligand.<sup>77,100</sup> Reducing agents such as dithiothreitol (DTT) were reported to reduce disulfide bonds in the cysteine-rich lower leg region of the  $\beta_1$  integrins subunit.<sup>78,107-109</sup> As this region is reportedly involved in signal transmission upon

activation, the disulfide bond reduction in a similar manner, leads to global conformation change of the integrin receptor.<sup>84,99,101,110</sup>

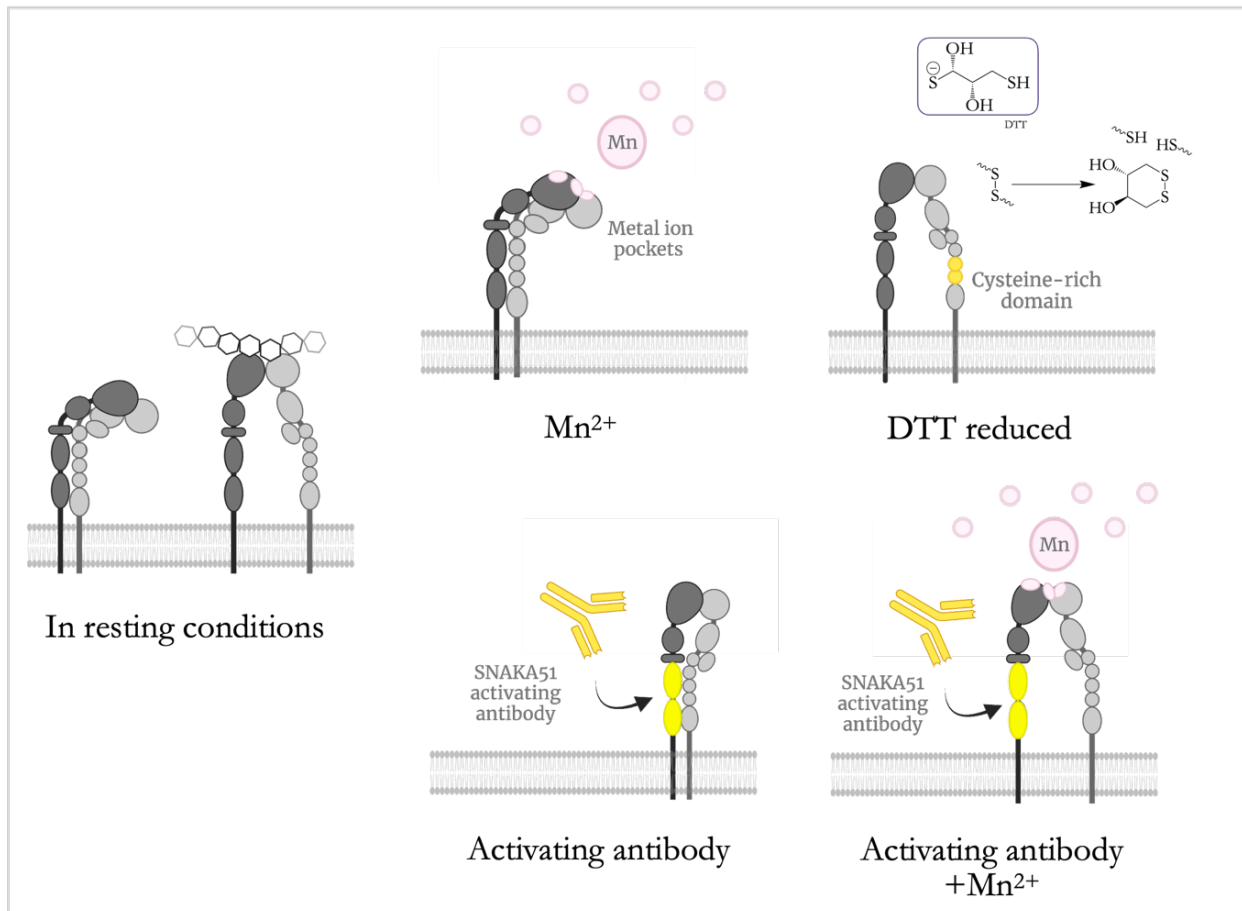


Figure 1.4 Integrin  $\alpha_5\beta_1$  activation methods. Left : Integrin conformations in resting conditions. Right : Activation methods,  $Mn^{2+}$ , DTT reduction, SNAK activating antibody with and without  $Mn^{2+}$ .

### 1.1.5 Integrin clustering & spatial organisation

Ever since the suggestion of imposing spatial organisation of membrane receptors with the aim of understanding cell signalling and the minimal receptor engagement requirements for cell function,<sup>111</sup> studies have been conducted in probing integrin clustering and spatial regulation, Figure 1.5.<sup>112-114</sup>

In a study investigating the effect of ligand clustering on cell migration, Maheshwari et al. used a polymer-linking method to tailor both the average surface density ( $1'000 - 200'000$  peptides  $\mu m^2$ ) the local distribution ( $\sim 50nm$ ) of the linear RGD peptide solely or in clusters averaging 5 or 9 ligands. Here, clustered integrin ligands significantly reduced fibroblast motility, and whilst supporting cell attachment, neither induced full spreading nor haptokinetic nor chemokinetic response. Nonetheless, non-clustered integrins supported cell movement.<sup>115</sup> A separate study by Davey et al. found that  $\beta_1$  integrins are vital for cell spreading as down-regulation in surface



expression of  $\alpha_5\beta_1$  integrins reduces spreading and the formation of stress fibres. Cortical actin assembly however was increased in this case.<sup>116</sup>

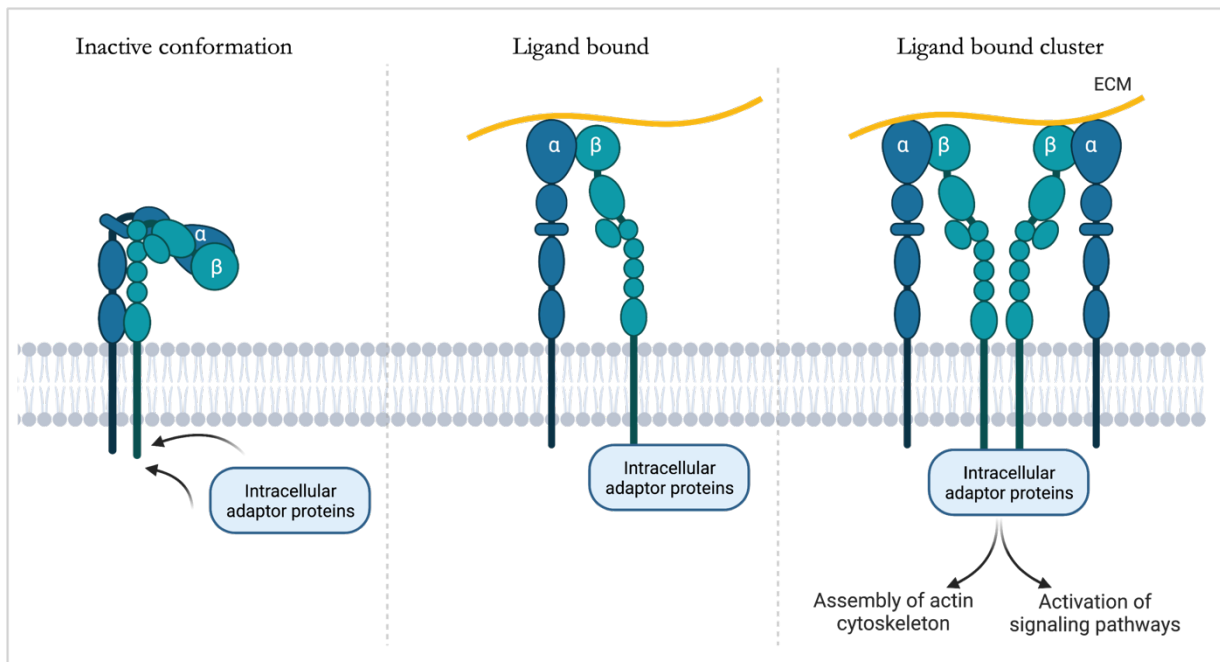


Figure 1.5 Integrin  $\alpha_5\beta_1$  binding and clustering. Left : Integrin  $\alpha_5\beta_1$  inactive conformation. Middle : Initial binding to ECM protein, fibronectin with intracellular adaptor protein recruitment. Right : Integrin  $\alpha_5\beta_1$  clustering upon ECM binding.

An initial study on adhesion units by Massia and Hubbell reported on a minimum of 6 RGD at spacings of 440nm were sufficient in supporting cell spreading.<sup>117</sup> Later on, Schwartzman et al. reported on a minimal adhesion unit, unaffected by global density of 4 ligands spaced within 60nm for cell spreading.<sup>15</sup>

Besides that, the Spatz laboratory has extensively investigated cell response to integrin ligand spatial presentation. They proposed a universal length scale for integrin clustering and activation to be in the range of 58-73nm from several studies.<sup>118-120</sup> One study showed that an increased cyclic RGD nanoscale ligand spacing with high stiffness on soft hydrogels promoted cell adhesion and stem cell osteogenic differentiation.<sup>121</sup> Here, liganded gold nanoparticle (NP) hexagons were transferred to polyacrylamide hydrogels for nanoscale hexagonal patterning and the conservation of cell response to cyclic RGD ligand spacing tested on different cell types.<sup>121</sup> In addition, local ligand presentation was shown to govern integrin clustering and adhesion when global average ligand spacing is larger than 70nm.<sup>122</sup> In a more recent study by Di Russo et al. of keratinocyte collective migratory response to inflammation, integrin  $\alpha_5\beta_1$  spacing was analysed for its ability to modulate focal adhesion formation, dynamics, and cell contact area. Integrin  $\alpha_5\beta_1$  peptidomimetic ligand spacings of 35nm, 50nm, and 70nm were patterned via gold NPs onto polyacrylamide hydrogels. Focal adhesion turnover and migration were found to be highest at 50nm with smallest areas, compared to 35nm and 70nm spacings. Focal adhesion length was however the longest on 70nm spacings.<sup>123</sup>

The Sheetz laboratory meanwhile reported in a similar manner that robust cell cytoskeletal linkages could only be forged with multiple FN adhesion domains spaced within 40-60nm.<sup>124,125</sup> In a separate study by Changede et al. using super-resolution microscopy to interrogate integrin adhesion formation with different RGD liganded fibre geometries, FAs were formed crossed or paired fibres but not of single fibres of widths  $\leq 30$  nm.<sup>126</sup> Fibres thicker than 40nm however induced FA formation. This was found to be a result of clusters of integrin traversing neighbouring fibres composed of co-clustered liganded with unliganded but activated integrins (in extended conformations).<sup>126</sup>

A study by Spiess et al. using two super-resolution techniques additionally reported on the segregation of integrin  $\beta_1$  into separate nanoclusters based on conformation (active versus inactive) with active nanoclusters being more organized.<sup>62</sup> Besides that, integrin receptor clustering was recently reported to be modulated by a non-random organisation of adhesion clusters spaced 20-30nm apart in a recent study from the Jungmann laboratory.<sup>88</sup> Here DNA-PAINT super-resolution was employed on cyclic RGD ligand functionalised DNA tension sensors binding fibroblasts.<sup>88</sup>

In the case of integrin  $\alpha_5\beta_1$  cross-talk with integrin  $\alpha_v\beta_3$ , a study investigating the influence of integrin subtype specific peptidomimetic ligand spacings (36nm, 60nm, 90nm) and density on individual integrin heterodimer signalling and between integrin receptor subtypes with gold and titanium substrates.<sup>13</sup> Relative cell area for both integrin  $\alpha_5\beta_1$  and  $\alpha_v\beta_3$  selective substrates resulted in the largest cell areas for the smallest spacing (36nm). With respect to the integrin  $\alpha_5\beta_1$  selective binding, colocalisation was often observed with clusters of integrin  $\alpha_v\beta_3$  with integrin  $\alpha_5\beta_1$  having higher kinetics and larger cell areas.<sup>13</sup> Integrin  $\alpha_5\beta_1$  selective clusters were also found to be more prominent in fibrillar type adhesions whilst the integrin  $\alpha_v\beta_3$  clusters localised more along the cell periphery.<sup>13</sup> Another study found that the bias between integrins  $\alpha_5\beta_1$  and  $\alpha_v\beta_3$  for ligand spacings ultimately influence the effectiveness of drugs administered.<sup>51</sup> This highlights the selective manner in which integrin subtypes engage ligands triggering distinct cell responses.

Theoretical analyses of integrin clustering and cell response have also been conducted. For instance, an *in silico* study by Comisar et al. correlating the *in vitro* effect of ligand presentation on cell response, i.e. spreading and osteogenic differentiation defined two regimes of adhesion cluster formation.<sup>127</sup> Here, they quantified at multiple length scales, the cell response to sub-adhesion multivalent “islands” (~30-70nm in diameter) of integrin ligands. Notably cell spreading corresponded to the number of bound receptors, focal adhesion kinase phosphorylation with integrin cluster distributed homogeneously and osteogenic differentiation with heterogenous cluster distributions.<sup>127</sup>

Macro versus nanoscale spacing on RGD poly(ethylene glycol) hydrogels was used to investigate human mesenchymal stem cell (hMSCs) integrin  $\alpha_5\beta_1$  cluster formation in a study by Maynard et al.<sup>53</sup> Single cell atomic force spectroscopy revealed that RGD concentration influenced short-term binding. Integrin  $\alpha_5\beta_1$  availability was however dramatically increased on the 10% hydrogel versus the 100% hydrogel, showing that availability and clustering of integrin  $\alpha_5\beta_1$  inversely correlates

with ligand availability.<sup>1</sup> Similar findings were found by Le Saux et al. on lower density RGD surfaces having more activated integrin  $\alpha_5\beta_1$  corresponding to an average spacing of 44nm compared to 100% coverage with HUVECs.<sup>128</sup> Of note, integrin overall expression was conserved across conditions upon investigation. RGD ligands were attached via a hydroxyl termination versus methoxy group termination on two different 1-amino-hexa(ethylene oxide) molecules, of which the ratio was tailored.<sup>128</sup> An earlier study by Oria et al. also probed the effect of ligand distribution on focal adhesion formation on substrates of different rigidities.<sup>129</sup> Here, nanodots were disordered or quasi-hexagonal in distribution with the same mean interparticle distance (50nm or 100nm). Focal adhesion growth was promoted on disordered substrates versus ordered substrates in the regime of spacing tested. This is explained by uneven distribution of forces that allowed some clusters to experience high loads, undergoing mechanotransduction ultimately leading to FA formation.<sup>129</sup>

Altogether, these findings shed light on the influence of the need to understand the spatial organisation that governs integrin receptor engagement across the macro, micro and nanoscale regimes. On the nanoscale, a scaffold capable of interrogating ligand presentation (spacing and valency) at subadhesion dimensions (<100nm) is vital for our understanding of regime boundaries in eliciting integrin clustering and types of adhesion formation observed in the afore-mentioned studies. Of note, this length scale is of relevance as it is the regime of periodic spacing on fibronectin.<sup>130-132</sup> This would coincidentally shed light on the patterning parameters for integrin targeting applications and on mechanisms governing integrin signalling.

## 1.2 Multivalency & Super-selectivity

Multivalent ligand-receptor interactions, that is a scaffold to which multiple numbers (valencies) of interacting moieties was reviewed by Kiessling et al., highlighting the role of multivalent ligands in elucidating the clustering mechanisms of receptors in a spatial and potentially temporal manner.<sup>133</sup> In nature, multivalent interactions that drive cellular responses are relatively weak on an individual level<sup>134</sup> but the collective effect of fine-tuning this array of weak interactions is capable of propagating over distances much greater than that of molecular dimensions.<sup>135,136</sup>

The importance of understanding the biases in the spatial distribution of cues that elicit these responses is noteworthy both for our understanding of cellular function as well as disease progression.<sup>135</sup> The resulting information would be key in the diagnosis and treatment of diseases.<sup>135</sup> Notably, targeted therapies would be made possible through the intelligent design of materials capable of selectively eliciting responses through the incorporation of multivalent interactions.<sup>137</sup>

Given the different expression levels of subtypes of integrin receptors based on cell type and state,<sup>5,6,20,138</sup> engineering a targeting system capable of differentiating between integrin expression levels and types would be necessary in engaging selective cell responses. The principle of super-selectivity, first introduced by Martinez-Veracoechea et al., could be applied for selective integrin

receptor-ligand binding based on expression levels.<sup>139,140</sup> This is due to the “on-off” binding behaviour, ideal for distinguishing between receptor concentrations, i.e. densities for selective binding. Here, the non-linear increase in binding of relatively weak individual ligands in function of receptor coverage, allows for the selective binding of receptors in higher densities, leaving lower density receptors unaffected.<sup>140,141</sup> This is due to the number of potential binding sites (degeneracy) that increase non-linearly when ligands are bound versus unbound in a multivalent system.<sup>141,142</sup> A study of the principle of super-selectivity by Dubacheva et al. was conducted on a model system composed of synthetic polymer, hyaluronan-CD44 receptor-ligand surface system. The authors investigated key parameters, i.e. ligand valency, ligand affinity, number of ligand binding sites and tether length.<sup>143</sup> It was ligand-receptor binding cannot merely be explained by enthalpic effects, i.e. the number of receptors or ligands but also the entropic effects, i.e. reduced conformational freedoms upon ligand binding and combinatorial entropic gains via higher receptor densities.<sup>140</sup> The above information opens avenues for investigating enhanced selectivity in binding with rigid presentations of ligands reflecting receptor spatial distributions, for instance in integrin ligand-receptor targeting. Hence, investigating integrin receptor spatial distributions (dependent on cell type and state) for subsequent ligand spatial patterning would allow for selective cell targeting.

### 1.3 RGD peptides as ligands

RGD peptides are widely studied in integrin targeting with characterised affinities.<sup>148</sup> As integrin expression levels are reported to vary across cells,<sup>5,6,20,138</sup> integrin receptor-RGD ligand are ideal targets for super-selective targeting. In terms of ligands for therapeutic use, peptides have several advantages over protein counterparts. Notably, the affinity and selectivity of the peptide can be easily tailored, peptides have less immunogenicity, lower production costs, are stable against enzymatic degradation hence exhibit longer stability.<sup>144,145</sup> Since its’ discovery, RGD peptides binding integrin receptors have been studied in the context of selective cell response, in particular in terms of adhesion, tailored to the specific cell.<sup>146,147</sup> The low spatial requirements of RGD peptides allow them to be packed with higher densities on the cell surface, compensating for relatively low individual adhesion activity.<sup>145</sup> Besides, tailoring the RGD peptide sequence and conformation allows selective targeting of subsets of integrin receptors.<sup>145,146,148</sup> Given that integrins subtype expression is regulated by cell type and state,<sup>5,8,149</sup> and the relative low affinities of monovalent RGD peptides, RGD liganded nanoscale scaffolds provide an excellent platform in harnessing valency<sup>133</sup> in attempt to selectively engage clusters of integrins present on different cell types and states,<sup>133,150</sup> providing us with means to distinguish between high density versus low density clusters of target receptors.<sup>140,141</sup>

### 1.4 DNA nanotechnology

DNA-based nanotechnology is an ideal scaffold system for the nanoscale manipulation of ligand presentation for cell receptor binding.<sup>151</sup> This is due to a number of factors, namely (i) sequence programmability that imparts modularity in DNA architectures and ligand presentation, (ii)

biocompatibility, (iii) facile tailoring of scaffold flexibility, (iv) monodispersity (v) high spatial precision, down to the Ångström, and (vi) relatively low cost for synthesis. From the pioneering works of Seeman,<sup>152,153</sup> followed by the DNA origami folding method introduced by Rothmund,<sup>154</sup> DNA nanotechnology has been employed in different cellular contexts.<sup>155–158</sup> For DNA Origami, a one-pot method with a few hundred short DNA ‘staple’ strands brings together a longer single-stranded viral DNA sequence, forming a 2D structure on the nanoscale.<sup>154</sup> Since, DNA origami was exploited by Andersen et al. in creating a three-dimensional box structure with nanometer dimensions (42x36x36 nm<sup>3</sup>) for cargo release upon the introduction of an externally supplied ‘key’.<sup>159</sup> Recently, DNA origami has been employed as molecular actuators by Mills et al. to manipulate integrin cell surface receptors through the adjustable single- and double-stranded DNA linkages.<sup>160</sup>

DNA NPs/origami structural fidelity relies however upon high cation concentration.<sup>161,162</sup> Low physiological and cell-culture media have cation concentrations insufficient in preventing denaturation. In addition, nucleases present in these conditions threaten the integrity of DNA NPs/origami.<sup>162,163</sup> Our laboratory has reviewed the stability issues encountered, compared and detailed the methods developed over the years in addressing the maintenance of DNA origami to guide the selection process for biological use.<sup>162</sup> A DNA origami disk, Figure 1.6 and characterised by Eklund et al. for label accessibility upon application of a protective coating for biostability was verified.<sup>164</sup> The DNA origami Disk examined has 36 potential labelling sites on either face for ligand or probe immobilisation. The DNA origami disk was then employed by Comberlato et al. as a tool for ligand binding of Toll-like Receptor 9, where stronger immune activation was achieved upon binding molecule presentation at a distance of 7nm, in agreement with the conformation of the receptor’s active dimer structure.<sup>165</sup>

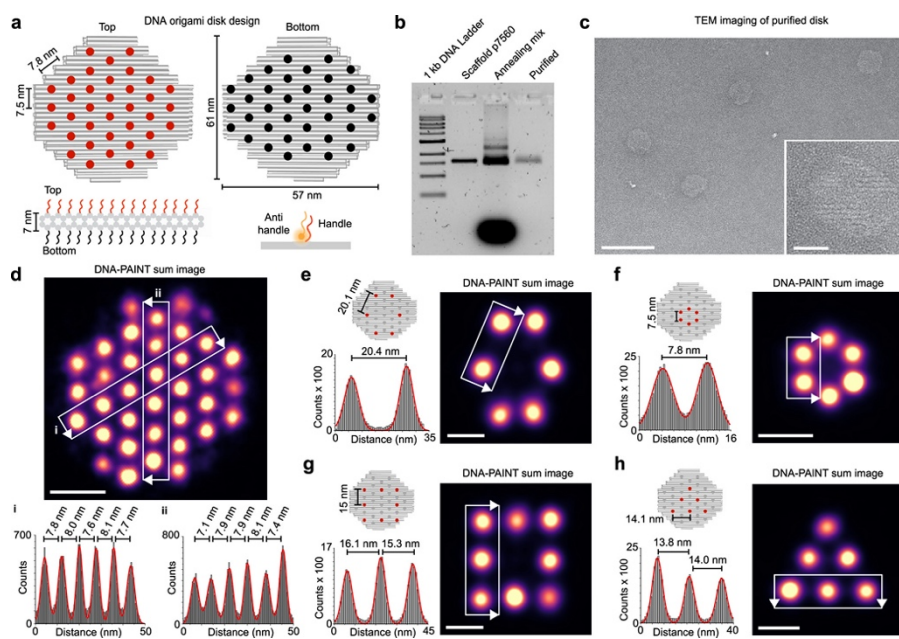


Figure 1.6 DNA origami Disk with two faces for label attachment. Each face allows for 36 ligands with the possibility of heteromultivalent label presentation for different label geometries.

Given the high degree of programmability of DNA origami, we would be able to address current limitations in techniques interrogating the influence of integrin ligand spacing and valency on a sub-adhesion scale, with facile incorporation of heterogenous ligand presentation. The DNA origami platform that affords us with better spatial resolution in targeting and analysis of adhesion formation. This grants us the ability probe the boundaries of spacing and valency in this length scale.

## 1.5 Motivation and Outline

In this thesis, we aim to interrogate the effect of RGD ligand presentation in terms of spacing and flexibility on integrin  $\alpha_5\beta_1$  receptor targeting efficacy. We then investigate the subsequent cell adhesion response to RGD local versus global ligand geometries. In patterning RGD ligands for integrin  $\alpha_5\beta_1$  receptor targeting, receptor distributions and spacings must first be established.

As such, we set out in **Chapter 2** to investigate the differences in integrin  $\alpha_5\beta_1$  receptor expression in 3 different cell types (HUVEC, CHO and HeLa). Here we investigate the resulting antibody staining of activation-specific conformations with different activation methods. Upon selection of an activation method of choice, we model the integrin  $\alpha_5\beta_1$  inter-receptor nearest neighbour distributions in the three cell lines based on cell binding assay and image processing. The distributions of receptors are used in the following Chapter for nanoscale ligand patterning.

In **Chapter 3**, a Bivalent Scaffold presentation of integrin  $\alpha_5\beta_1$  targeting RGD ligands is used to probe integrin  $\alpha_5\beta_1$  inter-receptor spacings on the respective cell types (HUVEC, CHO and HeLa) in resting conditions and when activated. The resulting RGD-liganded Bivalent Scaffold staining and selectivity is detailed. The influence of expression of integrin  $\alpha_5\beta_1$  in extended conformations is discussed. Preliminary assays with RGD ligand presenting higher valency Scaffolds is also presented.

In **Chapter 4**, HUVEC response to immobilised RGD-liganded Multivalent Scaffold with sub-adhesion ligand geometries is presented with a quasi-global ligand presentation control. Trends in adhesion formation, visualised with extra- and intra-cellular markers is detailed. Distinct regimes of HUVEC adhesion response to subadhesion geometries is described and conclusions are drawn on subadhesion geometries promoting HUVEC adhesions.

**Chapter 5** draws the main conclusions from the thesis and discusses future perspectives stemming from this thesis. Briefly, this thesis elaborates on the spatial design of targeting elements on the nanoscale based on receptor presentation and rigidity of ligand presentation for cell binding. The findings could pave the way to achieving higher selectivity and specificity in binding and cell response.

## 1.6 Bibliography

1. Attia, M. F., Anton, N., Wallyn, J., Omran, Z. & Vandamme, T. F. An overview of active and passive targeting strategies to improve the nanocarriers efficiency to tumour sites. *Journal of Pharmacy and Pharmacology* 71, 1185–1198 (2019).
2. Bazak, R., Hourii, M., Achy, S. E., Kamel, S. & Refaat, T. Cancer active targeting by nanoparticles: a comprehensive review of literature. *J Cancer Res Clin Oncol* 141, 769–784 (2015).
3. Vhora, I. et al. Receptor-targeted drug delivery: current perspective and challenges. *Therapeutic Delivery* 5, 1007–1024 (2014).
4. Wu, P.-H., Opadele, A. E., Onodera, Y. & Nam, J.-M. Targeting Integrins in Cancer Nanomedicine: Applications in Cancer Diagnosis and Therapy. *Cancers (Basel)* 11, (2019).
5. Samaržija, I. et al. Integrin Crosstalk Contributes to the Complexity of Signalling and Unpredictable Cancer Cell Fates. *Cancers* 12, 1910 (2020).
6. Vicente-Manzanares, M. & Sánchez-Madrid, F. Targeting the integrin interactome in human disease. *Current Opinion in Cell Biology* 55, 17–23 (2018).
7. Hynes, R. O. Integrins: Bidirectional, Allosteric Signaling Machines. *Cell* 110, 673–687 (2002).
8. Balcioglu, H. E., van Hoorn, H., Donato, D. M., Schmidt, T. & Danen, E. H. J. The integrin expression profile modulates orientation and dynamics of force transmission at cell–matrix adhesions. *Journal of Cell Science* 128, 1316–1326 (2015).
9. Ruoslahti, E. Integrins. *J. Clin. Invest.* 87, 1–5 (1991).
10. Burridge, K. Focal adhesions: a personal perspective on a half century of progress. *The FEBS Journal* 284, 3355–3361 (2017).
11. Giancotti, F. G. A Structural View of Integrin Activation and Signaling. *Developmental Cell* 4, 149–151 (2003).
12. Sun, Z., Guo, S. S. & Fässler, R. Integrin-mediated mechanotransduction. *Journal of Cell Biology* 215, 445–456 (2016).
13. Schaufler, V. et al. Selective binding and lateral clustering of  $\alpha 5 \beta 1$  and  $\alpha v \beta 3$  integrins: Unraveling the spatial requirements for cell spreading and focal adhesion assembly. *Cellul Adhes. Migr.* 10, 505–515 (2016).
14. Tijore, A. et al. Investigating the Spatial Distribution of Integrin  $\beta 1$  in Patterned Human Mesenchymal Stem Cells Using Super-Resolution Imaging. *ACS Appl. Mater. Interfaces* 6, 15686–15696 (2014).
15. Schwartzman, M. et al. Nanolithographic Control of the Spatial Organization of Cellular Adhesion Receptors at the Single-Molecule Level. *Nano Lett.* 11, 1306–1312 (2011).
16. Huggins, D. J., Sherman, W. & Tidor, B. Rational Approaches to Improving Selectivity in Drug Design. *J Med Chem* 55, 1424–1444 (2012).
17. Vlot, A. H. C. et al. Target and Tissue Selectivity Prediction by Integrated Mechanistic Pharmacokinetic-Target Binding and Quantitative Structure Activity Modeling. *AAPS J* 20, 11 (2017).
18. Kavari, S. L. & Shah, K. Engineered stem cells targeting multiple cell surface receptors in tumors. *Stem Cells* 38, 34–44 (2020).
19. Gilcrease, M. Z. Integrin signaling in epithelial cells. *Cancer Letters* 247, 1–25 (2007).
20. Sales, A. et al. Cell Type-Dependent Integrin Distribution in Adhesion and Migration Responses on Protein-Coated Microgrooved Substrates. *ACS Omega* 4, 1791–1800 (2019).
21. Mezu-Ndubuisi, O. J. & Maheshwari, A. The role of integrins in inflammation and angiogenesis. *Pediatr Res* 89, 1619–1626 (2021).
22. Civitarese, R. A., Kapus, A., McCulloch, C. A. & Connelly, K. A. Role of integrins in mediating cardiac fibroblast–cardiomyocyte cross talk: a dynamic relationship in cardiac biology and pathophysiology. *Basic Res Cardiol* 112, 6 (2016).
23. Schussler, O., Chachques, J. C., Alifano, M. & Lecarpentier, Y. Key Roles of RGD-Recognizing Integrins During Cardiac Development, on Cardiac Cells, and After Myocardial Infarction. *J. of Cardiovasc. Trans. Res.* 15, 179–203 (2022).
24. Ghosh, N., Garg, I., Srivastava, S. & Kumar, B. Influence of integrins on thrombus formation: a road leading to the unravelling of DVT. *Mol Cell Biochem* 476, 1489–1504 (2021).
25. Teoh, C. M., Tan, S. S. L. & Tran, T. Integrins as Therapeutic Targets for Respiratory Diseases. undefined (2015).
26. Wu, X. & Reddy, D. S. Integrins as Receptor Targets for Neurological Disorders. *Pharmacol Ther* 134, 68–81 (2012).
27. Schornberg, K. L. et al.  $\alpha 5 \beta 1$ -Integrin controls ebolavirus entry by regulating endosomal cathepsins. *Proceedings of the National Academy of Sciences* 106, 8003–8008 (2009).
28. Simons, P. et al. Integrin activation is an essential component of SARS-CoV-2 infection. *Sci Rep* 11, 20398 (2021).
29. Wolpe, A. G., Ruddiman, C. A., Hall, P. J. & Isakson, B. E. Polarized Proteins in Endothelium and Their Contribution to Function. *JVR* 58, 65–91 (2021).
30. Hou, J., Yan, D., Liu, Y., Huang, P. & Cui, H. The Roles of Integrin  $\alpha 5 \beta 1$  in Human Cancer. *OTT* 13, 13329–13344 (2020).

31. Schaffner, F., Ray, A. M. & Dontenwill, M. Integrin  $\alpha 5\beta 1$ , the Fibronectin Receptor, as a Pertinent Therapeutic Target in Solid Tumors. *Cancers (Basel)* 5, 27–47 (2013).
32. Kuwada, S. K., Kuang, J. & Li, X. Integrin  $\alpha 5/\beta 1$  Expression Mediates HER-2 Down-regulation in Colon Cancer Cells. *J. Biol. Chem.* 280, 19027–19035 (2005).
33. Fujita, M, Suzuki, H. & Fukai, F. Involvement of integrin-activating peptides derived from tenascin-C in colon cancer progression. *World J Gastrointest Oncol.* 13(9): 980–994. (2021).
34. Janouskova, H. et al. Activation of p53 pathway by Nutlin-3a inhibits the expression of the therapeutic target  $\alpha 5$  integrin in colon cancer cells. *Cancer Letters* 336, 307–318 (2013).
35. Nam, J.-M., Onodera, Y., Bissell, M. J. & Park, C. C. Breast cancer cells in three-dimensional culture display an enhanced radioresponse after coordinate targeting of integrin alpha5beta1 and fibronectin. *Cancer Res* 70, 5238–5248 (2010).
36. Li, X. et al. The exosomal integrin  $\alpha 5\beta 1$ /AEP complex derived from epithelial ovarian cancer cells promotes peritoneal metastasis through regulating mesothelial cell proliferation and migration. *Cell Oncol.* 43, 263–277 (2020).
37. Mette, S. A., Pilewski, J., Buck, C. A. & Albelda, S. M. Distribution of Integrin Cell Adhesion Receptors on Normal Bronchial Epithelial Cells and Lung Cancer Cells In Vitro and In Vivo. *Am J Respir Cell Mol Biol* 8, 562–572 (1993).
38. Roman, J., Ritzenthaler, J. D., Roser-Page, S., Sun, X. & Han, S.  $\alpha 5\beta 1$ -Integrin Expression Is Essential for Tumor Progression in Experimental Lung Cancer. *Am J Respir Cell Mol Biol* 43, 684–691 (2010).
39. Wang, H.-Y., Chen, Z., Wang, Z.-H., Wang, H. & Huang, L.-M. Prognostic Significance of  $\alpha 5\beta 1$ -integrin Expression in Cervical Cancer. *Asian Pacific Journal of Cancer Prevention* 14, 3891–3895 (2013).
40. Zhu, H. et al. Predictive role of galectin-1 and integrin  $\alpha 5\beta 1$  in cisplatin-based neoadjuvant chemotherapy of bulky squamous cervical cancer. *Bioscience Reports* 37, BSR20170958 (2017).
41. Rüegg, C., Dormond, O. & Mariotti, A. Endothelial cell integrins and COX-2: mediators and therapeutic targets of tumor angiogenesis. *Biochimica et Biophysica Acta (BBA) - Reviews on Cancer* 1654, 51–67 (2004).
42. Matlin, K. S., Haus, B. & Zuk, A. Integrins in epithelial cell polarity: using antibodies to analyze adhesive function and morphogenesis. *Methods* 30, 235–246 (2003).
43. Watt, F. M. Role of integrins in regulating epidermal adhesion, growth and differentiation. *EMBO J* 21, 3919–3926 (2002).
44. Sheppard, D. Functions of Pulmonary Epithelial Integrins: From Development to Disease. *Physiological Reviews* 83, 673–686 (2003).
45. Taddei, I. et al. Integrins in Mammary Gland Development and Differentiation of Mammary Epithelium. *J Mammary Gland Biol Neoplasia* 8, 383–394 (2003).
46. Franco-Barraza, J. et al. Matrix-regulated integrin  $\alpha v\beta 5$  maintains  $\alpha 5\beta 1$ -dependent desmoplastic traits prognostic of neoplastic recurrence. *eLife* 6, e20600 (2017).
47. Avraamides, C. J., Garmy-Susini, B. & Varner, J. A. Integrins in angiogenesis and lymphangiogenesis. *Nat Rev Cancer* 8, 604–617 (2008).
48. Zhang, R., Qin, X., Kong, F., Chen, P. & Pan, G. Improving cellular uptake of therapeutic entities through interaction with components of cell membrane. *Drug Deliv* 26, 328–342 (2019).
49. Liang, H. et al. Functional DNA-Containing Nanomaterials: Cellular Applications in Biosensing, Imaging, and Targeted Therapy. *Acc. Chem. Res.* 47, 1891–1901 (2014).
50. Sachlos, E. et al. Identification of Drugs Including a Dopamine Receptor Antagonist that Selectively Target Cancer Stem Cells. *Cell* 149, 1284–1297 (2012).
51. Young, J. L. et al. Integrin Subtypes and Nanoscale Ligand Presentation Influence Drug Sensitivity in Cancer Cells. *Nano Lett.* 20, 1183–1191 (2020).
52. Deng, J., Zhao, C., Spatz, J. P. & Wei, Q. Nanopatterned Adhesive, Stretchable Hydrogel to Control Ligand Spacing and Regulate Cell Spreading and Migration. *ACS Nano* 11, 8282–8291 (2017).
53. Maynard, S. A. et al. Nanoscale Molecular Quantification of Stem Cell–Hydrogel Interactions. *ACS Nano* 14, 17321–17332 (2020).
54. Zhou, N. et al. Effect of RGD content in poly(ethylene glycol)-crosslinked poly(methyl vinyl ether-alt-maleic acid) hydrogels on the expansion of ovarian cancer stem-like cells. *Materials Science and Engineering: C* 118, 111477 (2021).
55. Frelinger, A. L. et al. Selective inhibition of integrin function by antibodies specific for ligand-occupied receptor conformers. *J Biol Chem* 265, 6346–6352 (1990).
56. Mould, A. P. Getting integrins into shape: recent insights into how integrin activity is regulated by conformational changes. *Journal of Cell Science* 109, 2613–2618 (1996).
57. Xiong, J.-P. et al. Crystal Structure of the Extracellular Segment of Integrin  $\alpha V\beta 3$ . *Science* 294, 339–345 (2001).
58. Xiong, J.-P. et al. Crystal Structure of the Extracellular Segment of Integrin  $\alpha V\beta 3$  in Complex with an Arg-Gly-Asp Ligand. *Science* 296, 151–155 (2002).
59. Xiong, J.-P. et al. Crystal structure of the complete integrin  $\alpha V\beta 3$  ectodomain plus an  $\alpha/\beta$  transmembrane fragment. *J Cell Biol* 186, 589–600 (2009).



60. Xiao, T., Takagi, J., Collier, B. S., Wang, J.-H. & Springer, T. A. Structural basis for allostery in integrins and binding to fibrinogen-mimetic therapeutics. *Nature* 432, 59–67 (2004).
61. Iwamoto, D. V. & Calderwood, D. A. Regulation of integrin-mediated adhesions. *Current Opinion in Cell Biology* 36, 41–47 (2015).
62. Spiess, M. et al. Active and inactive  $\beta 1$  integrins segregate into distinct nanoclusters in focal adhesions. *J Cell Biol* 217, 1929–1940 (2018).
63. Shibata, A. C. E. et al. Archipelago architecture of the focal adhesion: Membrane molecules freely enter and exit from the focal adhesion zone. *Cytoskeleton* 69, 380–392 (2012).
64. Shimaoka, M., Takagi, J. & Springer, T. A. Conformational Regulation of Integrin Structure and Function. *Annual Review of Biophysics and Biomolecular Structure* 31, 485–516 (2002).
65. Arnaout, M. A., Goodman, S. L. & Xiong, J.-P. Structure and mechanics of integrin-based cell adhesion. *Curr Opin Cell Biol* 19, 495–507 (2007).
66. Miyazaki, N., Iwasaki, K. & Takagi, J. A systematic survey of conformational states in  $\beta 1$  and  $\beta 4$  integrins using negative-stain electron microscopy. *Journal of Cell Science* 131, jcs216754 (2018).
67. Askari, J. A., Buckley, P. A., Mould, A. P. & Humphries, M. J. Linking integrin conformation to function. *J Cell Sci* 122, 165–170 (2009).
68. Schumacher, S. Structural and biochemical characterization of the interaction between focal adhesion receptor integrin  $\alpha 5 \beta 1$  and fibronectin. (Ludwig-Maximilians-Universität München, 2020).
69. Cormier, A. et al. Cryo-EM structure of the  $\alpha v \beta 8$  integrin reveals a mechanism for stabilizing integrin extension. *Nat Struct Mol Biol* 25, 698–704 (2018).
70. Luo, B.-H., Carman, C. V. & Springer, T. A. Structural Basis of Integrin Regulation and Signaling. *Annual Review of Immunology* 25, 619–647 (2007).
71. Qin, J., Vinogradova, O. & Plow, E. F. Integrin Bidirectional Signaling: A Molecular View. *PLOS Biology* 2, e169 (2004).
72. Lee, J. O., Rieu, P., Arnaout, M. A. & Liddington, R. Crystal structure of the A domain from the alpha subunit of integrin CR3 (CD11b/CD18). *Cell* 80, 631–638 (1995).
73. Isaji, T., Sato, Y., Fukuda, T. & Gu, J. N-Glycosylation of the I-like Domain of  $\beta 1$  Integrin Is Essential for  $\beta 1$  Integrin Expression and Biological Function. *J Biol Chem* 284, 12207–12216 (2009).
74. Schumacher, S. et al. Structural insights into integrin  $\alpha 5 \beta 1$  opening by fibronectin ligand. *Science Advances* 7, eabe9716 (2021).
75. Su, Y. et al. Relating conformation to function in integrin  $\alpha 5 \beta 1$ . *Proc. Natl. Acad. Sci. U.S.A.* 113, E3872–3881 (2016).
76. Conformational equilibria and intrinsic affinities define integrin activation. *The EMBO Journal* 36, 629–645 (2017).
77. Askari, J. A. et al. Focal adhesions are sites of integrin extension. *Journal of Cell Biology* 188, 891–903 (2010).
78. Tamkun, J. W. et al. Structure of integrin, a glycoprotein involved in the transmembrane linkage between fibronectin and actin. *Cell* 46, 271–282 (1986).
79. Zhu, J., Zhu, J. & Springer, T. A. Complete integrin headpiece opening in eight steps. *Journal of Cell Biology* 201, 1053–1068 (2013).
80. Nagae, M. et al. Crystal structure of  $\alpha 5 \beta 1$  integrin ectodomain: atomic details of the fibronectin receptor. *J. Cell Biol.* 197, 131–140 (2012).
81. Xia, W. & Springer, T. A. Metal ion and ligand binding of integrin  $\alpha 5 \beta 1$ . *Proc. Natl. Acad. Sci. U.S.A.* 111, 17863–17868 (2014).
82. Structure of integrin  $\alpha 5 \beta 1$  in complex with fibronectin. *The EMBO Journal* 22, 4607–4615 (2003).
83. Paszek, M. J. et al. The cancer glycolyx mechanically primes integrin-mediated growth and survival. *Nature* 511, 319–325 (2014).
84. Byron, A. et al. Anti-integrin monoclonal antibodies. *J Cell Sci* 122, 4009–4011 (2009).
85. Young, J. L. et al. Integrin Subtypes and Nanoscale Ligand Presentation Influence Drug Sensitivity in Cancer Cells. *Nano Lett.* 20, 1183–1191 (2020).
86. Bae, G. et al. Receptor-Level Proximity and Fastening of Ligands Modulates Stem Cell Differentiation. *Advanced Functional Materials* 2200828. (2022).
87. Changede, R., Xu, X., Margadant, F. & Sheetz, M. P. Nascent Integrin Adhesions Form on All Matrix Rigidities after Integrin Activation. *Dev Cell* 35, 614–621 (2015).
88. Schlichthaerle, T., Lindner, C. & Jungmann, R. Super-resolved visualization of single DNA-based tension sensors in cell adhesion. *Nat Commun* 12, 2510 (2021).
89. Minagawa, S. et al. Selective targeting of TGF- $\beta$  activation to treat fibroinflammatory airway disease. *Sci Transl Med* 6, 241ra79 (2014).
90. Wang, J. et al. Atypical interactions of integrin  $\alpha V \beta 8$  with pro-TGF- $\beta 1$ . *Proceedings of the National Academy of Sciences* 114, E4168–E4174 (2017).
91. Poulos, F. E. & Petrich, B. G. Integrin-dependent regulation of the endothelial barrier. *Tissue Barriers* 7, 1685844 (2019).

92. Pilewski, J. M., Latoche, J. D., Arcasoy, S. M. & Albelda, S. M. Expression of integrin cell adhesion receptors during human airway epithelial repair in vivo. *American Journal of Physiology-Lung Cellular and Molecular Physiology* 273, L256–L263 (1997).
93. Ali, O. et al. Cooperativity between Integrin Activation and Mechanical Stress Leads to Integrin Clustering. *Biophysical Journal* 100, 2595–2604 (2011).
94. Dormond, O., Ponsonnet, L., Hasmim, M., Foletti, A. & Rügge, C. Manganese-induced integrin affinity maturation promotes recruitment of  $\alpha V\beta 3$  integrin to focal adhesions in endothelial cells: evidence for a role of phosphatidylinositol 3-kinase and Src. *Thromb Haemost* 92, 151–161 (2004).
95. Miyake, K., Yamashita, Y. & Kimoto, M. A calcium- or manganese-dependent epitope on the integrin  $\beta 1$  chain recognized by a unique mAb. *International Immunology* 6, 1221–1226 (1994).
96. Yanai, T., Shimo-Oka, T. & Ii, I. Manganese Ion Elicits a Binding Activity of Placenta Vitronectin Receptor to Fibronectin Cell-Binding Domain. *Cell Structure and Function* 16, 149–156 (1991).
97. Banères, J.-L., Roquet, F., Martin, A. & Parello, J. A Minimized Human Integrin  $\alpha 5\beta 1$  That Retains Ligand Recognition \*. *Journal of Biological Chemistry* 275, 5888–5903 (2000).
98. O'Toole, T. et al. Integrin cytoplasmic domains mediate inside-out signal transduction. *Journal of Cell Biology* 124, 1047–1059 (1994).
99. Bazzoni, G., Shih, D.-T., Buck, C. A. & Hemler, M. E. Monoclonal Antibody 9EG7 Defines a Novel  $\beta 1$  Integrin Epitope Induced by Soluble Ligand and Manganese, but Inhibited by Calcium (\*). *Journal of Biological Chemistry* 270, 25570–25577 (1995).
100. Clark, K. et al. A specific  $\alpha 5\beta 1$ -integrin conformation promotes directional integrin translocation and fibronectin matrix formation. *Journal of Cell Science* 118, 291–300 (2005).
101. Yan, B. & Smith, J. W. Mechanism of Integrin Activation by Disulfide Bond Reduction. *Biochemistry* 40, 8861–8867 (2001).
102. Calderwood, D. A. Integrin activation. *Journal of Cell Science* 117, 657–666 (2004).
103. Woodside, D. G., Liu, S. & Ginsberg, M. H. Integrin Activation. *Thromb Haemost* 86, 316–323 (2001).
104. Kim, C., Ye, F. & Ginsberg, M. H. Regulation of Integrin Activation. *Annual Review of Cell and Developmental Biology* 27, 321–345 (2011).
105. Ginsberg, M. H. Integrin activation. *BMB Reports* 47, 655–659 (2014).
106. Humphries, M. J., Symonds, E. J. & Mould, A. P. Mapping functional residues onto integrin crystal structures. *Current Opinion in Structural Biology* 13, 236–243 (2003).
107. Humphries, M. J. Integrin structure. *Biochem Soc Trans* 28, 311–339 (2000).
108. Kishimoto, T. K., Hollander, N., Roberts, T. M., Anderson, D. C. & Springer, T. A. Heterogeneous mutations in the  $\beta$  subunit common to the LFA-1, Mac-1, and p150,95 glycoproteins cause leukocyte adhesion deficiency. *Cell* 50, 193–202 (1987).
109. Takagi, J., Beglova, N., Yalamanchili, P., Blacklow, S. C. & Springer, T. A. Definition of EGF-like, closely interacting modules that bear activation epitopes in integrin beta subunits. *Proc Natl Acad Sci U S A* 98, 11175–11180 (2001).
110. Takagi, J., Isobe, T., Takada, Y. & Saito, Y. Structural interlock between ligand-binding site and stalk-like region of beta1 integrin revealed by a monoclonal antibody recognizing conformation-dependent epitope. *J Biochem* 121, 914–921 (1997).
111. Buckley, C. D., Rainger, G. E., Bradfield, P. F., Nash, G. B. & Simmons, D. L. Cell adhesion: More than just glue (Review). *Molecular Membrane Biology* 15, 167–176 (1998).
112. Changede, R. & Sheetz, M. Integrin and cadherin clusters: A robust way to organize adhesions for cell mechanics. *BioEssays* 39, e201600123 (2017).
113. Dhavalikar, P. et al. Review of Integrin-Targeting Biomaterials in Tissue Engineering. *Advanced Healthcare Materials* 9, 2000795 (2020).
114. Geiger, B., Spatz, J. P. & Bershadsky, A. D. Environmental sensing through focal adhesions. *Nat. Rev. Mol. Cell Biol.* 10, 21–33 (2009).
115. Maheshwari, G., Brown, G., Lauffenburger, D. A., Wells, A. & Griffith, L. G. Cell adhesion and motility depend on nanoscale RGD clustering. *Journal of Cell Science* 113, 1677–1686 (2000).
116. Davey, G., Buzzai, M. & Assoian, R. K. Reduced expression of (alpha)5(beta)1 integrin prevents spreading-dependent cell proliferation. *Journal of Cell Science* 112, 4663–4672 (1999).
117. Massia, S. P. & Hubbell, J. A. An RGD Spacing of 440 nm Is Sufficient for Integrin  $\alpha v\beta 3$ -Mediated Fibroblast Spreading and 140 nm for Focal Contact and Stress Fiber Formation. *The Journal of Cell Biology* 114, 1089–1100 (1991).
118. Arnold, M. et al. Activation of Integrin Function by Nanopatterned Adhesive Interfaces. *ChemPhysChem* 5, 383–388 (2004).
119. Cavalcanti-Adam, E. A. et al. Cell Spreading and Focal Adhesion Dynamics Are Regulated by Spacing of Integrin Ligands. *Biophysical Journal* 92, 2964–2974 (2007).
120. Cavalcanti-Adam, E. A. et al. Lateral spacing of integrin ligands influences cell spreading and focal adhesion assembly. *European Journal of Cell Biology* 85, 219–224 (2006).

121. Zhang, M. et al. Controllable ligand spacing stimulates cellular mechanotransduction and promotes stem cell osteogenic differentiation on soft hydrogels. *Biomaterials* 268, 120543 (2021).
122. Huang, J. et al. Impact of order and disorder in RGD nanopatterns on cell adhesion. *Nano Lett* 9, 1111–1116 (2009).
123. Di Russo, J. et al. Integrin  $\alpha 5 \beta 1$  nano-presentation regulates collective keratinocyte migration independent of substrate rigidity. *eLife* 10, e69861 (2021).
124. Roca-Cusachs, P., Gauthier, N. C., del Rio, A. & Sheetz, M. P. Clustering of  $\alpha 5 \beta 1$  integrins determines adhesion strength whereas  $\alpha v \beta 3$  and talin enable mechanotransduction. *Proc Natl Acad Sci U S A* 106, 16245–16250 (2009).
125. Jiang, G., Giannone, G., Critchley, D. R., Fukumoto, E. & Sheetz, M. P. Two-piconewton slip bond between fibronectin and the cytoskeleton depends on talin. *Nature* 424, 334–337 (2003).
126. Changede, R., Cai, H., Wind, S. J. & Sheetz, M. P. Integrin nanoclusters can bridge thin matrix fibres to form cell–matrix adhesions. *Nature Materials* 18, 1366–1375 (2019).
127. Comisar, W. A., Mooney, D. J. & Linderman, J. J. Integrin Organization: Linking Adhesion Ligand Nanopatterns with Altered Cell Responses. *J Theor Biol* 274, 120–130 (2011).
128. Le Saux, G. et al. Spacing of Integrin Ligands Influences Signal Transduction in Endothelial Cells. *Biophys J* 101, 764–773 (2011).
129. Oria, R. et al. Force loading explains spatial sensing of ligands by cells. *Nature* 552, 219–+ (2017).
130. Vogel, V. & Sheetz, M. Local force and geometry sensing regulate cell functions. *Nat Rev Mol Cell Biol* 7, 265–275 (2006).
131. Carreiras, F. et al. Involvement of  $\alpha v \beta 3$  integrin and disruption of endothelial fibronectin network during the adhesion of the human ovarian adenocarcinoma cell line IGROV1 on the human umbilical vein cell extracellular matrix. *International Journal of Cancer* 99, 800–808 (2002).
132. Vogel, V. MECHANOTRANSDUCTION INVOLVING MULTIMODULAR PROTEINS: Converting Force into Biochemical Signals. *Annual Review of Biophysics and Biomolecular Structure* 35, 459–488 (2006).
133. Kiessling, L. L., Gestwicki, J. E. & Strong, L. E. Synthetic Multivalent Ligands as Probes of Signal Transduction. *Angew. Chem. Int. Ed.* 45, 2348–2368 (2006).
134. Eisenstein, M. Strength in numbers. *Nat Methods* 10, 823–823 (2013).
135. Bakshi, A. K., Haider, T., Tiwari, R. & Soni, V. Critical parameters for design and development of multivalent nanoconstructs: recent trends. *Drug Deliv. and Transl. Res.* (2022).
136. Kane, R. S. Thermodynamics of Multivalent Interactions: Influence of the Linker. *Langmuir* 26, 8636–8640 (2010).
137. Wang, J., Tian, S., Petros, R. A., Napier, M. E. & DeSimone, J. M. The Complex Role of Multivalency in Nanoparticles Targeting the Transferrin Receptor for Cancer Therapies. *J. Am. Chem. Soc.* 132, 11306–11313 (2010).
138. Taherian, A., Li, X., Liu, Y. & Haas, T. A. Differences in integrin expression and signaling within human breast cancer cells. *BMC Cancer* 11, 293 (2011).
139. Martinez-Veracochea, F. J. & Frenkel, D. Designing super selectivity in multivalent nano-particle binding. *PNAS* 108, 10963–10968 (2011).
140. Dubacheva, G. V., Curk, T., Auzély-Velty, R., Frenkel, D. & Richter, R. P. Designing multivalent probes for tunable superselective targeting. *PNAS* 112, 5579–5584 (2015).
141. Martinez-Veracochea, F. J. & Frenkel, D. Designing super selectivity in multivalent nano-particle binding. *Proceedings of the National Academy of Sciences* 108, 10963–10968 (2011).
142. Curk, T., Dobnikar, J. & Frenkel, D. Design Principles for Super Selectivity using Multivalent Interactions. in *Multivalency* 75–101 (John Wiley & Sons, Ltd, 2018).
143. Dubacheva, G. V. et al. Superselective Targeting Using Multivalent Polymers. *J. Am. Chem. Soc.* 136, 1722–1725 (2014).
144. Wang, L. et al. Therapeutic peptides: current applications and future directions. *Sig Transduct Target Ther* 7, 1–27 (2022).
145. Hersel, U., Dahmen, C. & Kessler, H. RGD Modified Polymers: Biomaterials for Stimulated Cell Adhesion and Beyond. *Biomaterials* 24, 4385–415 (2003).
146. Pierschbacher, M. D. & Ruoslahti, E. Influence of stereochemistry of the sequence Arg-Gly-Asp-Xaa on binding specificity in cell adhesion. *J Biol Chem* 262, 17294–17298 (1987).
147. Borgne-Sanchez, A. et al. Targeted Vpr-derived peptides reach mitochondria to induce apoptosis of alphaVbeta3-expressing endothelial cells. *Cell Death Differ* 14, 422–435 (2007).
148. Kapp, T. G. et al. A Comprehensive Evaluation of the Activity and Selectivity Profile of Ligands for RGD-binding Integrins. *Sci Rep* 7, 39805 (2017).
149. Lowell, C. A. & Mayadas, T. N. Overview-studying integrins in vivo. *Methods Mol Biol* 757, 369–397 (2012).
150. Montet, X., Funovics, M., Montet-Abou, K., Weissleder, R. & Josephson, L. Multivalent Effects of RGD Peptides Obtained by Nanoparticle Display. *J. Med. Chem.* 49, 6087–6093 (2006).

151. Chen, Y.-J., Groves, B., Muscat, R. A. & Seelig, G. DNA nanotechnology from the test tube to the cell. *Nature Nanotech* 10, 748–760 (2015).
152. Seeman, N. C. Molecular Craftwork with DNA. in *Culture of Chemistry: The Best Articles on the Human Side of 20th-Century Chemistry from the Archives of the Chemical Intelligencer* (eds. Hargittai, B. & Hargittai, I.) 141–152 (Springer US, 2015).
153. Seeman, N. C. DNA in a material world. *Nature* 421, 427–431 (2003).
154. Rothemund, P. W. K. Folding DNA to create nanoscale shapes and patterns. *Nature* 440, 297–302 (2006).
155. Wang, W. et al. Bioapplications of DNA nanotechnology at the solid–liquid interface. *Chemical Society Reviews* 48, 4892–4920 (2019).
156. Jahanban-Esfahlan, R. et al. Static DNA Nanostructures For Cancer Theranostics: Recent Progress In Design And Applications. *Nanotechnol Sci Appl* 12, 25–46 (2019).
157. Wang, H., Luo, D., Wang, H., Wang, F. & Liu, X. Construction of smart stimuli-responsive DNA nanostructures for biomedical applications. *Chemistry – A European Journal*, (2020).
158. Zhang, K., Gao, H., Deng, R. & Li, J. Emerging Applications of Nanotechnology for Controlling Cell-Surface Receptor Clustering. *Angewandte Chemie International Edition* 58, 4790–4799 (2019).
159. Andersen, E. S. et al. Self-assembly of a nanoscale DNA box with a controllable lid. *Nature* 459, 73–76 (2009).
160. Mills, A. et al. A modular spring-loaded actuator for mechanical activation of membrane proteins. *Nat. Commun.* 13, 3182 (2022).
161. Kielar, C. et al. On the Stability of DNA Origami Nanostructures in Low-Magnesium Buffers. *Angewandte Chemie International Edition* 57, 9470–9474 (2018).
162. Bila, H., Kurisinkal, E. E. & Bastings, M. M. C. Engineering a stable future for DNA-origami as a biomaterial. *Biomater. Sci.* 7, 532–541 (2019).
163. Chandrasekaran, A. R. Nuclease resistance of DNA nanostructures. *Nat Rev Chem* 5, 225–239 (2021).
164. Eklund, A. S., Comberlato, A., Parish, I. A., Jungmann, R. & Bastings, M. M. C. Quantification of Strand Accessibility in Biostable DNA Origami with Single-Staple Resolution. *ACS Nano* (2021).
165. Comberlato, A., Koga, M. M., Nüssing, S., Parish, I. A. & Bastings, M. M. C. Spatially Controlled Activation of Toll-like Receptor 9 with DNA-Based Nanomaterials. *Nano Lett.* 22, 2506–2513 (2022).

## Chapter 2 Characterisation of integrin $\alpha_5\beta_1$ expression & distribution

Targeting cells specifically based on receptor expression levels remains an area of active research to date. The selective binding of receptors cannot merely be achieved with increasing individual receptor ligand binding in most cases as this approach does not account for differing distributions of receptor density across healthy and diseased cells.<sup>1,2</sup> Hence, targeting receptors above a threshold concentration, leaving sparser counterparts unaffected would be desirable in devising selective targeting systems.<sup>2</sup> Integrin cell surface receptors are prime candidates as target receptors as they are readily available on the cell surface and have been reported to be overexpressed in certain diseases.<sup>3,4</sup> Insights into the spatial organization of these receptors would therefore be useful to design selective targeting agents. Here, we first investigate the effect of activation method on integrin  $\alpha_5\beta_1$  clustering by immunofluorescence. We then take three cell types of decreasing levels of integrin  $\alpha_5\beta_1$  receptor expression, HUVEC, CHO and HeLa. We model the integrin  $\alpha_5\beta_1$  inter-receptor nearest neighbour distances with input from cell binding assay data on receptor expression levels and image processing of confocal microscopy images for subsequent targeting studies. We observe the possibility of a shift in integrin receptor spatial distribution in the sub 60nm region.

Citation: Kurisinkal, E.E.; Caroprese, V.; Koga, M.M.; Morzy, D.; Bastings, M.M.C. Selective Integrin  $\alpha_5\beta_1$  Targeting through Spatially Constrained Multivalent DNA-Based Nanoparticles. *Molecules* **2022**, *27*, 4968. <https://doi.org/10.3390/molecules27154968>

Author Contributions: Conceptualization, M.M.C.B., V.C. and E.E.K.; methodology, E.E.K.; software, V.C., and E.E.K.; validation, M.M.K. and E.E.K.; formal analysis, E.E.K.; investigation, E.E.K., M.M.K. and D.M.; resources, M.M.C.B.; data curation, E.E.K. and V.C.; writing—original draft preparation, E.E.K.; writing—review and editing, M.M.C.B.; visualization, E.E.K.; supervision, M.M.C.B.; project administration, M.M.C.B.; funding acquisition, M.M.C.B. All authors have read and agreed to the published version of the manuscript.

### 2.1 Introduction

Integrin expression levels vary dependent on cell type and are implicated in many diseases.<sup>5-7</sup> As principle integrin heterodimers are ubiquitously represented on cells, selective targeting of integrins based on expression levels is an interesting approach to increase selectivity for integrin-targeted applications.<sup>8-10</sup> The goal of this chapter is to investigate the potential shift in spatial clustering regimes exhibited by integrin  $\alpha_5\beta_1$  based on different cell types based on overall expression levels, Figure 2.1. This information can be used to guide the design of applications for integrin  $\alpha_5\beta_1$

targeting based on ligand spacing. As such, the results obtained from this chapter will be used to guide subsequent studies founded on experimenting with cells of different integrin  $\alpha_5\beta_1$  distributions.

We first analyse the results of activation methods (activation specific antibody, reducing agent, divalent cations),<sup>11-14</sup> its' impact on integrin  $\alpha_5\beta_1$  receptor distribution and cell morphology by means of immunofluorescence of an activation specific integrin antibody, SNAKA51 coupled with a fluorescently tagged secondary antibody system. This analysis is performed across three cell types (HUVEC, CHO, HeLa). Activation methods investigated include (i) a reducing agent, dithiothreitol (DTT)<sup>15</sup>, for the reduction of disulfide bonds in the cysteine rich domain of the integrin  $\beta_1$  subunit<sup>16,17</sup> (ii) SNAKA51 integrin  $\alpha_5\beta_1$  activation antibody<sup>11</sup> that converts the integrin  $\alpha_5\beta_1$  to a ligand-competent form<sup>11</sup> and (iii) Manganese in increasing the affinity of the integrin  $\alpha_5\beta_1$  ligand<sup>12,18,19</sup> in combination with (ii). Thereafter, we investigate integrin  $\alpha_5\beta_1$  expression levels on the three cell types of choice via cell binding assay. Data obtained is combined from the cell binding assay and image processing of fluorescence microscopy images to establish a mathematical model of integrin inter-receptor  $\alpha_5\beta_1$  nearest-neighbour distribution in terms of spacing in the respective cell lines, Figure 2.1.

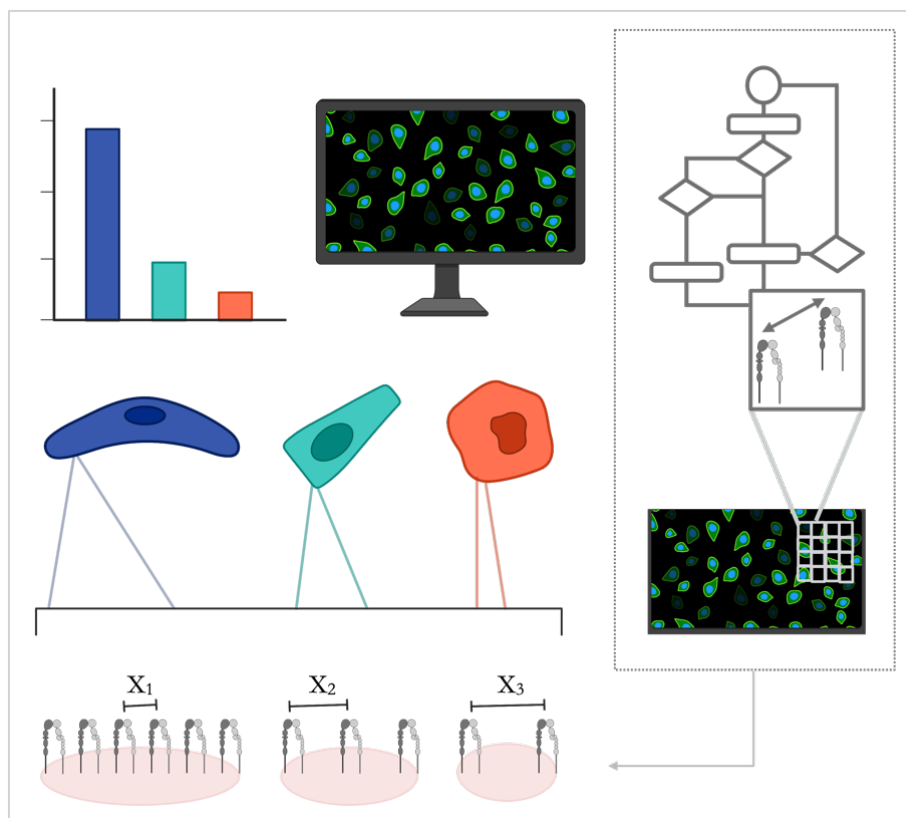


Figure 2.1 Chapter overview. Combining Cell binding assay and image processing methods in establishing a workflow to model integrin  $\alpha_5\beta_1$  nearest neighbour inter-receptor spacing distributions.

## 2.2 Methods and materials

### 2.2.1 Materials

Unless otherwise specified, reagents were used as received without further modification. Deionized water obtained from a Milli-Q water purification system was used for all experiments. Penicillin/streptomycin (Cat.No. 15140122), DMEM+GlutaMAX (Cat.No. 31966021), Fetal Bovine Serum (Cat.No. 10500064), DPBS (Cat.No. 14040091) and BSA 7.5% solution (Cat.No. 15260037) were purchased from Life Technologies EU BV. All buffers were filtered with 0.22 $\mu$ m PES syringe filters (Cat.No. 431229, Corning) or PES bottle filters (Cat.No. 431097, Corning). Hela Ohio cells were obtained from SuNMIL Lab, EPFL and CHO from EPFL Protein Facility. HUVEC (Cat.No. C2517AS), Reagent Pack™ Subculture Reagents (Cat.No. CC-5034) and EGM2 endothelial cell growth medium-2 bulletKit (Cat.No. CC-3162) was purchased from Lonza, Basel, Switzerland. 0.05% Trypsin-EDTA (Cat.No. 25300054) was purchased from Gibco. 96 well ibidi angiogenesis  $\mu$ -plates (Cat.No. 89646) were purchased from Vitaris AG. BlockAid blocking solution (Cat.No. B10710) was purchased from Invitrogen. Rabbit anti-Integrin alpha 5 antibody EPR7854 (ab150361) 1:200, Recombinant Rabbit IgG, monoclonal (Cat.No. ab172730) 1:1'500, Goat Anti-Rabbit IgG H&L Alexa Fluor® 488 (Cat.No. ab150077) 1:500, and Goat Anti-Mouse IgG H&L Alexa Fluor® 488 (Cat.No. ab150113) 1:500 were purchased from abcam. Integrin alpha 5/CD49e Antibody (SNAKA51) (Cat.No. NBP2-50146) 1:1000 was purchased from Novus Biologicals. Mouse IgG2a kappa, clone eBM2a, eBioscience (Cat.No. 15287367) and 4%PFA (Cat.No. 15424389) was purchased from Fisher Scientific. Poly-L-lysine solution (Cat.No. P4832) was purchased from Merck.

## 2.3 Cell Binding Assay

### 2.2.2 Experimental Procedure

HUVEC, CHO and HeLa cells were seeded in 96 well ibidi angiogenesis  $\mu$ -plate. Cells were incubated overnight at 37°C, 5% CO<sub>2</sub>, 95% relative humidity. When relevant, cells were incubated in media supplemented with activator (DTT 3mM, Mn<sup>2+</sup> 1mM, SNAK primary antibody 1 $\mu$ g mL<sup>-1</sup>, or a combination of Mn<sup>2+</sup> 1mM and SNAK primary antibody 1 $\mu$ g mL<sup>-1</sup>) for 45 mins. All the following steps were performed at room temperature. Cells were fixed in 2% PFA for 15min, washed with DPBS, and blocked for 1h with BlockAid blocking solution. The cells were then incubated on a shaker for 1h with the respective primary antibodies diluted in BlockAid. Cells were then washed with DPBS supplemented with 3%BSA and incubated with the respective secondary antibodies diluted in BlockAid for 1h.

### 2.2.3 Calibration Method

96 well ibidi angiogenesis  $\mu$ -plates were coated with poly-L-lysine (PLL) for 1h and washed with DPBS prior to incubation with a serial dilution of the Alexa Fluor® 488 conjugated secondary antibodies for calibration of antibody concentrations in experimental wells. Calibration wells were washed with DPBS prior to fluorescence measurements.

### 2.2.4 Data acquisition

Fluorescence intensities were measured on the BioTek™ Cytation 5™ Cell Imaging Multi-Mode Reader, BioTek Instruments, Inc. using the Gen5 software, Version 3.10. Monochromators were used to measure the fluorescence intensities of the Alexa Fluor® 488 secondary antibodies (BioTek, Ex/Em 495(10)/519(10)).

### 2.2.5 Fluorescence microscopy

Fluorescence microscopy was conducted on the BioTek™ Cytation 5™ Cell Imaging Multi-Mode Reader, BioTek Instruments, Inc. using the Gen5 software, Version 3.10. A GFP filter cube (BioTek Instruments, Inc., Ex/Em 469/525, LED Part Number 1225001) was used to image the cells stained with the Alexa Fluor® 488 secondary antibodies. A 20X PL FL Phase (Olympus, LUCLFLN 20X) phase objective was used. Imaging settings were kept constant across cell lines when comparing different conditions. Dimensions 4X images : 1'224 x 904 pixels (0.619 pixels  $\mu\text{m}^{-1}$ ) Dimensions 20X images : 1'224 x 904 pixels (3.115 pixels  $\mu\text{m}^{-1}$ )

## 2.3 Integrin $\alpha_5\beta_1$ activation

In the following section, we analyse the impact of different activation methods for integrin  $\alpha_5\beta_1$  activation, notably divalent cation  $\text{Mn}^{2+}$ ,<sup>18,20,21</sup> an activation inducing antibody SNAKA51<sup>11</sup> and reducing agent dithioeritol (DTT)<sup>13</sup> but not recombinant integrins<sup>22,23</sup> on integrin cluster distribution. We conduct this analysis to determine the activation method best suited for use in our future studies. This is as integrin conformation, clustering and spatial distribution is initiated and influenced by integrin activation methods employed.<sup>24,25</sup>

## 2.4 Integrin $\alpha_5\beta_1$ activation with monoclonal antibody SNAKA51 and $\text{Mn}^{2+}$

Integrin monoclonal antibodies function and epitope location have been reviewed by Byron et al.<sup>26</sup> and Su et al.<sup>25</sup> For our study with activated integrin  $\alpha_5\beta_1$ , we have the following requirements in the use of activating antibodies, notably that the (i) antibody binding epitope be distant from the ligand binding site, i.e. the integrin  $\alpha_5\beta_1$  headpiece to prevent encountering potential steric hindrance in future studies and (ii) antibody be specific to the integrin  $\alpha_5\beta_1$  dimer to prevent cross-activation and ligand binding from other  $\beta_1$  containing integrin dimers in our future assays. Our requirements ruled out majority of the available antibodies activating integrin  $\alpha_5\beta_1$  due to the antibody binding epitope location in the headpiece region and/or on the integrin  $\beta_1$  subunit.<sup>26,27</sup> The prevalence of the integrin  $\beta_1$  subunit in forming heterodimers with 12 different integrin  $\alpha$  subunits out of the 24 integrin heterodimers lacks the specificity in activating solely integrin  $\alpha_5\beta_1$ .<sup>28</sup> We were thus led to employ an integrin  $\alpha_5$  subunit activating antibody, SNAKA51.<sup>11</sup>

The activating antibody SNAKA51 was first produced by Clark et al.<sup>11</sup> and was shown to induce clustering of integrin  $\alpha_5\beta_1$ , mimicking the formation of fibrillar adhesions, i.e. inducing matrix formation. The SNAKA51 antibody binding epitope location, in the calf regions of the  $\alpha_5$  subunit induces a conformational change in the integrin legs that primes the integrin to bind to its ligand.<sup>11,25</sup> Accordingly, the SNAKA51 antibody selectively recognises integrin conformations in



subsets of adhesions, primarily to those associated with matrix formation and integrin translocation.<sup>11</sup> In short, the SNAKA51 antibody favours the recognition of the ligand-bound integrin  $\alpha_5\beta_1$  as it binds preferentially to extended conformations of the integrin  $\alpha_5\beta_1$ .<sup>29</sup> Furthermore, the SNAKA51 antibody binding affinity is increased with the addition of  $Mn^{2+}$  and its ligand<sup>11,29</sup> in good agreement with the conformational changes reported for the integrin  $\alpha_5\beta_1$ .<sup>12,19,25</sup> A concentration of SNAKA51 antibody of  $1\mu\text{M mL}^{-1}$  was sufficient in inducing FN incorporation in the matrix and is the concentration used in our experiments.<sup>11</sup> As reported, we compared the distribution of integrin  $\alpha_5\beta_1$  receptors when activated and in its' native state.<sup>11</sup> When used together with the SNAKA51 antibody and otherwise,  $Mn^{2+}$  was added at a concentration of 1mM in accordance with literature.<sup>12,21,30</sup>

## 2.5 Integrin $\alpha_5\beta_1$ activation via DTT disulfide bond reduction of cysteine-rich domain

The lower leg region of the  $\beta_1$  integrins subunit, i.e. the EGF-like domains has cysteine-rich repeats.<sup>31-34</sup> The tight intermodule linkage in this region is reportedly necessary in transmitting signals, such as activation, from the membrane to the headpiece, the site for ligand binding.<sup>34</sup> As such, antibodies that bind to this region serve to activate the integrin for ligand binding or probe activation specific integrin conformations.<sup>26,35,36</sup> Investigation of the EGF-like domains confirm the formation of disulfide bonds within the repeats.<sup>34</sup> DTT, a reducing agent, was found to reduce two disulfide bonds within the cysteine-rich domain, leading to a global conformational change in both  $\alpha$  and  $\beta$  subunits. This study in the context of integrin  $\alpha_{IIb}\beta_3$  led to the opening of the integrin ligand binding sites.<sup>13</sup> Another study showed that the reduction of a long-range disulfide bond in this region induced a conformational change of the integrin to an active state.<sup>37</sup> We decided to use a concentration of DTT of 3mM for our analysis based on a report in shifts in overall integrin conformation in the aforementioned study.<sup>13</sup>

## 2.6 Integrin $\alpha_5\beta_1$ activation analysis

The HUVECs imaged under different activation conditions were seeded at the same densities, Figure 2.2. The difference in the effect of the respective activation conditions both on HUVEC morphology and integrin  $\alpha_5\beta_1$  distribution is pronounced. The fluorescence localisation observed is in good agreement with the initial report of the SNAKA51 labelling integrin  $\alpha_5\beta_1$  at farther edge of focal adhesions, distal from the cell perimeter and at the sites of fibrillar adhesion.<sup>11</sup>

When dithiothreitol (DTT) activated, Figure 2.2 (B) the HUVECs were seen to retract in area, with regions of clustered integrin  $\alpha_5\beta_1$  flanking the nucleus, located in most cases, distal from the periphery of the cell. The lack of HUVEC spreading in the presence of large clusters of adhesions is in good agreement with an initial study on the influence of disulphide reducing agents on integrin mediated cell adhesion where DTT treated cells adhered but did not spread on FN substrates.<sup>38</sup>  $Mn^{2+}$  treated HUVECs, Figure 2.2 (C) maintained similar morphology and integrin  $\alpha_5\beta_1$  distribution when compared to HUVECs in resting conditions, Figure 2.2 (A) with an arguably

unnoticeable enrichment of pre-existing integrin  $\alpha_5\beta_1$  clusters. These findings are consistent with reports in literature of  $Mn^{2+}$  alone being unable to alter the conformation of integrin  $\alpha_5\beta_1$ .<sup>12,19</sup> As such, the sole  $Mn^{2+}$  activating condition is insufficient in driving the translocation of the integrin  $\alpha_5\beta_1$  to form new clusters of fibrillar adhesions. Integrin  $\alpha_5\beta_1$  clusters and cell morphology in HUVEC were indistinguishable between SNAKA51 staining both alone, Figure 2.2 (D) and in combination with  $Mn^{2+}$ , Figure 2.2 (E) This would be consistent with reports of  $Mn^{2+}$  increasing the affinity of integrin  $\alpha_5\beta_1$  for its ligand, with activating antibodies and ligands inducing conformational changes that could drive integrin  $\alpha_5\beta_1$  translocation.<sup>12,25</sup> Clusters of integrin  $\alpha_5\beta_1$  were observed over the entirety of the HUVEC cell surface, distributed in dot-like or in streak-like manners typical of fibrillar adhesion, away from the cell periphery.<sup>39</sup> The lack of marked integrin  $\alpha_5\beta_1$  fibrillar adhesions flanking the nuclei of cells could be attributed partially to the lack of clear boundaries from surrounding adhesions, distribution of the receptors between new clusters of adhesions and potential endocytosis of “pre-activated” liganded integrin  $\alpha_5\beta_1$ .<sup>40,41</sup> HUVEC were also more spread in SNAKA51 activating conditions, potentially resulting from the SNAKA51 enrichment of integrin  $\alpha_5\beta_1$  on the cell surface.

The difference in staining between the HUVEC in resting conditions, i.e. not activated and SNAKA51 activated cells was marked, confirmed the translocation of integrin  $\alpha_5\beta_1$  to fibrillar adhesions. The pattern of SNAKA51 staining observed in HUVECs reflects a previous report of SNAKA51 staining in ovarian carcinoma cells, with subnuclear tensin-rich adhesions in centrally located, well defined patches.<sup>40</sup> This pattern of SNAKA51 staining in HUVECs in resting conditions however, was unlike the streak-like adhesions observed in fibroblasts reported in literature,<sup>11</sup> making it likely to be cell type dependent. As the SNAKA51 antibody has preference for integrin  $\alpha_5\beta_1$  open-extended conformations,<sup>11</sup> the integrin  $\alpha_5\beta_1$  within clusters likely adopt this conformation in a ligand-bound as a result of HUVEC “inside-out” signalling. Of note, HUVECs have high expression levels of integrin  $\alpha_5\beta_1$  as they are key modulators of endothelial cell function in regulating cell engagement with the ECM.<sup>42</sup>

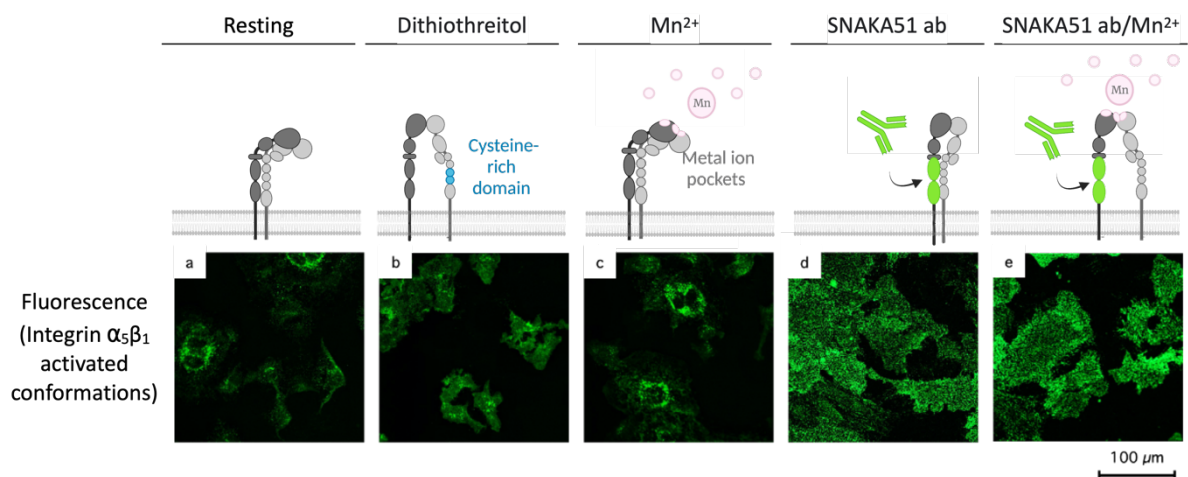


Figure 2.2 Methods for integrin activation. Fluorescence microscopy images show the resulting staining of the SNAKA51 (a) in resting conditions (b) DTT (c)  $Mn^{2+}$  (d) SNAKA51 (e) SNAKA51 and  $Mn^{2+}$ .

In deciding on an activation method to use, we had to consider the compatibility of the activation method with our future experimental setup, the nature of the activation method, its' resemblance to native activation and the specificity of the mechanism of activation. Whilst we did not screen for a range of time points and concentrations in DTT activation, we decided to proceed by alternative means of integrin  $\alpha_5\beta_1$  activation. This decision was based on (i) a lack of literature specific to DTT activation of the integrin  $\alpha_5\beta_1$  dimer, especially in terms of its' resulting conformations and ligand binding abilities, (ii) the lack of specificity in the mechanism of activation, i.e. the reduction being aspecific to the integrin  $\alpha_5\beta_1$  dimer and the disulphide reduction probably affecting multiple proteins on the cell surface and (iii) the deviation of results from DTT activation both in literature<sup>13</sup> and from our own observations of cell morphology and integrin  $\alpha_5\beta_1$  distribution compared to native cell states. From our observations of the inability of  $Mn^{2+}$  to direct translocation of the integrin  $\alpha_5\beta_1$  and reports from literature of unaltered integrin  $\alpha_5\beta_1$  conformations,  $Mn^{2+}$  alone was not considered a viable option for integrin activation for our experiments.

We decided to employ the SNAKA51 antibody as an activating method for integrin  $\alpha_5\beta_1$  in our studies as we gather that SNAKA51 priming of the integrin  $\alpha_5\beta_1$  to a ligand competent form would be sufficient to compensate for any loss in ligand affinity from the absence of  $Mn^{2+}$  in our experimental conditions. Moreover, the SNAKA51 binding epitope is specific to the integrin  $\alpha_5\beta_1$  and is situated far from the ligand binding site, unlikely in sterically hindering liganded DNA NP binding. Also, reported resulting conformations in negative stainings of the isolated integrin  $\alpha_5\beta_1$  in complex with the RGD peptide<sup>14</sup> and SNAKA51 antibody<sup>25</sup> did not deviate far from isolated integrin  $\alpha_5\beta_1$  conformations.<sup>12</sup> In our experimental conditions, precipitation observed in our buffers supplemented with  $Mn^{2+}$ , presumably from high salt concentration due to the necessary use of  $Na^+$  and/or  $Mg^{2+}$  in maintaining DNA NP stability led us to discontinue the use of  $Mn^{2+}$ . We note, however that SNAKA51 binding affinity is increased with the addition of  $Mn^{2+}$  and that EDTA used in our buffer systems, reportedly does not affect its binding ability.<sup>11</sup> Also, activating cells with the SNAKA51 antibody in the absence of  $Mn^{2+}$  could result in looser packed integrin clusters according to evidence of tighter distributions of integrin  $\alpha_5\beta_1$  in nascent adhesions in the presence of  $Mn^{2+}$ .<sup>43</sup> The effect of SNAKA51 activation will be tested on HUVEC, CHO and HeLa prior to modelling of integrin  $\alpha_5\beta_1$  inter-receptor distances.

### 2.6.1 Integrin $\alpha_5\beta_1$ expression & implications

Respective integrin heterodimer function can be traced to cell-type dependent expression levels making them ideal candidates for super-selective targeting.<sup>44-46</sup> Integrin  $\alpha_5\beta_1$  implicated in cell proliferation and angiogenesis essential for endothelial cell function<sup>47</sup> has reportedly a loss in polarisation upon epithelial malignant transformation.<sup>48</sup> Also, overexpression of integrin  $\alpha_5\beta_1$  in cervical cancer was correlated with negative chemotherapeutic response and recurrence.<sup>49,50</sup> Otherwise, epithelial upregulation in integrin  $\alpha_5\beta_1$  expression is associated with inflammatory response<sup>48,51,52</sup> and active proliferation.<sup>53</sup> Given this information, we investigate the relative integrin  $\alpha_5\beta_1$  expression levels in HUVEC (endothelial), CHO (epithelial) and HeLa (epithelial carcinoma) cells for future studies probing inter-receptor spacing and distribution.

## 2.6.2 Integrin $\alpha_5\beta_1$ expression across different cell types

Our cell repertoire of endothelial HUVEC, epithelial CHO and malignant epithelial HeLa, depicted in Figure 2.3 provides us with sufficiently diverse cells and integrin  $\alpha_5\beta_1$  expression levels for the analysis of integrin  $\alpha_5\beta_1$  receptor distribution for use in investigating the influence of integrin ligand spatial presentation on receptor binding.

The non-conformation specific integrin  $\alpha_5$  EPR7854 antibody staining, Figure 2.3 (G-I) is a control included for integrin  $\alpha_5\beta_1$  expression levels in resting conditions, i.e. regardless of integrin  $\alpha_5\beta_1$  receptor conformation. The integrin  $\alpha_5\beta_1$  staining observed with hotspots around the nucleus account for non-clustered and/or unliganded integrin  $\alpha_5\beta_1$  across the surface and clustered receptors being mostly liganded in adhesions.<sup>11</sup>

The staining of the HUVEC, CHO and HeLa with the non-functional integrin  $\alpha_5$  antibody, Figure 2.3 (G-I) compared with the activation specific SNAKA51 in resting conditions Figure 2.3 (D-F) have staining patterns that overlap. Given recent information of the distribution in conformations of integrin  $\alpha_5\beta_1$  in resting conditions,<sup>12,19,25</sup> it is likely that the antibodies stain for a variety of integrin  $\alpha_5\beta_1$  conformations leading to this observation. Robust deductions based on EPR7854 antibody binding epitope on the staining observed cannot be made as it is proprietary. Nevertheless, the diffuse staining observed with the EPR7854 on cells in resting conditions with hotspots of binding that are more marked than the SNAKA51 staining of CHO and HeLa cells, Figure 2.3 (E-F vs H-I) in resting conditions is consistent with EPR7854 staining of a broader range of conformations due to its non-functional nature compared to the SNAKA51 which likely is more stringent in its recognition of integrin  $\alpha_5\beta_1$  conformations. As for HUVECs, when comparing the SNAK versus EPR7854 antibody staining, Figure 2.3 (D, G) the same conclusions can be drawn albeit with a more distinct separation between clusters of adhesions and more pronounced SNAKA51 staining in the former. The overall higher integrin  $\alpha_5\beta_1$  expression levels in HUVEC compared to CHO and HeLa is a plausible reason for the difference. It should be noted that the differences in intensities of staining between the EPR7854 and SNAKA51 could also arise from the different primary-secondary antibody systems in use. The preferential staining of regions of the cell periphery, where nascent adhesions localise versus peripheral to the nuclear region where fibrillar adhesions localise observed EPR7854 antibody is consistent with reports of integrin  $\alpha_5\beta_1$  localisation, with larger clusters in the latter.<sup>11,54,55</sup>

HUVEC activated and stained by SNAKA51 displayed a streak-like staining morphology typical of fibrillar adhesions and in good agreement with initial findings with the SNAKA51 antibody.<sup>11</sup>

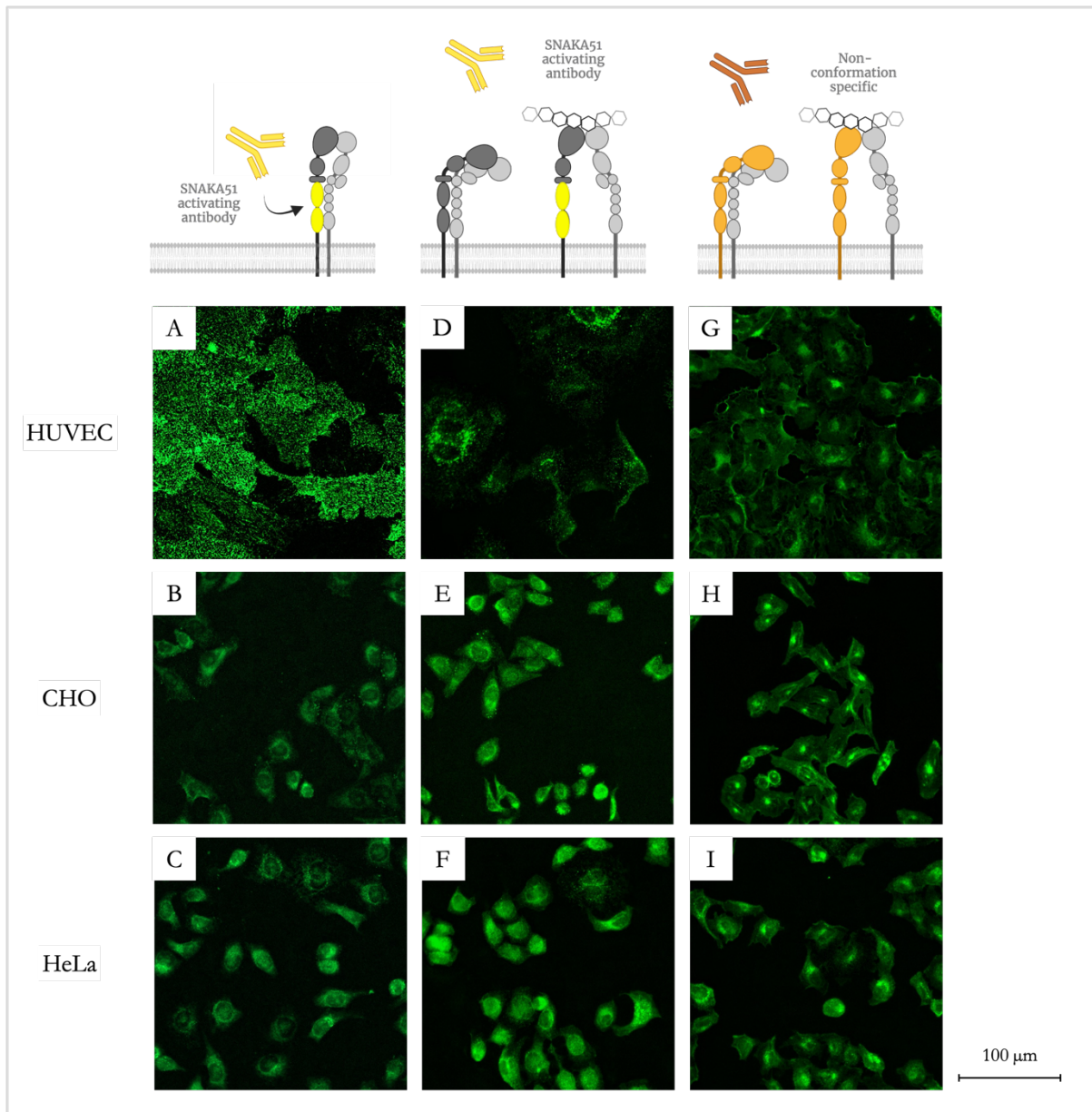


Figure 2.3 Analysis of integrin  $\alpha_5\beta_1$  receptor on HUVEC, CHO and HeLa in “chased” versus resting conditions.

Top row : HUVEC; Middle row : CHO; Bottom row : HeLa cells. (A-C : Cells activated and stained with SNAKA51 antibody; D-F : Cells in resting conditions, stained with SNAKA51 antibody; G-I Cells in resting conditions stained with  $\alpha_5$  antibody EPR7854)

SNAKA51 staining in CHO and HeLa cells in resting conditions, Figure 2.3 (E-F) display a more diffuse pattern of staining when compared to the activated cells, also previously reported.<sup>11</sup> The activated cells on the other hand, Figure 2.3 (B-C) have staining predominantly in distinct locations, flanking the nuclei of the cells. However, in Figure 2.3 (H-I) these patterns appear brighter on the CHO and HeLa cells in resting conditions that could be explained by subsequent integrin endocytosis when activated.<sup>40,41</sup> Ligand-engaged integrin  $\alpha_5\beta_1$  were reported to be endocytosed from regions below the nucleus, with these integrin  $\alpha_5\beta_1$  having similar conformations to those activated by the SNAKA51 antibody.<sup>25,40,41</sup> Our analysis of the

redistribution of integrin  $\alpha_5\beta_1$  upon SNAKA51 activation set the stage for subsequent modelling of integrin  $\alpha_5\beta_1$  inter-receptor nearest neighbour distances.

### 2.6.3 Workflow in establishing the model of integrin $\alpha_5\beta_1$ distributions

We set out to establish a theoretical method to interrogate the integrin  $\alpha_5\beta_1$  nearest neighbour spatial distributions from cell types (HUVEC, CHO and HeLa) of different integrin  $\alpha_5\beta_1$  overall expression levels. The resting versus SNAKA51 activated HUVEC, CHO and HeLa cells were subjected to a workflow for the modelling of integrin  $\alpha_5\beta_1$  interreceptor distributions, detailed below. The cell binding assay, Figure 2.5 (A) performed on the HUVEC, CHO and HeLa were subjected to both fluorescence intensity measurements and fluorescence microscopy. The fluorescence intensity measurements performed and quantities of the secondary antibodies in the respective conditions were derived from an established calibration curve. An assumption of 1:1 binding was employed in the ratio of secondary antibody to receptor binding.

### 2.6.4 Cell binding assay data analysis

Raw data obtained from fluorescence intensity measurements were treated as follows:

- (i) Background subtraction from maximum buffer intensities in control wells.
- (ii) Scaling of intensities across plates with dilutions of stock solutions of Alexa Fluor® 488 secondary antibodies.
- (iii) Fluorescence intensities of experimental wells were converted to concentrations via a calibration curve. The curve was plotted from the serial dilution of Alexa Fluor® 488 secondary antibodies immobilized on PLL coated wells plateaued at higher concentrations. The plateau obtained indicated complete surface coverage.
- (iv) A method was adapted from a previous report for surface characterisation.<sup>56</sup> Since the path length and molar absorptivity is constant across samples, we are able to derive the concentration of the experimental samples from the Beer-Lambert Law, denoted in Equation (1), from the linear regime of the curve. Linear regression was applied to the linear regime of the curve prior, Figure 2.4.

$$(1) \quad A = \epsilon lc$$

A is absorbance with no units,  $l$  is the path length of the sample,  $\epsilon$  is the molar absorptivity with units of  $L \text{ mol}^{-1} \text{ cm}^{-1}$  and  $c$  is the concentration of the compound in solution, expressed in  $\text{mol L}^{-1}$  or M for molarity.

- (v) The relative concentrations of secondary antibodies obtained in experimental wells were converted to the number of receptors,  $n_R$  via the following Equation (2). A ratio

of 1:1 was applied to estimate the number of integrin  $\alpha_5\beta_1$  receptors with respect to the number of Alexa Fluor® 488 secondary antibodies in experimental wells.

$$(2) n_R = cV_{\text{sample}}N_A$$

$c$  is the concentration of the compound in solution, expressed in mol L<sup>-1</sup> or M for molarity,  $V_{\text{sample}}$  is the volume of sample in the well in L and  $N_A$  is Avogadro's number,  $N_A = 6.02214076 \times 10^{23}$

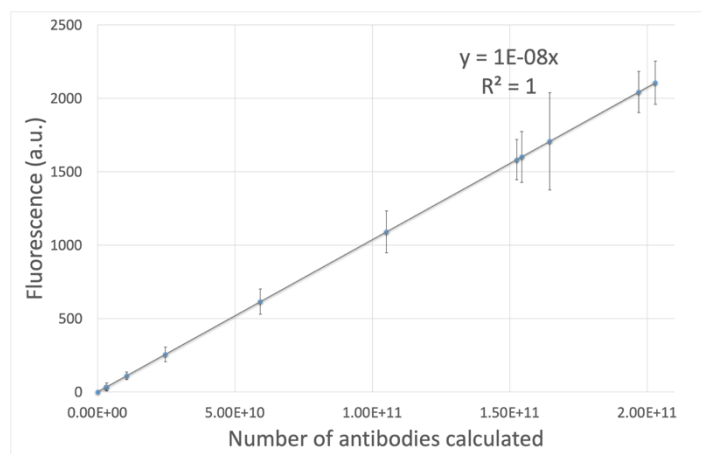


Figure 2.4 SNAKA51 antibody calibration for receptor concentration.

### 2.6.5 Image Processing based Mathematical Model of integrin $\alpha_5\beta_1$ distribution

For the modelling of receptor distributions, 3 images were selected at random per condition. Fiji software<sup>57</sup> and Wolfram Mathematica was used for the following steps.

- (i) Images of cells for the individual conditions were trained with the Trainable Weka Segmentation Fiji plugin.<sup>58</sup> This generated classifier models distinguishing between cell pixels and background pixels for the respective conditions. This was later used in the Weka analysis Fiji plugin developed in house, detailed in Appendix 2.8.1, depicted in Figure 2.5 (B)
- (ii) The number of integrin  $\alpha_5\beta_1$  receptors was evenly distributed across images, corrected for relative cell area to image area between stitched images of the entire well and individual images within the dataset. The corrected number of integrin  $\alpha_5\beta_1$  receptors was inserted into a Wolfram Mathematica<sup>59</sup> script Appendix 2.8.2 depicted in Figure 2.5 (C).
- (iii) In the Wolfram Mathematica script in Appendix 2.8.2 depicted in Figure 2.5 (C), histograms of the individual pixel intensities from the respective images are plotted and fitted to for normal distributions. Pixel intensity values lower than that of the intersection of the distributions are set zero as the normal distribution of lower pixel

intensities, attributed to cell autofluorescence. The intensities of the pixels in the image is summed. The intensity value attributed per receptor is then calculated by total pixel intensity of an image by the corrected number of integrin  $\alpha_5\beta_1$  receptors previously calculated. The integrin  $\alpha_5\beta_1$  receptors are distributed by pixel intensity and the inter-receptor distances within a pixel ( $3.115 \text{ pixels } \mu\text{m}^{-1}$ ) are calculated assuming an even distribution between pixel intensities, factoring a jamming limit of  $\sim 0.55^{60,61}$  and considering a conservative integrin receptor diameter of 10 nm.<sup>62</sup> For visualisation purposes, heat maps were generated of the modelled images to demonstrate the localisation of the fluorescent signal and the variation in intensity across cell lines and areas. Histograms of the resultant distributions of frequency of spacings are plotted. The normalized distributions of modelled integrin  $\alpha_5\beta_1$  receptors spacings are the plotted in Figure 2.6

Confocal microscopy analysis of spatially constrained integrin staining. (A) Representative overview for non-activated cells (B) Representative overview for activated cells. Images show the DNA-analytes in red (Cy5 label), antibody-stained integrin in green (Alexa 488) and the nucleus in blue (DAPI). Scale bar = 30  $\mu\text{m}$  (C) Quantification of selective binding, in resting conditions and in activated state. Plotted is the globally normalized intensity of scaffold present within the cell boundaries from a Z-projection of confocal images, corrected for background. Data is quantified from nine independent image stacks containing multiple cells per image.

(iv)

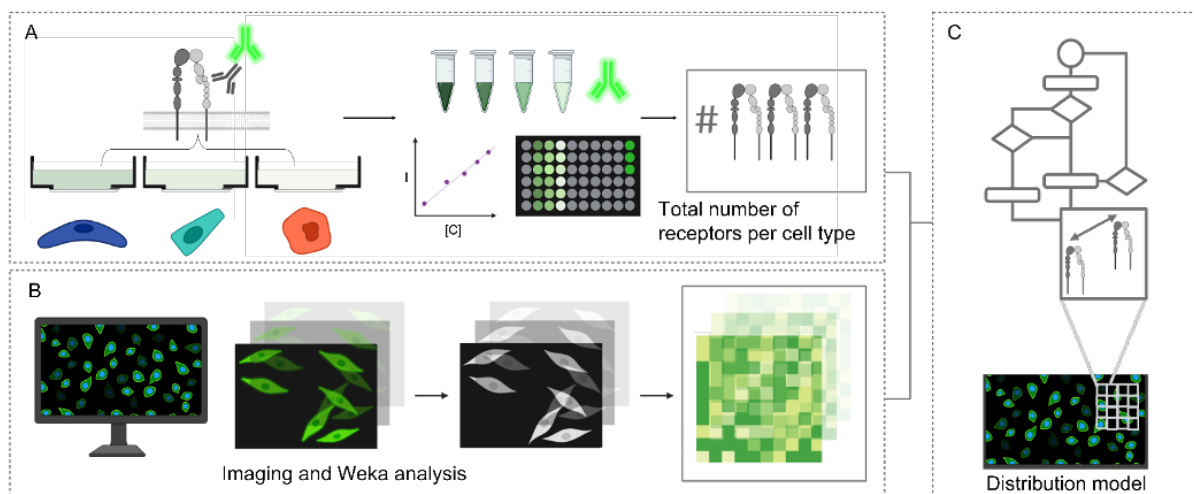


Figure 2.5 Workflow in modelling integrin  $\alpha_5\beta_1$  receptors distributions in HUVEC, CHO and HeLa. (A) Cell binding assay (B) Fluorescence microscopy & Image Processing by Weka Analysis (C) Mathematical model of integrin  $\alpha_5\beta_1$  distribution of interreceptor spacings.

The difference between SNAKA51 staining of HUVEC that are activated versus in resting conditions is explained by the relative proportions of integrin  $\alpha_5\beta_1$  adopting active conformations on the cell surface.<sup>63</sup> Cells were previously reported to maintain overall integrin  $\alpha_5\beta_1$  expression levels, with varying proportions of integrin conformations dependent on activation state.<sup>63</sup>



### 2.6.6 Modelled integrin $\alpha_5\beta_1$ nearest neighbour receptor spatial distributions

The model depicted in Figure 2.6 Confocal microscopy analysis of spatially constrained integrin staining. (A) Representative overview for non-activated cells (B) Representative overview for activated cells. Images show the DNA-analytes in red (Cy5 label), antibody-stained integrin in green (Alexa 488) and the nucleus in blue (DAPI). Scale bar = 30  $\mu\text{m}$  (C) Quantification of selective binding, in resting conditions and in activated state. Plotted is the globally normalized intensity of scaffold present within the cell boundaries from a Z-projection of confocal images, corrected for background. Data is quantified from nine independent image stacks containing multiple cells per image.

shows the distribution of receptors between image replicates fell within the same range of each other and between resting and activated conditions. A limit of 60nm was set to cap the distributions and defined the limits of ligand presentation on our DNA NPs. The decision was also based on reports of integrins requiring a minimum of four ligands within 60nm to enable cell spreading<sup>64,65</sup> and clustering that occurs below 70nm.<sup>66</sup> In proportion to the increased in active integrin  $\alpha_5\beta_1$  expression levels from HeLa to CHO then HUVEC, the modelled integrin  $\alpha_5\beta_1$  inter-receptor spacings resulted in distributions that are more tightly clustered, i.e. HUVEC mostly in the ranging from being in contact to 20nm, CHO from 10nm to 40nm and HeLa ranging from 20nm and beyond.

The spacings modelled in Figure 2.6 between the integrin  $\alpha_5\beta_1$  receptors might deviate as the receptors are evenly distributed across a plane, not considering distributions along the z-axis that occurs on the cell membrane in addition to the conservative 10nm conservative receptor diameter used. As the model distributes receptors evenly within pixels, deviations could be expected from the plotted distributions resulting from the even distribution, depending on the clustering conditions. Higher expression levels of the integrin  $\alpha_5\beta_1$  result in more tightly packed receptors within a pixel, leading to less deviations from the modelled distributions. For instance, as our target  $\alpha_5\beta_1$  integrin receptors reside predominantly in fibrillar adhesions upon activation<sup>11</sup> i.e. clusters

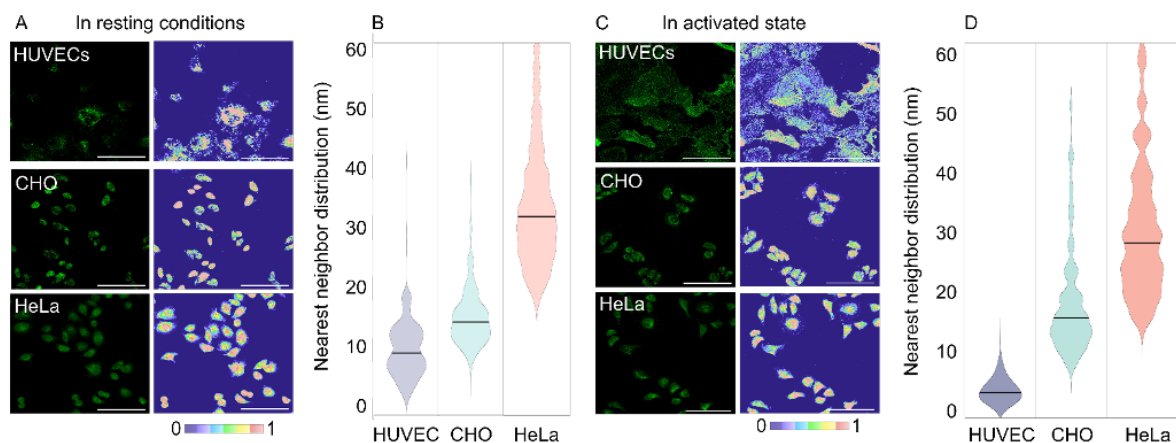


Figure 2.6 Confocal microscopy analysis of spatially constrained integrin staining. (A) Representative overview for non-activated cells (B) Representative overview for activated cells. Images show the DNA-analytes in red (Cy5 label), antibody-stained integrin in green (Alexa 488) and the nucleus in blue (DAPI). Scale bar = 30  $\mu\text{m}$  (C) Quantification of selective binding, in resting conditions and in activated state. Plotted is the globally normalized intensity of scaffold present within the cell boundaries from a Z-projection of confocal images, corrected for background. Data is quantified from nine independent image stacks containing multiple cells per image.

that are longer and thicker<sup>67,68</sup> (in the  $\mu\text{m}$  range) than that of nascent ( $<1\mu\text{m}$  in size) or focal adhesions ( $1-5\mu\text{m}$  in size),<sup>66</sup> the targeted clusters likely encompass several pixels, leading to less deviation from the modelled spacings. It is likely the case in our interpretation of HUVEC integrin  $\alpha_5\beta_1$  interreceptor spacings compared to that of CHO and HeLa. As a result, any distinct integrin  $\alpha_5\beta_1$  clusters formed within pixels will not be modelled accurately. Hence, densely packed receptor small sized clusters within a pixel will have underestimated interreceptor spacings in this model. Shifts between the modelled distributions and reality could also be explained by the assumptions made in the workflow, methods detailed in 2.6.6. Otherwise, the model only plots the distribution of the receptor spacings with respect to the nearest neighbour. The actual distribution of integrin  $\alpha_5\beta_1$  interreceptor spacings beyond the first neighbour likely falls in a range overlapping the larger spacings of distributions and beyond. The proportions of those distributions with respect to the nearest neighbour interreceptor spacings cannot be surmised from this dataset.

## 2.7 Conclusions

Briefly, the three cell types show an increasing integrin spacing was observed from  $\sim 10$  to  $\sim 20$  to  $\sim 30$  nm for HUVEC to CHO to HeLa, respectively. The results of the modelled distributions of integrin  $\alpha_5\beta_1$  receptor spacings suggest sufficiently diverse expressions levels across the cell types. From the model, we conclude that the different integrin  $\alpha_5\beta_1$  expression levels observed across cell types HUVEC, CHO and HeLa could have the ability to cluster receptors with increasing inter-receptor spacings in the sub-60nm regime. The modelled regimes show sufficient distinction between integrin  $\alpha_5\beta_1$  spatial regimes for ligand spatial targeting on the nanoscale. This provides a platform for investigating the modelled integrin  $\alpha_5\beta_1$  spacings with our liganded DNA scaffolds in following studies.

Reporting on a potential link between the spatial distributions of the integrin  $\alpha_5\beta_1$  with respect to expression levels could shed light on the mechanisms of clustering and signalling. The debate on the protumoural versus tumour suppressive role of the integrin  $\alpha_5\beta_1$  receptor in cancer and/or other diseases can be investigated in the influence of receptor clustering/spacing of respective cells.<sup>44,69</sup> The resulting selectivity in integrin targeting can guide the design of integrin  $\alpha_5\beta_1$  expression based therapies. The spatial distribution of the integrin  $\alpha_5\beta_1$  receptors can also be investigated in the context of 2D versus 3D cell culture matrices, facilitating the translation of cell cultures into more physiologically relevant settings.<sup>66</sup> The distributions of integrin  $\alpha_5\beta_1$  interreceptor spacings has the potential to also enhance our understanding of force transduction within adhesions and on the cell as a whole, as well as the dynamics in the diffusion of integrins on the cell surface.<sup>70,71</sup> Lastly, endocytic pathways of spatially distinct integrin  $\alpha_5\beta_1$  adhesion can be investigated with particles confined to the modelled spacings probing the localisation of different clusters of adhesions.<sup>72</sup>

## 2.8 Appendix

### 2.8.1 Weka Analysis Fiji Plugin Script

```

1 '''
2 This is a script to use after images have been segmented using Weka segmentation or a similar technique that only separates background/foreground.
3 It takes as input the fluorescent images with the data of interest, the brightfield images to perform Weka segmentation on and the Weka model file. It outputs three things:
4 A pixel value histogram for each image with foreground and background split.
5 Cell probabilities from the Weka segmentation (to be reused to save time).
6 And the masks used to segment the image.
7 '''
8
9 #@ File(label="Input directory of brightfield", description="Select the directory with input brightfield images to use in weka.", style="directory") inputDirBFW
10 #@ File(label="Input directory of fluorescent", description="Select the directory with input fluorescent images to take data from.", style="directory") inputDirFluoW
11 #@ File(label="Output directory", description="Select the output directory.", style="directory") outputDirW
12 #@ File(label="Model file", description="Select the location of the .model file.", style="file") modelFileW
13 #@ Boolean(label="Use existing cell probabilities", description="Check if Weka model has already been applied and cell probabilities images exist.") useProb
14 #@ Float(label="Select model certainty", description="Threshold for the probability images to be converted into mask.", min=0, max=1) threshCertainty
15
16 from ij import IJ, ImagePlus
17 from ij.io import FileSaver
18 from ij.plugin import ImageCalculator
19 from ij.process import ImageConverter
20 from trainableSegmentation import WekaSegmentation
21
22 import os
23 import csv
24
25
26 ''' FUNCTIONS '''
27 def save_as_tif(iplus, outDirectory):
28     '''
29     Saves an ImagePlus in the location specified by outDirectory
30     '''
31     outputFn = os.path.join(outDirectory, iplus.title + ".tif")
32     FileSaver(iplus).saveAsTiff(outputFn)
33     IJ.log("====Weka Analysis==== Saved image to: " + outputFn)
34
35 def to_csv(data, header, filename, outDirectory):
36     '''
37     Saves the specified data into outDirectory
38     '''
39     #output filename
40     outfn = os.path.join(outDirectory, filename)
41
42     #write data lines in the csv
43     with open(outfn, "wb") as csv_file:
44         csv_writer = csv.writer(csv_file, delimiter=',')
45         csv_writer.writerow(header)
46         for row in data:
47             csv_writer.writerow(row)
48
49     # Takes a cell probability image and transforms it into a binary image that can be used as a mask
50     '''
51     #remove potential DUP, if image is duplicated (which it should to avoid unwanted modifications) and then remove the file ending
52     iplus.title = imageTitle + "_mask"
53
54     #threshold image with a set value which represents the probability of that pixel to be a cell
55     IJ.setThreshold(iplus, threshCertainty, 1, "Black & White")
56     IJ.run(iplus, "Convert to Mask", "")
57
58     #perform binary operations to make mask better
59     IJ.run(iplus, "EDM Binary Operations", "iterations=2 operation=dilate")
60     IJ.run(iplus, "EDM Binary Operations", "iterations=2 operation=erode")
61
62     #save image for later
63     save_as_tif(iplus, masksDirString)
64
65     return iplus
66
67 def analyse(iplus, mask):
68     '''
69     With the original cell image and the mask created with create_mask(), applies analysis to get histogram of foreground and also background.
70     '''
71     all_data = []
72
73     #write header for the csv file
74     header = ['Region', 'Area (px)']
75     header.extend(['hist_'+str(i) for i in range(256)])
76
77     #foreground
78     foreground = ic.run("and create", iplus, mask)
79     hist = foreground.getProcessor().getHistogram()
80     hist[0] = 0 #we remove the pixel with value of 0 to get rid of the background so it doesn't hinder our data
81     if gotCalibration:
82         data = ["Foreground", sum(hist), sum(hist)*cal.pixelWidth*cal.pixelHeight]
83     else:
84         data = ["Foreground", sum(hist)]
85
86     data.extend(hist)
87     all_data.append(data)
88
89     #background
90     background = ic.run("zero create", iplus, mask)
91     hist = background.getProcessor().getHistogram()
92     hist[-1] = 0 #we remove the pixel with value of 255 to get rid of the foreground so it doesn't hinder our data
93     if gotCalibration:
94         data = ["Background", sum(hist), sum(hist)*cal.pixelWidth*cal.pixelHeight]
95     else:
96         data = ["Background", sum(hist)]
97
98     data.extend(hist)
99     all_data.append(data)
100
101     #write header for the csv file
102     if gotCalibration:
103         header = ['Cell number', 'Area (px)', 'Area (unit^2)'] #suddenly impossible to write µm due to encoding when it worked fine before, no other options work but to ignore it
104     else:
105         header = ['Cell number', 'Area (px)']
106
107     header.extend(['hist_'+str(i) for i in range(256)])
108
109     to_csv(all_data, header, imageTitle + ".csv", os.path.join(outputDirString, "csv"))
110 ''' END '''
111
112 ''' BEGINNING ROUTINE '''
113 #shorthand for weka (cuter)
114 weka = WekaSegmentation()
115
116 #same for calculator
117 ic = ImageCalculator()

```

```

140
141 #get strings of the directories, and create them if non existant
142 inputDirBFString = inputDirBFW.getCanonicalPath()
143 inputDirFluoString = inputDirFluow.getCanonicalPath()
144 outputDirString = outputDirW.getCanonicalPath()
145 probDirString = os.path.join(outputDirString, "cell_probabilities")
146 csvDirString = os.path.join(outputDirString, "csv")
147 masksDirString = os.path.join(outputDirString, "masks")
148 modelFileString = modelFileW.getCanonicalPath()
149
150 for dirString in [probDirString, csvDirString, masksDirString]:
151     if not os.path.exists(dirString):
152         os.mkdir(dirString)
153         IJ.log("----Weka Analysis---- Created output directory: " + dirString)
154
155 #load the classifier to use on the images only if probabilities don't already exist
156 if not useProb:
157     IJ.log("----Weka Analysis---- Loading classifier")
158     weka.loadClassifier(modelFileString)
159     IJ.log("----Weka Analysis---- Classifier loaded")
160
161 gotCalibration = False
162 ''' END '''
163
164 ''' BATCH LOOP '''
165 #loop around each image and apply the classification, with counter
166 c = 0
167 for imageFn in os.listdir(inputDirBFString):
168     if imageFn.endswith(".tif") or imageFn.endswith(".jpg") or imageFn.endswith(".jpeg") or imageFn.endswith(".png"):
169         imageBF = IJ.openImage(os.path.join(inputDirBFString, imageFn))
170         imageTitle = imageBF.title.rsplit(".", 1)[0] #title with file extension to use throughout the code
171         IJ.log("----Weka Analysis---- Processing " + imageTitle)
172
173         #get scaling to return values and perform analysis in units, prioritises global scale over local one (just like Fiji)
174         cal = imageBF.getCalibration()
175         if cal.unit=="pixel!":
176             gotCalibration = False
177             IJ.log("----Weka Analysis---- Did not find a scale. Consider setting a global or local scale if you want the data in something else than pixels.")
178         else:
179             gotCalibration = True
180             IJ.log("----Weka Analysis---- Found a scale, using that for calculations and particle analysis.")
181
182         #open fluorescent image and throw error if cannot find the fluorescent image
183         imageFluo = IJ.openImage(os.path.join(inputDirFluoString, imageFn))
184
185         if imageFluo is None:
186             IJ.log("----Weka Analysis---- Could not find fluorescent image for " + imageFn + ". Please make sure that it has the same name as the brightfield image.")
187             continue
188         else:
189             #convert to 8bit to be sure that values are in normal range
190             ImageConverter(imageFluo).convertToGray8()
191
192         c += 1
193         #if cell probabilities already exist, use those instead of apply Weka which can take a long time
194         if useProb:
195             cellProbImage = IJ.openImage(os.path.join(probDirString, imageTitle + "_cell_probability.tif"))
196         else:
197             cellProbImage = apply_weka(imageBF.duplicate())
198
199         mask = create_mask(cellProbImage)
200         analyse(imageFluo.duplicate(), mask)
201
202 IJ.log("----Weka Analysis---- Found and processed " + str(c) + " images")
203 ''' END '''

```

## 2.8.2 Mathematical Predictions of Integrin $\alpha_5\beta_1$ Receptor Distribution Script

```

In[ ]:= SetDirectory[NotebookDirectory[]]
Out[ ]:= C:\Users\pb1lep\Desktop\P51_HUVEC_8BIT10IMAGES\ALLWEKA_NOAREACORRECTION

In[ ]:= "C:\Users\pb1lep\Desktop\"
Out[ ]:= C:\Users\pb1lep\Desktop\

```

Set the name of the file to perform calculations on.

```

dataFn = "Data_FilePath";
imageFn = "Image_FilePath";

```

## Pre calculations

These new lines import/calculate import values that are used throughout the notebook.

### Scale

The pixel length is the length of one side of a pixel. This is only needed for the receptor spacing calculations.

```

In[ ]:= pixelLength =

```

## Starting index

Because the data can contain two areas if it came with units, we calculate the starting index of the histogram data.

```
In[ ]:= header = Import[dataFn][[1]];
      strtIdx = Position[header, "hist_0"][[1, 1]]
```

## Background value

First, we import the data from Fiji where the histograms for background and foreground are kept. We take the background histogram.

```
In[ ]:= rawHistData = Import[dataFn][[2 ;;]];
      backgroundHistData = rawHistData[[2, strtIdx ;;]];
```

Since backgroundHistData is a histogram we multiply each value by their occurrence leading us to allBackgroundValues. We use values from 0 to 255 here because it should coincide with the integrated density calculation found below.

```
In[ ]:= allBackgroundValues =
      Flatten[MapThread[ConstantArray, {Range[0, 255], backgroundHistData}]];
```

We can then take the mean of this to get the average background value. This value will be between 0 and 255.

```
In[ ]:= backgroundValue = N[Mean[allBackgroundValues]]
```

```
Out[ ]:=
```

## Receptors per pixel value

The value totalReceptors is taken directly from prior calculations. Integrated density will sum all the pixel values for each cell, subtracting the background value (calculated above) with it. When we subtract the background value, if pixels in the cells are underneath this level, we just put it to 0. pixelValues is just a flattened list of all the pixel values that are in the cell calculated from the histogram in the csv file.

It is important that the totalReceptor number is calculated from values of 0 to 255 as this is how the integrated density is calculated.

```
totalReceptors =;
```

```
In[ ]:= foregroundHistData = rawHistData[[1, strtIdx ;;]];
      pixelValues = Flatten[MapThread[ConstantArray, {Range[0, 255], foregroundHistData}]];
```

```
In[ ]:= integratedDensity = N[Total[If[# < 0, 0, #] & /@ (pixelValues - backgroundValue)]]
```

```
Out[ ]:=
```

```
In[ ]:= valuePerReceptor = integratedDensity / totalReceptors
```

```
Out[ ]:=
```

## Image in modified colour

### Calculating the gradient based on the image values

First, import the histogram data for background and foreground for one image.

Preparation of the data to fit the Gaussian. The data will be of the shape  $\{\{0, x_0\}, \{1/255, x_1\}, \{2/255, x_2\}, \dots\}$ . The  $x_n$  are normalised. Note the 255x in gaussianModel, this is to ensure that the scaling between the ranges 0-1 and 0-255 is respected.

```

In[ ]:= dataToFit = Partition[
  Riffle[Range[0, 1, 1 / 255], foregroundHistData / Total[foregroundHistData]], 2];
  gaussianModel = PDF[NormalDistribution[ $\mu$ ,  $\sigma$ ], 255 * x]

```

$$\text{Out[ ]:= } \frac{e^{-\frac{(255x-\mu)^2}{2\sigma^2}}}{\sqrt{2\pi}\sigma}$$

Find the fit for the gaussian.

```

In[ ]:= fit = FindFit[dataToFit, gaussianModel, { $\mu$ ,  $\sigma$ }, x]
Out[ ]:= { $\mu \rightarrow$  ,  $\sigma \rightarrow$  }

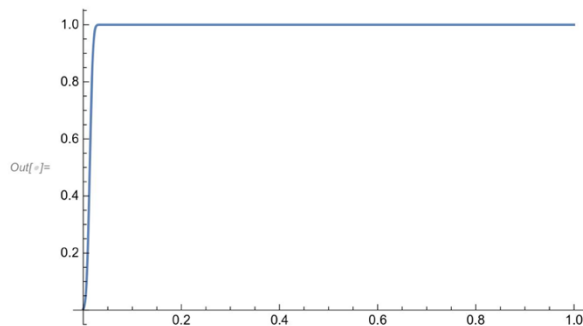
```

Use that fit to calculate the cumulative distribution which will serve as the value converter in our custom colour gradient. In the future, and to ensure comparability between the images, the cdf should stay the same between images. To do so, just save the  $\mu$  and  $\sigma$  values from any image and change the fit variable above.

```

In[ ]:= cumulativeGaussian = CDF[NormalDistribution[ $\mu$ ,  $\sigma$ ] /. fit, 255 * x];
  colourValueConverter = Function[{x}, Evaluate[cumulativeGaussian]];
  Plot[colourValueConverter[x], {x, 0, 1}]

```



Creating the colour gradient and the composition of it and the value converter from above.

```

In[ ]:= gradient[x_] := Blend[{{0., #1}, {0.152941, #2}, {0.152941, #3},
  {0.321569, #4}, {0.321569, #5}, {0.490196, #6}, {0.490196, #7},
  {0.662745, #8}, {0.662745, #9}, {0.831373, #10}, {0.831373, #11}, {1., #12}}, x]
  customGradient[x_] := gradient[colourValueConverter[x]]

```

Some misc different gradients to try.

```

In[ ]:= (*
  customGradient[x_] := Blend[{{0., #1}, {0.152941, #2}, {0.152941, #3},
    {0.321569, #4}, {0.321569, #5}, {0.490196, #6}, {0.490196, #7},
    {0.662745, #8}, {0.662745, #9}, {0.831373, #10}, {0.831373, #11}, {1., #12}}, x];
  customGradient[x_] := Blend[{{0., #1}, {0.152941, #2}, {0.152941, #3},
    {0.321569, #4}, {0.321569, #5}, {0.490196, #6}, {0.490196, #7},
    {0.662745, #8}, {0.662745, #9}, {0.831373, #10}, {0.831373, #11}, {1., #12}}, x];
  customGradient[x_] := gradient[colourValueConverter[x]]
  *)

```

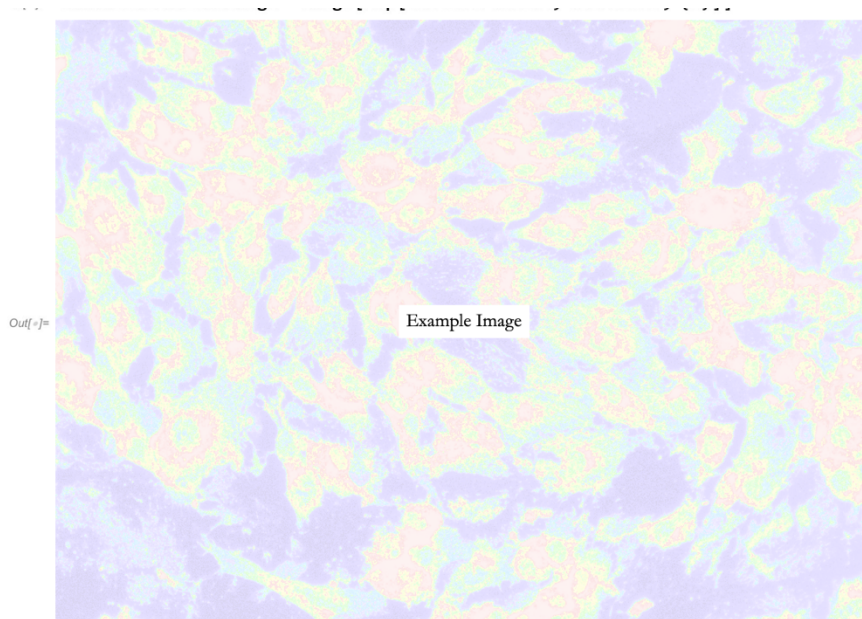
## Colouring the image

Import all the pixels from the image to colour. We take only the data of the image to turn it into an array of numbers from 0 to 1.

```

In[ ]:= allPixels = ImageData[Import[imageFn]];
In[ ]:= enhancedGradientImage = Image[Map[customGradient, allPixels, {2}]]

```



Export the image to whatever place/format you want.

```
In[ ]:= Export["visualisations/enhanced_gradient.png", enhancedGradientImage]
Out[ ]:= visualisations/enhanced_gradient.png
```

## Inter-receptor spacing histogram

First, let's define a function, `getSpacingHistograms[]`, which will calculate, for each pixel, the number of receptors that it should have in it. Further explanation is found inside the function.

```
In[ ]:= getSpacingHistograms[cellPixelsValues_, pixelArea_, fractionOccupied_] :=
  Block[{receptorsPerPixel, areaPerReceptor, spacingBetweenReceptors},
    (*first, for every pixel value, we remove the background,
    divide it by our valuePerReceptor and round it to get the number of
    receptors in each pixel, if the value is below 0 we set it to 0*)
    receptorsPerPixel = If[Round[#] <= 0, Nothing, Round[#]] & /@
      ((cellPixelsValues - backgroundValue) / valuePerReceptor);
    (*taking into account the fraction of the area of each pixel that a
    receptor can occupy, we calculate the areas for each receptors*)
    areaPerReceptor = (fractionOccupied pixelArea / #) & /@ receptorsPerPixel;
    (*we can then, assuming a circular occupation,
    calculate the distance for each receptor*)
    spacingBetweenReceptors = Sqrt[4 * areaPerReceptor / Pi];
    (*as is done further up in the notebook,
    we translate histogram values to a list of the occurrences and return this*)
    Flatten[MapThread[ConstantArray, {spacingBetweenReceptors, receptorsPerPixel}]]
  ]
```

We calculate the fraction of area of a pixel accessible to a receptor, factoring a jamming limit of 0.54. The calculated values of each pixel is plotted in a histogram.

```
In[ ]:= pixelArea = pixelLength^2;
fractionOccupied = .54;
spacingHists = getSpacingHistograms[pixelValues, pixelArea, fractionOccupied];
meanSpacingHists = Mean[spacingHists];
```

To check if the results are correct, `totalNumber` and the length of `spacingHists` should be roughly similar.

```
In[ ]:= totalReceptors
Length[spacingHists]
```

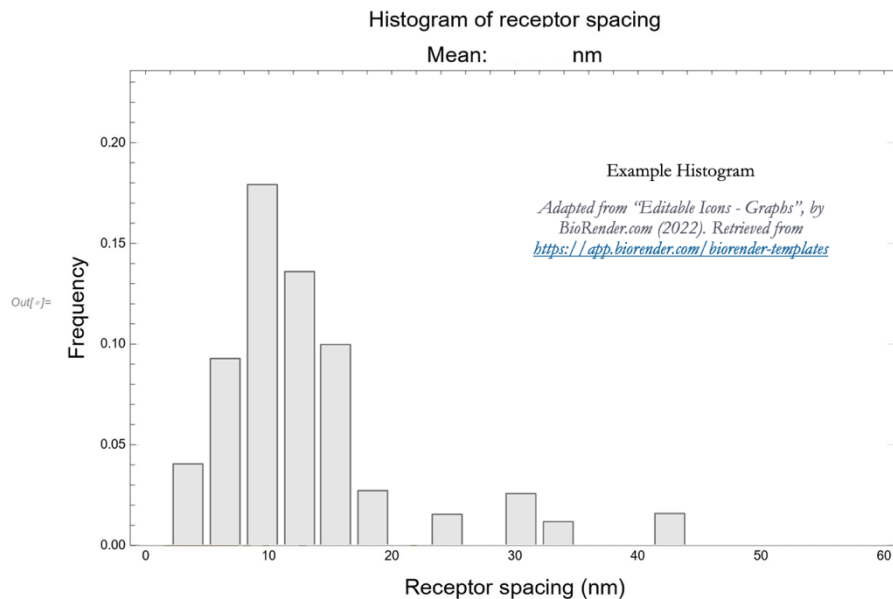
Out[ ]:=

Out[ ]:=

```

In[ ]:= receptorHist = Histogram[spacingHists, 40,
  "Probability", PlotRange -> {{0, 60}, Automatic}, FrameLabel ->
  {Style["Receptor spacing (nm)", Black, 15], Style["Frequency", Black, 15]},
  Frame -> True, GridLines -> Automatic, ImageSize -> Large,
  PlotLabel -> Style["Histogram of receptor spacing\nMean: " <>
  ToString[meanSpacingHists] <> "nm", Black, 15]]

```



Save the histogram wherever needed.

```

In[ ]:= Export["visualisations/receptor_histograms.png", receptorHist, ImageResolution -> 500]

```

```

Out[ ]:= visualisations/receptor_histograms.png

```

If you want to make histograms in another program, evaluate the next cell to save the histogram data into a csv file.

```

In[ ]:= binWidth = 10;
binStart = Min[spacingHists];
binEnd = Max[spacingHists] + binWidth;

In[ ]:= histList = HistogramList[spacingHists, {binStart, binEnd, binWidth}]

```

```

Out[ ]:=

```

```

In[ ]:= Export["visualisations/histogram_data.csv", histList]

```

```

Out[ ]:= visualisations/histogram_data.csv

```

## 2.9 Bibliography

1. Muro, S. Challenges in design and characterization of ligand-targeted drug delivery systems. *J. Control. Release Off. J. Control. Release Soc.* 164, 125–137 (2012).
2. Martinez-Veracochea, F. J. & Frenkel, D. Designing super selectivity in multivalent nano-particle binding. *Proc. Natl. Acad. Sci.* 108, 10963–10968 (2011).
3. Samaržija, I. et al. Integrin Crosstalk Contributes to the Complexity of Signalling and Unpredictable Cancer Cell Fates. *Cancers* 12, 1910 (2020).
4. Young, J. L. et al. Integrin Subtypes and Nanoscale Ligand Presentation Influence Drug Sensitivity in Cancer Cells. *Nano Lett.* 20, 1183–1191 (2020).
5. Dzobo, K. Integrins Within the Tumor Microenvironment: Biological Functions, Importance for Molecular Targeting, and Cancer Therapeutics Innovation. *OMICS J. Integr. Biol.* 25, 417–430 (2021).
6. Wickström, S. A., Radovanac, K. & Fässler, R. Genetic Analyses of Integrin Signaling. *Cold Spring Harb. Perspect. Biol.* 3, a005116 (2011).
7. Taherian, A., Li, X., Liu, Y. & Haas, T. A. Differences in integrin expression and signaling within human breast cancer cells. *BMC Cancer* 11, 293 (2011).



8. Baiula, M. et al. Selective Integrin Ligands Promote Cell Internalization of the Antineoplastic Agent Fluorouracil. *ACS Pharmacol. Transl. Sci.* 4, 1528–1542 (2021).
9. Millard, M., Odde, S. & Neamati, N. Integrin Targeted Therapeutics. *Theranostics* 1, 154–188 (2011).
10. Anderson, L. R., Owens, T. W. & Naylor, M. J. Structural and mechanical functions of integrins. *Biophys. Rev.* 6, 203–213 (2013).
11. Clark, K. et al. A specific  $\alpha 5\beta 1$ -integrin conformation promotes directional integrin translocation and fibronectin matrix formation. *J. Cell Sci.* 118, 291–300 (2005).
12. Schumacher, S. et al. Structural insights into integrin  $\alpha 5\beta 1$  opening by fibronectin ligand. *Sci. Adv.* 7, eabe9716 (2021).
13. Yan, B. & Smith, J. W. Mechanism of Integrin Activation by Disulfide Bond Reduction. *Biochemistry* 40, 8861–8867 (2001).
14. Structure of integrin  $\alpha 5\beta 1$  in complex with fibronectin. *EMBO J.* 22, 4607–4615 (2003).
15. Sun, X., Skorstengaard, K. & Mosher, D. F. Disulfides modulate RGD-inhibitable cell adhesive activity of thrombospondin. *J. Cell Biol.* 118, 693–701 (1992).
16. Shih, D. T., Edelman, J. M., Horwitz, A. F., Grunwald, G. B. & Buck, C. A. Structure/function analysis of the integrin beta 1 subunit by epitope mapping. *J. Cell Biol.* 122, 1361–1371 (1993).
17. Nagae, M. et al. Crystal structure of  $\alpha 5\beta 1$  integrin ectodomain: atomic details of the fibronectin receptor. *J. Cell Biol.* 197, 131–140 (2012).
18. Miyake, K., Yamashita, Y. & Kimoto, M. A calcium- or manganese-dependent epitope on the integrin  $\beta 1$  chain recognized by a unique mAb. *Int. Immunol.* 6, 1221–1226 (1994).
19. Miyazaki, N., Iwasaki, K. & Takagi, J. A systematic survey of conformational states in  $\beta 1$  and  $\beta 4$  integrins using negative-stain electron microscopy. *J. Cell Sci.* 131, jcs216754 (2018).
20. Dormond, O., Ponsonnet, L., Hasmim, M., Foletti, A. & Rügge, C. Manganese-induced integrin affinity maturation promotes recruitment of  $\alpha V\beta 3$  integrin to focal adhesions in endothelial cells: evidence for a role of phosphatidylinositol 3-kinase and Src. *Thromb. Haemost.* 92, 151–161 (2004).
21. Yanai, T., Shimo-Oka, T. & Ii, I. Manganese Ion Elicits a Binding Activity of Placenta Vitronectin Receptor to Fibronectin Cell-Binding Domain. *Cell Struct. Funct.* 16, 149–156 (1991).
22. Banères, J.-L., Roquet, F., Martin, A. & Parello, J. A Minimized Human Integrin  $\alpha 5\beta 1$  That Retains Ligand Recognition \*. *J. Biol. Chem.* 275, 5888–5903 (2000).
23. O’Toole, T. et al. Integrin cytoplasmic domains mediate inside-out signal transduction. *J. Cell Biol.* 124, 1047–1059 (1994).
24. Ali, O. et al. Cooperativity between Integrin Activation and Mechanical Stress Leads to Integrin Clustering. *Biophys. J.* 100, 2595–2604 (2011).
25. Su, Y. et al. Relating conformation to function in integrin  $\alpha 5\beta 1$ . *Proc. Natl. Acad. Sci. U. S. A.* 113, E3872–3881 (2016).
26. Byron, A. et al. Anti-integrin monoclonal antibodies. *J. Cell Sci.* 122, 4009–4011 (2009).
27. Humphries, M. J., Symonds, E. J. & Mould, A. P. Mapping functional residues onto integrin crystal structures. *Curr. Opin. Struct. Biol.* 13, 236–243 (2003).
28. Takada, Y., Ye, X. & Simon, S. The integrins. *Genome Biol.* 8, 215 (2007).
29. Askari, J. A. et al. Focal adhesions are sites of integrin extension. *J. Cell Biol.* 188, 891–903 (2010).
30. Sechler, J. L., Corbett, S. A. & Schwarzbauer, J. E. Modulatory Roles for Integrin Activation and the Synergy Site of Fibronectin during Matrix Assembly. *Mol. Biol. Cell* 8, 2563–2573 (1997).
31. Humphries, M. J. Integrin structure. *Biochem. Soc. Trans.* 28, 311–339 (2000).
32. Tamkun, J. W. et al. Structure of integrin, a glycoprotein involved in the transmembrane linkage between fibronectin and actin. *Cell* 46, 271–282 (1986).
33. Kishimoto, T. K., Hollander, N., Roberts, T. M., Anderson, D. C. & Springer, T. A. Heterogeneous mutations in the  $\beta$  subunit common to the LFA-1, Mac-1, and p150,95 glycoproteins cause leukocyte adhesion deficiency. *Cell* 50, 193–202 (1987).
34. Takagi, J., Beglova, N., Yalamanchili, P., Blacklow, S. C. & Springer, T. A. Definition of EGF-like, closely interacting modules that bear activation epitopes in integrin beta subunits. *Proc. Natl. Acad. Sci. U. S. A.* 98, 11175–11180 (2001).
35. Bazzoni, G., Shih, D.-T., Buck, C. A. & Hemler, M. E. Monoclonal Antibody 9EG7 Defines a Novel  $\beta 1$  Integrin Epitope Induced by Soluble Ligand and Manganese, but Inhibited by Calcium. *J. Biol. Chem.* 270, 25570–25577 (1995).
36. Takagi, J., Isobe, T., Takada, Y. & Saito, Y. Structural interlock between ligand-binding site and stalk-like region of beta1 integrin revealed by a monoclonal antibody recognizing conformation-dependent epitope. *J. Biochem. (Tokyo)* 121, 914–921 (1997).
37. Liu, Z. Y. et al. Characterization of signal transduction pathways in human bone marrow endothelial cells. *Blood* 90, 2253–2259 (1997).
38. Davis, G. E. & Camarillo, C. W. Regulation of integrin-mediated myeloid cell adhesion to fibronectin: influence of disulfide reducing agents, divalent cations and phorbol ester. *J. Immunol.* 151, 7138–7150 (1993).

39. Barber-Pérez, N. et al. Mechano-responsiveness of fibrillar adhesions on stiffness-gradient gels. *J. Cell Sci.* 133, jcs242909 (2020).
40. Rainero, E. et al. Ligand-Occupied Integrin Internalization Links Nutrient Signaling to Invasive Migration. *Cell Rep.* 10, 398–413 (2015).
41. Changede, R. & Sheetz, M. Integrin and cadherin clusters: A robust way to organize adhesions for cell mechanics. *BioEssays* 39, e201600123 (2017).
42. Hou, J., Yan, D., Liu, Y., Huang, P. & Cui, H. The Roles of Integrin  $\alpha 5\beta 1$  in Human Cancer. *OncoTargets Ther.* 13, 13329–13344 (2020).
43. Changede, R., Xu, X., Margadant, F. & Sheetz, M. P. Nascent Integrin Adhesions Form on All Matrix Rigidities after Integrin Activation. *Dev. Cell* 35, 614–621 (2015).
44. Gilcrease, M. Z. Integrin signaling in epithelial cells. *Cancer Lett.* 247, 1–25 (2007).
45. Sales, A. et al. Cell Type-Dependent Integrin Distribution in Adhesion and Migration Responses on Protein-Coated Microgrooved Substrates. *ACS Omega* 4, 1791–1800 (2019).
46. Mezu-Ndubuisi, O. J. & Maheshwari, A. The role of integrins in inflammation and angiogenesis. *Pediatr. Res.* 89, 1619–1626 (2021).
47. Rüegg, C., Dormond, O. & Mariotti, A. Endothelial cell integrins and COX-2: mediators and therapeutic targets of tumor angiogenesis. *Biochim. Biophys. Acta BBA - Rev. Cancer* 1654, 51–67 (2004).
48. Watt, F. M. Role of integrins in regulating epidermal adhesion, growth and differentiation. *EMBO J.* 21, 3919–3926 (2002).
49. Zhu, H. et al. Predictive role of galectin-1 and integrin  $\alpha 5\beta 1$  in cisplatin-based neoadjuvant chemotherapy of bulky squamous cervical cancer. *Biosci. Rep.* 37, BSR20170958 (2017).
50. Wang, H.-Y., Chen, Z., Wang, Z.-H., Wang, H. & Huang, L.-M. Prognostic Significance of  $\alpha 5\beta 1$ -integrin Expression in Cervical Cancer. *Asian Pac. J. Cancer Prev.* 14, 3891–3895 (2013).
51. Sheppard, D. Functions of Pulmonary Epithelial Integrins: From Development to Disease. *Physiol. Rev.* 83, 673–686 (2003).
52. Teoh, C. M., Tan, S. S. L. & Tran, T. Integrins as Therapeutic Targets for Respiratory Diseases. undefined (2015).
53. Taddei, I. et al. Integrins in Mammary Gland Development and Differentiation of Mammary Epithelium. *J. Mammary Gland Biol. Neoplasia* 8, 383–394 (2003).
54. Wozniak, M. A., Modzelewska, K., Kwong, L. & Keely, P. J. Focal adhesion regulation of cell behavior. *Biochim. Biophys. Acta BBA - Mol. Cell Res.* 1692, 103–119 (2004).
55. Strohmeyer, N., Bharadwaj, M., Costell, M., Fässler, R. & Müller, D. J. Fibronectin-bound  $\alpha 5\beta 1$  integrins sense load and signal to reinforce adhesion in less than a second. *Nat. Mater.* 16, 1262–1270 (2017).
56. Bastings, M. M. et al. From phage display to dendrimer display: Insights into multivalent binding. *J. Am. Chem. Soc.* 133, 6636–6641 (2011).
57. Schindelin, J. et al. Fiji: an open-source platform for biological-image analysis. *Nat. Methods* 9, 676–682 (2012).
58. Arganda-Carreras, I. et al. Trainable Weka Segmentation: a machine learning tool for microscopy pixel classification. *Bioinformatics* 33, 2424–2426 (2017).
59. Wolfram Mathematica. (Wolfram Research, Inc., 2021).
60. Adamczyk, Z. Modeling adsorption of colloids and proteins. *Curr. Opin. Colloid Interface Sci.* 17, 173–186 (2012).
61. Gajos, K., Szafraniec, K., Petrou, P. & Budkowski, A. Surface density dependent orientation and immunological recognition of antibody on silicon: TOF-SIMS and surface analysis of two covalent immobilization methods. *Appl. Surf. Sci.* 518, 146269 (2020).
62. Lepzelter, D., Bates, O. & Zaman, M. Integrin Clustering in Two and Three Dimensions. *Langmuir* 28, 5379–5386 (2012).
63. Saux, G. L., Magenau, A., Böcking, T., Gaus, K. & Gooding, J. J. The Relative Importance of Topography and RGD Ligand Density for Endothelial Cell Adhesion. *PLOS ONE* 6, e21869 (2011).
64. Schwartzman, M. et al. Nanolithographic Control of the Spatial Organization of Cellular Adhesion Receptors at the Single-Molecule Level. *Nano Lett.* 11, 1306–1312 (2011).
65. Cavalcanti-Adam, E. A., Aydin, D., Hirschfeld-Warneken, V. C. & Spatz, J. P. Cell adhesion and response to synthetic nanopatterned environments by steering receptor clustering and spatial location. *HFSP J.* 2, 276–285 (2008).
66. Maynard, S. A., Winter, C. W., Cunnane, E. M. & Stevens, M. M. Advancing Cell-Instructive Biomaterials Through Increased Understanding of Cell Receptor Spacing and Material Surface Functionalization. *Regen. Eng. Transl. Med.* 7, 533–547 (2021).
67. Yamada, K. M., Pankov, R. & Cukierman, E. Dimensions and dynamics in integrin function. *Braz. J. Med. Biol. Res. Rev. Bras. Pesqui. Medicas E Biol.* 36, 959–966 (2003).
68. De Pascalis, C. & Etienne-Manneville, S. Single and collective cell migration: the mechanics of adhesions. *Mol. Biol. Cell* 28, 1833–1846 (2017).
69. Schaffner, F., Ray, A. M. & Dontenwill, M. Integrin  $\alpha 5\beta 1$ , the Fibronectin Receptor, as a Pertinent Therapeutic Target in Solid Tumors. *Cancers* 5, 27–47 (2013).

70. Sun, Z., Costell, M. & Fässler, R. Integrin activation by talin, kindlin and mechanical forces. *Nat. Cell Biol.* 21, 25–31 (2019).
71. Sun, Z., Guo, S. S. & Fässler, R. Integrin-mediated mechanotransduction. *J. Cell Biol.* 215, 445–456 (2016).
72. Mana, G., Valdembri, D. & Serini, G. Conformationally active integrin endocytosis and traffic: why, where, when and how? *Biochem. Soc. Trans.* 48, 83–93 (2020).

## Chapter 3 Selective integrin $\alpha_5\beta_1$ targeting with rigid DNA scaffolds

In this chapter, we aim to engineer materials for the selective binding of receptors for improved efficacy in targeting systems. Our approach relies on matching ligand presentation to receptor spacing capitalising on the spatial tolerance of DNA nanotechnology.<sup>1,2</sup> Our experiments account for different receptor densities across cell types and states.<sup>3,4</sup> As depicted in Figure 3.1 we present RGD ligands for integrin  $\alpha_5\beta_1$  receptor binding probing regimes of spacing previously modelled in Chapter 2. We elaborate on the trends in RGD liganded DNA Scaffold binding observed via immunofluorescent confocal microscopy images across HUVEC, CHO and HeLa in resting versus activated conditions. For HUVEC and CHO, the data demonstrated an improved selectivity and localisation of binding for smaller spacings  $\sim 7$  nm and  $\sim 24$  nm, in good agreement with the model. A deviation from the mode predictions for HeLa was observed, indicative of a clustered, instead of homogeneous, integrin organization. Our findings demonstrate how low-technology imaging methods can guide the design of spatially controlled ligands to selectively differentiate between cell type and integrin activation state.

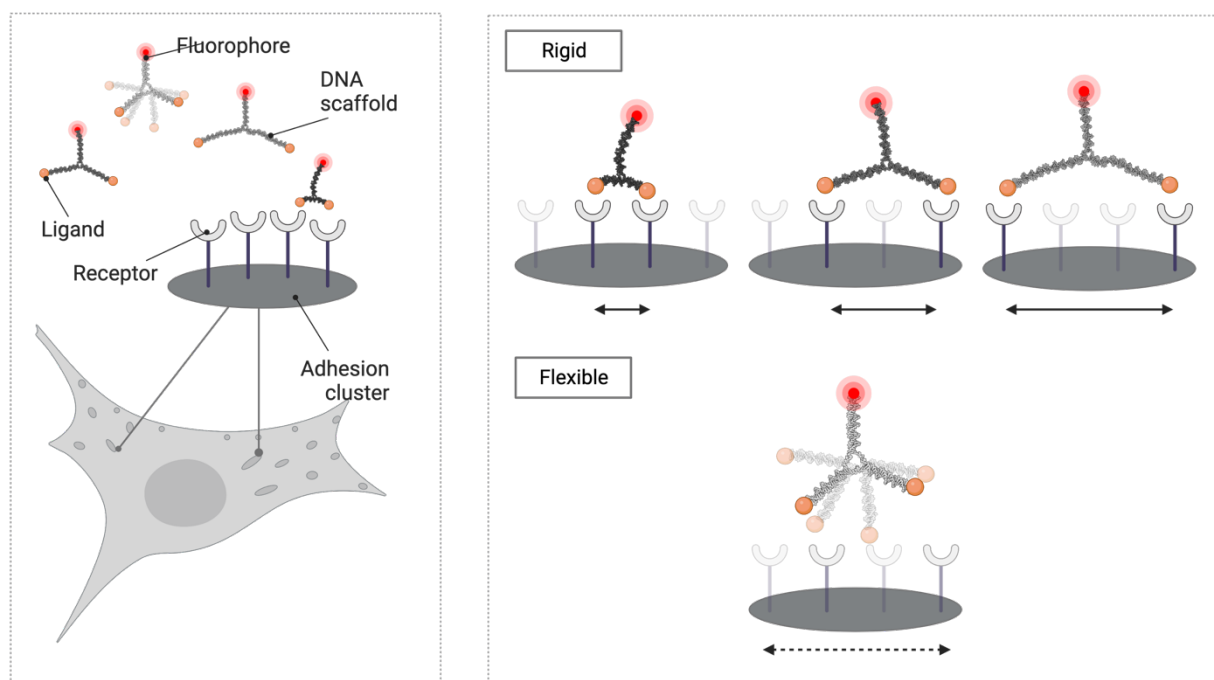


Figure 3.1 Chapter overview. Bivalent, rigid DNA scaffolds as probes of receptor spacing & rigidity. Depiction of receptor engagement with liganded bivalent, rigid DNA scaffolds.

As integrin  $\alpha_5\beta_1$  receptors been reported to be upregulated in certain diseases,<sup>5,6</sup> applications stemming from improve integrin  $\alpha_5\beta_1$  receptor targeting would span diagnostics,<sup>7</sup> cellular uptake,<sup>8</sup> drug delivery,<sup>9</sup> biomaterial design for tissue engineering applications.<sup>10,11</sup>

Citation: Kurisinkal, E.E.; Caroprese, V.; Koga, M.M.; Morzy, D.; Bastings, M.M.C. Selective Integrin  $\alpha_5\beta_1$  Targeting through Spatially Constrained Multivalent DNA-Based Nanoparticles. *Molecules* **2022**, *27*, 4968. <https://doi.org/10.3390/molecules27154968>

Author Contributions: Conceptualization, M.M.C.B., V.C. and E.E.K.; methodology, E.E.K.; software, V.C., and E.E.K.; validation, M.M.K. and E.E.K.; formal analysis, E.E.K.; investigation, E.E.K., M.M.K. and D.M.; resources, M.M.C.B.; data curation, E.E.K. and V.C.; writing—original draft preparation, E.E.K.; writing—review and editing, M.M.C.B.; visualization, E.E.K.; supervision, M.M.C.B.; project administration, M.M.C.B.; funding acquisition, M.M.C.B. All authors have read and agreed to the published version of the manuscript.

(Additional Contributions to Thesis) : AFM: C. Tekin.

### 3.1 Introduction

A minimum cell adhesion recognition site, the arginine-glycine-aspartate (RGD) sequence, was first discovered in FN by Pierschbacher & Ruoslahti in 1984.<sup>12,13</sup> Subsequent findings of integrins cell surface receptor recognition of the RGD motif led to a many studies involving RGD ligand-integrin receptor targeting systems.<sup>14-16</sup> In this study, we employ the RGD ligand to probe the distributions of integrin  $\alpha_5\beta_1$  receptors on the cell surface. We employ a bivalent, rigid DNA scaffold bearing RGD ligands to probe the distributions of spacings between integrin  $\alpha_5\beta_1$  receptor clusters on the cell surface. We investigate the trends in receptor organisation between the 3 cell types characterised in Chapter 2, namely, HUVEC, CHO and HeLa. The distributions of integrin  $\alpha_5\beta_1$  receptors between cells in an activated state versus in resting conditions in the ensemble of adhesion clusters is also detailed. We go on to show preliminary experiments with higher valency, rigid DNA scaffolds and the potential impact on targeting systems.

Our findings are posited as means to tailor the efficacy of cell surface receptor targeting systems, and in doing so reducing the propensity for off-targets. Finally, we discuss the limitations of our currents experiments and future perspectives addressing spacing and rigidity for biological applications.

### 3.2 Methods and materials

#### 3.2.1. Materials

Unless otherwise specified, reagents were used as received without further modification. Deionized water obtained from a Milli-Q water purification system was used for all experiments. Penicillin/streptomycin (Cat.No. 15140122), DMEM+GlutaMAX (Cat.No. 31966021), Fetal Bovine Serum (Cat.No. 10500064), DPBS (Cat.No. 14040091) and BSA 7.5% solution (Cat.No. 15260037) were purchased from Life Technologies EU BV. All buffers were filtered with 0.22 $\mu$ m

PES syringe filters (Cat.No. 431229, Corning) or PES bottle filters (Cat.No. 431097, Corning). Hela Ohio cells were obtained from SuNMIL Lab, EPFL and CHO from EPFL Protein Facility. HUVEC (Cat.No. C2517AS), Reagent Pack™ Subculture Reagents (Cat.No. CC-5034) and EGM2 endothelial cell growth medium-2 bulletKit (Cat.No. CC-3162) was purchased from Lonza, Basel, Switzerland. 0.05% Trypsin-EDTA (Cat.No. 25300054) was purchased from Gibco. 96 well ibidi angiogenesis  $\mu$ -plates (Cat.No. 89646) and ibidi  $\mu$ -Slide Angiogenesis Glass bottom (Cat.No. 81507) were purchased from Vitaris AG. Goat Anti-Rabbit IgG H&L Alexa Fluor® 488 (Cat.No. ab150077) 1:500, DAPI staining solution (Cat.No. ab228549) 1:1000 and Goat Anti-Mouse IgG H&L Alexa Fluor® 488 (Cat.No. ab150113) 1:500 were purchased from abcam. Integrin alpha 5/CD49e Antibody (SNAKA51) (Cat.No. NBP2-50146) (Live :1:1000; Fixed : 1:250) was purchased from Novus Biologicals. Mouse IgG2a kappa, clone eBM2a, eBioscience (Cat.No. 15287367), Tris Buffer, 2M, (Cat.No. BP1759), Piperazine-N,N'-bis(2-ethanesulfonic acid) 1M, PIPES (Cat.No. 15404879), Methanol (Cat.No. M/4060/PB17) Tris-borate-EDTA, TBE Buffer, (10X) (Cat.No. BP1333-1) and 4%PFA (Cat.No. 15424389) was purchased from Fisher Scientific. ( $\pm$ )-6-Hydroxy-2,5,7,8-tetramethylchromane-2-carboxylic acid, Trolox, 97% (Cat.No. 238813), 3,4-Dihydroxybenzoic acid, >97%, PCA (Cat.No. 37580), Protocatechuate 3,4-Dioxygenase from *Pseudomonas* sp., PCD (Cat.No. P8279), Dextran sulfate sodium salt from *Leuconostoc* spp. mol wt 6,500-10,000, (Cat.No. D4911), Sodium chloride solution 5M (Cat.No. S5150), Ethylene glycol-bis(2-aminoethylether)-N,N,N',N'-tetraacetic acid, EGTA (Cat.No. 200-651-2), Sucrose (Cat.No. S0389), Deoxyribonucleic acid, single stranded from salmon testes (Cat.No. D7656), 1-Hydroxybenzotriazole hydrate, HOBt (Cat.No. 711489), dichloromethane, DCM (Cat.No. 270997), Trifluoroacetic acid, TFA (Cat.No. T6508), Phenol (Cat.No. 33517), Diethyl ether (Cat.No. 32203), Dibenzocyclooctyne-maleimide, DBCO-maleimide, (Cat.No. 760668), Neuraminidase from *Clostridium perfringens* (C.-betawelchii) (Cat.No. N2876-6UN), Heparinase I and III Blend from *Flavobacterium heparinum* (Cat.No. H3917-50UN), Hyaluronidase from bovine testes Type I-S (Cat.No. H3506-100MG), CF™ 488A maleimide (Cat.No. SCJ4600016), Anhydrous Dimethyl sulfoxide, DMSO (Cat.No. 472301), and Magnesium Chloride solution 1M (Cat.No. M1028) was purchased from Merck. Ethylenediaminetetraacetic acid 0.5M, EDTA (Cat.No. J60292) and 1,2 ethanedithiol, EDT (Cat.No. L12865) was purchased from Alfa Aesar. Glycerol (Cat.No. AB113718), O-benzotriazole-N,N,N',N'-tetramethyluroniumhexafluorophosphate, HBTU (Cat.No. AB12886), diisopropylethylamine, DIPEA (Cat.No. AB182190) and N-methylpyrrolidine, NMP (Cat.No. AB182195) were purchased from ABCR. Tween-20 (Cat.No. BIT0803) and Tris hydrochloride, Tris-HCl (Cat.No. BIT1513) was purchased from Apollo Scientific. Potassium chloride (Cat.No. 6781.1), Agarose (Cat.No. 3810.2), Triethylamine, TEA (Cat. No. X875.2) and Sodium chloride (Cat.No. 3957.1) was purchased from Carl Roth. Fmoc protected peptides were purchased from Merck as follows : Fmoc-Cys(Trt)-OH (Cat.No. 8520080025), Fmoc-Gly-OH (Cat.No. 8520010025), Fmoc-Arg(Pbf)-OH (Cat.No. 8520670025), Fmoc-Ala-OH (Cat.No. 8520030025), Fmoc-Asp(OtBu)-OH, (Cat.No. 8520050025), Fmoc-Ser(tBu)-OH (Cat.No. 8520190025). Fmoc-Rink Amide MBHA resin (Cat.No. AS-20083) was purchased from AnapSpec. Argon ALPHAGAZ™ (Cat.No. P0022L50S2A001) was purchased from Air Liquide. ssDNA scaffold type p7560 (Cat.No. M1-30) was obtained from Tilibit. 40% acrylamide and bis-acrylamide solution 19:1, (Cat.No. 1610144) was purchased from Bio-Rad. Ammonium persulfate, APS (Cat.No. 231-786-5) was purchased from VWR. N,N,N',N'-tetramethylethylenediamine, TEMED (Cat.No. A1148), Gold Nucleic Acid Gel Stain (Cat.No.

S11494), SYBR™ Safe DNA Gel Stain, (Cat.No. S33102), GeneRuler Ultra Low Range DNA Ladder (Cat.No. SM1213), GeneRuler 50 bp DNA Ladder (Cat.No. SM0372), GeneRuler 100bp DNA Ladder (Cat.No. SM0241), 1kb Plus DNA Ladder (Cat.No. 10787018), 6X DNA Loading Dye (Cat.No. R0611), TriTrack DNA Loading Dye (Cat.No. R1161), Zeba™ Micro Spin Desalting Columns, 7K MWCO (Cat.No. 89883), Image-iT™ FX Signal Enhancer (Cat.No. I36933), Pierce™ C18 Spin Columns (Cat.No. 89870), Pierce™ Immobilized TCEP Disulfide Reducing Gel (Cat.No. 77712) and Precast Native Gels : 4-20% (Cat.No. XP04205BOX), 4-12% (Cat.No. XP04122BOX), 6% (Cat.No. XP00065BOX) were purchased from Thermo Fisher Scientific. Acetonitrile >99.9% HPLC grade, (Cat. No. FSHA/0627/17-4) was purchased from Chemie Brunschwig AG. Thin muscovite mica Grade V1, (Cat.No. PEL56) was purchased from Ted Pella.

### 3.2.2. ssDNA strands

All ssDNA strands listed below were ordered from Integrated DNA Technologies, Coralville, Iowa, USA, with modification when indicated in ssDNA Bivalent Scaffold strands and modifications 3.7.1 and 3.7.2.

### 3.2.3. Instruments

Reverse phase analytical High Pressure Liquid Chromatography (RP-HPLC) (Dionex Ultimate 3000 U-HPLC, Thermo Scientific) equipped with Hypersil Gold™ C18, 150x4 mm column (3 $\mu$ m diameter) was used for peptide and peptide conjugated characterisation. Peptide molecular weight was analysed by electrospray ionization mass spectrometry (ESI-MS) (LTQ Orbitrap ELITE ETD, ThermoFisher Scientific). HERMLE Z366 HK centrifuge was used for centrifugation steps. Agarose and Polyacrylamide (PAGE) gel electrophoresis were performed in or Biometra eco-mini gel tank (Analytic Jena). Gel images were acquired by the Bio-Rad ChemiDoc MP imaging system (Hercules, California, USA) and analysed with Bio-Rad ImageLab software. Fluorescence intensity measurements and imaging of samples were performed on the BioTek™ Cytation 5™ and Gen5 software, Version 3.10 (Winooski, Vermont, USA). ssDNA and dsDNA concentrations were acquired from the Quawell Q9000 nanodrop spectrometer. Annealing programs of DNA scaffolds were conducted on the Biometra trio thermocycler (Analytical Jena). AFM images of bivalent, rigid scaffolds were acquired in tapping mode in liquid on a Cypher VRS (Asylum Research Inc.) with a BioLever mini cantilever (BL-AC40TS-C2, Olympus). Confocal microscopy was conducted for monovalent experiments on a Leica SP8 IN1 with Lumencor Sola II LED, Laser illumination. Images were processed with Leica Application Suite X (LAS-X) software. Confocal imaging of rigid, bivalent DNA scaffolds was conducted on a Zeiss LSM980 with Colibri 5 illumination for fluorescence and ZEN Blue software version 3.4.91.

### 3.2.4. RGD Peptide Synthesis & Characterisation

Peptide synthesis of RGD peptides with a GC linker was conducted based on previously reported synthesis.<sup>17</sup> 65 $\mu$ mol Fmoc-based solid phase peptide synthesis (SPPS) was conducted of the following peptides (GRGDSGGGC, GRADSGGGC) on Fmoc-Rink Amide MBHA resin. The entire synthesis was conducted in solid phase synthesis vessels under a steady stream of Argon.

Fmoc deprotection was performed by mixing the resin in a 20% (v/v) NMP supplemented with 0.1M HOBt for five minutes. This was followed by six washing steps of NMP. For each amino acid coupling, four molar equivalents relative to resin loading of Fmoc-protected amino acid, four molar equivalents of HBTU in NMP and 16 molar equivalents of DIPEA in NMP were added to the reaction chamber and mixed at room temperature. The first 5 amino acid couplings were conducted for 1 hour and the remaining for 2 hours. The efficiency of coupling and deprotection was assessed as previously reported.<sup>18</sup> After the last deprotection and washing step, an additional washing step with 4 times 8mL of DCM was conducted. The resin was then dried under compressed air for 30 minutes. Peptide cleavage from the resin and removal of side chain protecting groups was carried out with the following cleavage cocktail for four hours. The 2mL cleavage cocktail was composed of 90% (v/v) TFA, 2.5% (v/v) Milli-Q, 2.5% (v/v) thioanisole, 2.5% (w/v) phenol, and 2.5% (v/v) EDT. Precipitation was conducted with cold diethyl ether, and incubated for 30 minutes at -20°C. The solution and precipitate was then centrifuged at 2000 x g for 20 minutes. The precipitate was washed with 40mL cold diethyl ether and the centrifugation step repeated. Then, the precipitate was dissolved in ddH<sub>2</sub>O, lyophilised and stored at -80°C in powder form. For CF488-peptide conjugation, peptide dissolved in Milli-Q was first added in a 1:1 (v/v) ratio to Pierce™ Immobilized TCEP Disulfide Reducing Gel and incubated on a shaking platform for 90mins. To separate the TCEP Gel from the reduced peptide sample, the mix was added to Pierce™ Spin Cups and centrifuged for 1minute at 1500 x g into microcentrifuge tubes containing the CF488-maleimide, in 1.2X molar excess.

### 3.2.5. RGD Peptide Characterisation

Peptide molecular weight was analysed by ESI-MS. m/z Calcd. [M+H]<sup>+</sup>: 764.29Da Obsd. [M+H]<sup>+</sup>: 764.31Da [M+2H]<sup>2+</sup>: 382.66Da (CGGGGRGDS) m/z Calcd. [M+H]<sup>+</sup>: 778.30Da Obsd. [M+H]<sup>+</sup>: 778.33Da [M+2H]<sup>2+</sup>: 389.67Da (CGGGGRADS). The peptides synthesised were characterised by RP-HPLC. A gradient of 15% to 75%B over 24 minutes was used with A: Milli-Q with 0.1% (v/v) TFA and B: acetonitrile with 0.1% (v/v) TFA. Peptide-CF488 conjugates were characterised on 4-20% Native Gels for 1h20, 120V.

### 3.2.6. ssDNA Antihandle-Peptide Conjugation

Peptides were conjugated to ssDNA strands with azide modification listed in 3.7.1 for eventual ligand functionalised ssDNA antihandle annealing of the DNA Scaffolds. All the following steps were conducted at room temperature. ssDNA was resuspended in 0.01XDPBS-10mM EDTA targeting a concentration of 300 $\mu$ M. Dibenzocyclooctyne (DBCO)-maleimide stock was prepared in anhydrous DMSO at 25mM, added in 4-fold molar excess to the ssDNA and incubated for 2h. In parallel, 2mg of peptide was dissolved in Milli-Q and added in a 1:1 (v/v) ratio to Pierce™ Immobilized TCEP Disulfide Reducing Gel and incubated on a shaking platform for 90mins. After incubation, Zeba™ Spin Desalting Columns 7K were used to remove excess DBCO-maleimide according to the manufacturer's instructions.<sup>3</sup> To separate the TCEP Gel from the reduced peptide sample, the mix was added to Pierce™ Spin Cups and centrifuged for 1minute at 1500 x g into microcentrifuge tubes containing the purified ssDNA-maleimide sample. The solution was incubated for 2h, characterised and stored at -20°C in solution. Peptides ligand



functionalised ssDNA antihandles were characterized by 20% Native PAGE and RP-HPLC. 2 $\mu$ M, 5 $\mu$ L samples were loaded on 20% Native PAGE gels and run for 2h30-3h30 hours at 150V. For RP-HPLC characterisation, a gradient of 15% to 75%B over 24 minutes was used with A: TEAA buffer 100mM, pH 7 and B: ACN.

### 3.2.7. Bivalent, Rigid DNA Scaffold Design & Characterisation

Bivalent, rigid DNA scaffolds were adapted from a publication from Mohri et al.<sup>19</sup> with sequence designs based on 4 base pair motifs. During the design, ssDNA sequences were submitted to NUPACK analysis of base pairing and structures formed from the interacting ssDNA sequences.<sup>20</sup> All bivalent scaffolds were subjected to 4-20% Native PAGE characterisation, 2h30, 120V. Ligand functionalised ssDNA antihandles were synthesised and characterised as detailed in 3.2.6.

### 3.2.8. Atomic Force Microscopy (AFM)

AFM images of bivalent, rigid scaffolds were acquired in tapping mode in liquid on a Cypher VRS (Asylum Research Inc.) with a BioLever mini cantilever (BL-AC40TS-C2, Olympus). For imaging, first, a 40 $\mu$ L drop of 100mM NiCl<sub>2</sub> was placed on freshly cleaved thin muscovite mica. After 1 minute of incubation, mica was rinsed by 20mL of Milli-Q water and dried by compressed air. 5 $\mu$ L of the Bivalent Scaffolds at 5nM was deposited upon the pre-treated mica and left briefly for absorption. Then, 20 $\mu$ L of Bivalent Scaffold Buffer (10mM MgCl<sub>2</sub>, 5mM TRIS, 1mM EDTA) was added on top of it. The cantilever was placed into the liquid cantilever holder and the ensemble was embedded in the cantilever chamber. The setpoint was maximized while preserving good tracking with a range of integral gain of 40. The raw data was processed with Gwyddion software (version 2.61) using the following steps: 1) Align Rows by Median of differences 2) Outlier removal by manual selection of Bivalent Scaffold Threshold height excluding superior heights 3) Interpolation of data under mask by solution of Laplace equation 4) Image segmentation with Otsu mask, polynomial level 1 excluding masked region 5) Application of Gwyddion net LUT.

### 3.2.9. Multivalent, Rigid DNA Scaffold preparation & characterisation

Multivalent, Rigid DNA Scaffold were prepared as detailed a publication by Eklund et al.<sup>21</sup> Ligand functionalised ssDNA antihandle were annealed in 3X molar excess per handle to the Multivalent, Rigid Scaffold was performed in a Thermal Cycler with the following program : Samples were heated to 37°C for 2h, cooled to 28°C over 12h and stored at 4°C. 5 $\mu$ L, 10nM samples were loaded on 1% agarose gels with 1kb Plus ladder as reference. Gels were run for 90 mins at 70V.

### 3.2.10. Monovalent-RGD Binding Assay

HUVEC were seeded in 96 well ibidi angiogenesis  $\mu$ -plate and incubated overnight at 37°C, 5% CO<sub>2</sub>, 95% relative humidity. The following morning, cells were incubated in full media

supplemented with activator SNAKA51 primary antibody  $1\mu\text{g mL}^{-1}$  for 1h. All the following steps were performed at room temperature. Cells were fixed in 2% PFA for 15 mins. Cells were then washed with DPBS, blocked in BlockingAid for 30 mins followed by Image-iT™ FX Signal Enhancer for 15 mins. CF488-RGD was then added to the cells and incubated for 1h. Cells were then washed and imaged by confocal microscopy. LUT Applied, CF488 : Green; DAPI : Blue.

### 3.2.11. Bivalent Scaffold Binding Assay

HUVEC, CHO and HeLa cells were seeded in 96 well ibidi angiogenesis  $\mu$ -plate. Cells were serum-starved incubated overnight at  $37^\circ\text{C}$ , 5%  $\text{CO}_2$ , 95% relative humidity. The following morning, cells were incubated in full media (supplemented with activator SNAKA51 primary antibody  $1\mu\text{g mL}^{-1}$  when stated) for 1h. All the following steps were performed at room temperature. Buffers used for fixation, staining and imaging were adapted from Strauss et al.<sup>22</sup> Cells were fixed in 2%PFA and 1X cytoskeleton buffer (1M NaCl, 0.1M PIPES, 30mM  $\text{MgCl}_2$ , 10mM EGTA, 10mM sucrose) for 15min then washed with DPBS+0.05%Tween. When non-activated, cells were incubated with SNAKA51 primary antibody for 30 mins prior to the following steps.

For Bivalent Scaffolds, respective scaffolds were added to cells at  $7.5\mu\text{M}$  in Bivalent Scaffold Staining Buffer and incubated for 30 mins. Cells were staining with Goat Anti-Mouse IgG H&L Alexa Fluor® 488 secondary antibody and DAPI prior to imaging. Cells were washed with Bivalent Scaffold Buffer and stored in Bivalent Scaffold Imaging Buffer for confocal imaging. Buffers used in experiment : (i) Bivalent Scaffold Staining Buffer (In PBS 1X :10mM  $\text{MgCl}_2$ , 0.05% Tween-20, 1%BSA, 1mM dextran sulfate, 0.2mg/mL sheared salmon sperm DNA) (ii) Bivalent Scaffold Buffer (10mM  $\text{MgCl}_2$ , 5mM TRIS, 1mM EDTA) (iii) Bivalent Scaffold Imaging Buffer (In PBS 1X : 0.5M NaCl, 10mM  $\text{MgCl}_2$ , Trolox 1X, PCA 1X, PCD 1X)

In preliminary assay, prior to addition of respective Bivalent Scaffolds, cells were blocked in BSA3% for 30 mins followed by Image-iT™ FX Signal Enhancer incubation for 15 minutes and DAPI. The Bivalent Scaffolds were incubated in Bivalent Scaffold buffer prior to imaging. Imaging conditions : LED intensity :10; Integration time : 600ms; Camera Gain : 10. LUT Applied, Cy5 : Red; DAPI : Blue.

### 3.2.12. Confocal Microscopy

Confocal microscopy images were acquired in 3 channels, DAPI, Cy5 and Alexa488. The images were acquired as z-stacks ( $0.2\mu\text{m}$ ) of 15 images. Images were post-processed in Fiji software as follows in all channels. To quantify scaffold selectivity, the integrated density on the cell was calculated, defined with a mask based on antibody SNAKA51 presence. The quantification of the Cy5 signals was done identically for all datasets (9 per cell type and scaffold condition) using MATLAB: (i) Segmentation of cells from background using hard thresholding and morphological operators on the SNAKA51 channel, (ii) segmentation of the nuclei using the same approach in the DAPI channel, (iii) summation of the Cy5 signal in the slices when present within the defined mask of (i) but not (ii), (iv) computation of average background intensity and hard thresholding (v) computation of the average intensity of the Cy5 signal. Resulting images were exported to Fiji

and identical LUT for Cy5 were applied. For statistical analysis (Supplementary S9) an ANOVA test between activated and resting conditions was applied as well as t-tests between each spatial scaffold in resting and activated state.

### 3.2.13. Multivalent Scaffold Binding Assay

HUVEC, CHO and HeLa cells were seeded in 96 well ibidi angiogenesis  $\mu$ -plate. Cells were serum-starved incubated overnight at 37°C, 5% CO<sub>2</sub>, 95% relative humidity. The following morning, cells were incubated in full media (supplemented with activator SNAKA51 primary antibody 1 $\mu$ g mL<sup>-1</sup> when stated) for 1h. All the following steps were performed at room temperature. Buffers used for fixation, staining and imaging were adapted from Strauss et al.<sup>22</sup> Cells were fixed in 2%PFA and 1X cytoskeleton buffer (1M NaCl, 0.1M PIPES, 30mM MgCl<sub>2</sub>, 10mM EGTa, 10mM sucrose) for 15min then washed with DPBS+0.05%Tween. When non-activated, cells were incubated with SNAKA51 primary antibody for 30 mins prior to the following steps.

As for Multivalent Scaffolds, the DNA NP were added to cells at 10nM in Multivalent Scaffold Staining Buffer and incubated for 1h. Cells were staining with Goat Anti-Mouse IgG H&L Alexa Fluor® 488 secondary antibody and DAPI prior to imaging. Cells were washed with Multivalent Scaffold Buffer and stored in Multivalent Scaffold Imaging Buffer for confocal imaging. Buffers used in experiment: (i) Multivalent Scaffold Staining Buffer (In PBS 1X :18mM MgCl<sub>2</sub>, 5mM NaCl, 0.05% Tween-20, 1%BSA, 1mM dextran sulfate, 0.2mg/mL sheared salmon sperm DNA) (ii) Multivalent Scaffold Buffer (18mM MgCl<sub>2</sub>, 5mM NaCl, 5mM TRIS, 1mM EDTA) (iii) Multivalent Scaffold Imaging Buffer (In PBS 1X : 0.5M NaCl, 18mM MgCl<sub>2</sub>, Trolox 1X, PCA 1X, PCD 1X)

For glycolyx digested conditions, after overnight serum starvation, cells were treated with a cocktail of Neuraminidase 0.1U mL<sup>-1</sup>, Heparinase I and III Blend 5U mL<sup>-1</sup>, and Hyaluronidase 50  $\mu$ g mL<sup>-1</sup> fir 1h at 37°C, 5% CO<sub>2</sub>, 95% relative humidity prior to SNAKA51 and/or full media activation. In preliminary assay, prior to addition of respective Multivalent Scaffolds, cells were blocked in BSA3% for 30 mins followed by Image-iT™ FX Signal Enhancer incubation for 15 minutes and DAPI. The Multivalent Scaffolds were incubated in Multivalent Scaffold buffer prior to plate reader imaging. Imaging conditions: LED intensity :10; Integration time : 4000ms; Camera Gain : 24. Multivalent Scaffold confocal images presented were identically hard thresholded (iv) LUT, Cy5 : Red; DAPI : Blue.

Stock solutions for the imaging buffers were prepared as follows<sup>22</sup> : (i) Trolox 100X (100mg Trolox, 430 $\mu$ L 100% methanol, 345 $\mu$ L 1M NaOH, 3.2mL MilliQ) (ii) PCA 40X (154mg PCA in total 10mL MilliQ after pH 9.0 adjustment with NaOH) (iii) PCD 100X (9.3mg PCD in 13.3mL PCD buffer) (iv) PCD buffer (100mM TRIS-HCl pH8, 50mM KCl, 1mM EDTA, 50% glycerol)

### 3.3 Monovalent RGD Binding Assay

#### 3.3.1 Monovalent RGD Synthesis and Binding Assay

Prior to investigating the targeting of integrin  $\alpha_5\beta_1$  receptors with bivalent, rigid DNA scaffolds, we investigated the monovalent binding of the RGD peptide synthesised in terms of its' binding concentration regime across HUVEC, CHO and HeLa. Establishing the monovalent binding concentration regime is pertinent in for analysis of further RGD-liganded Bivalent Scaffold binding assays. To weigh in on the impact of RGD ligand spatial presentation of Scaffold binding efficacy, a significant shift is required for the decoupling of the monovalent RGD binding contribution preventing masking of the signal observed.

The RGD and RAD peptides synthesised were characterised by ESI-MS and RP-HPLC, Figure 3.2, with purities of 91.55% and 90.74% respectively from peak integration of HPLC chromatograms. The peptides were coupled to a CF488-maleimide fluorescent dye via terminal cysteines for analysis of monovalent peptide binding. We found that the binding of the monovalent RGD tagged with CF488 was clearly detectable by confocal microscopy in milimolar concentration, Figure 3.3, regime, shown in Figure 3.3. Our analysis does not take into account any alteration in monovalent RGD-CF488 binding affinity caused by CF488, however we estimate this contribution to be negligible as we have incorporated a 3 glycine amino acid linker between the RGD binding sequence and CF488. Clear binding of the RGD-CF488 in the milimolar regime was however observed to be consistent with the RGD concentration used for binding to the isolated integrin  $\alpha_5\beta_1$  headpiece reported by Takagi et al<sup>23</sup> and the IC50 value of  $>100\mu\text{M}$  reported in a competition assay by Bernhagen et al.<sup>24</sup> Kapp et al. noted much lower GRGDS IC50 value of  $\sim 78\text{nM}$  for integrin  $\alpha_5\beta_1$ .<sup>25</sup> The deviation in affinity, posited by both studies could be attributed to integrin subtype affinity dependence on experimental protocols, namely when the receptor is free in solution versus immobilised on a substrate or cell surface.<sup>24,25</sup> To elaborate, the mobility of soluble integrin  $\alpha_5\beta_1$  impacts the binding kinetics for the GRGDS peptide in solution, probably overestimating the peptide affinity due to a slower off-rate compared to the immobilised integrin  $\alpha_5\beta_1$ . In our experimental setup, the reduced affinity observed compared to integrins in solution is likely due to the fixation of the integrin  $\alpha_5\beta_1$  on the cell surface, albeit in an extended conformation due to SNAKA51 activation.

The binding regime of the monovalent RGD was tested at 1mM on HUVEC, CHO and HeLa to check for any cell type specific variation prior to RGD-liganded Bivalent Scaffold binding assays, Figure 3.4. Controls of RAD-CF488 non-binding peptide and free CF488 dye, Figure 3.4, were added to HUVEC to account for aspecific binding. Clear bound signal was observed for monovalent RGD-CF488 bound to HUVEC, CHO and HeLa at 1mM. A shift in staining was observed from the free CF488 dye which aspecifically stained the nucleus compared to the RGD-CF488 where clusters were observed on the cells mirroring the distributions of the integrin  $\alpha_5\beta_1$  characterised in Chapter 2. A noticeable absence of signal was observed for the RAD-CF488 non-binder on HUVEC at 1mM.

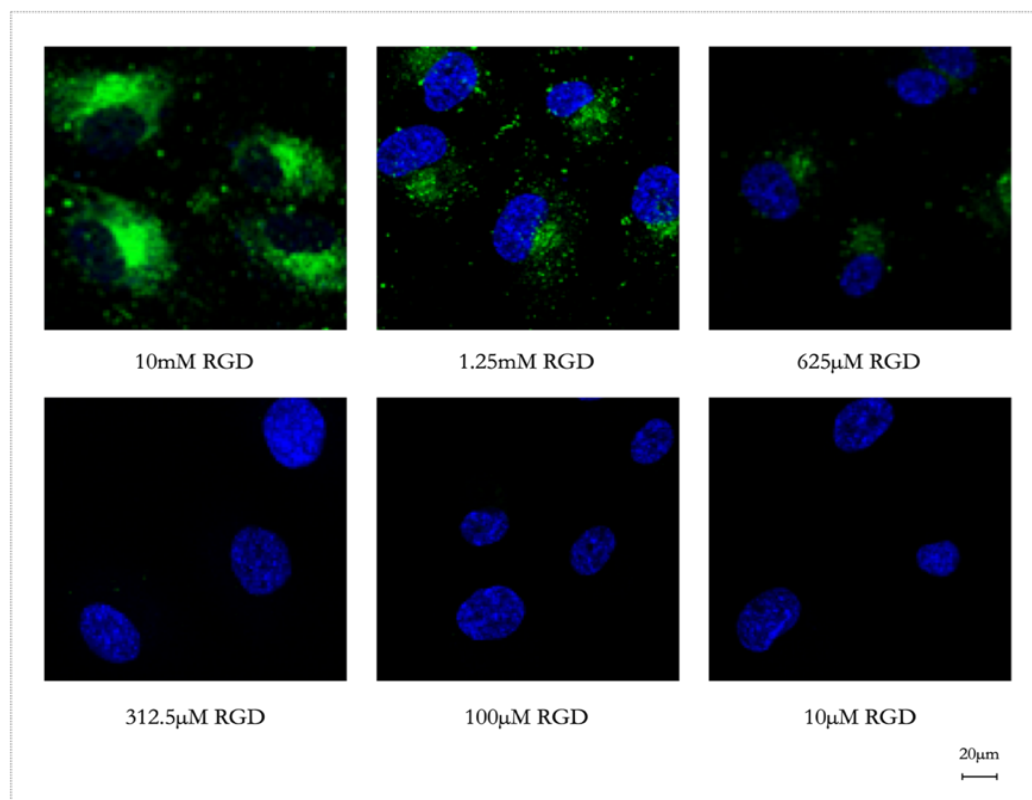
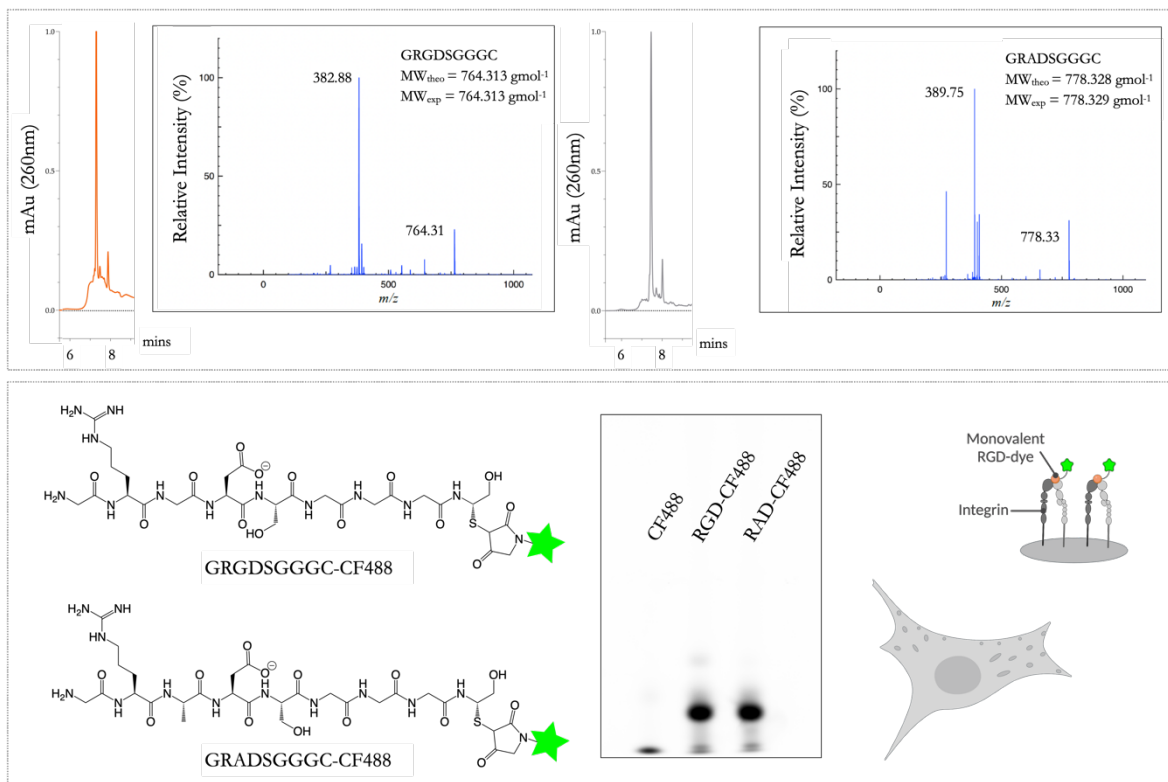


Figure 3.3 Monovalent RGD-CF488 binding concentration regime in HUVEC.

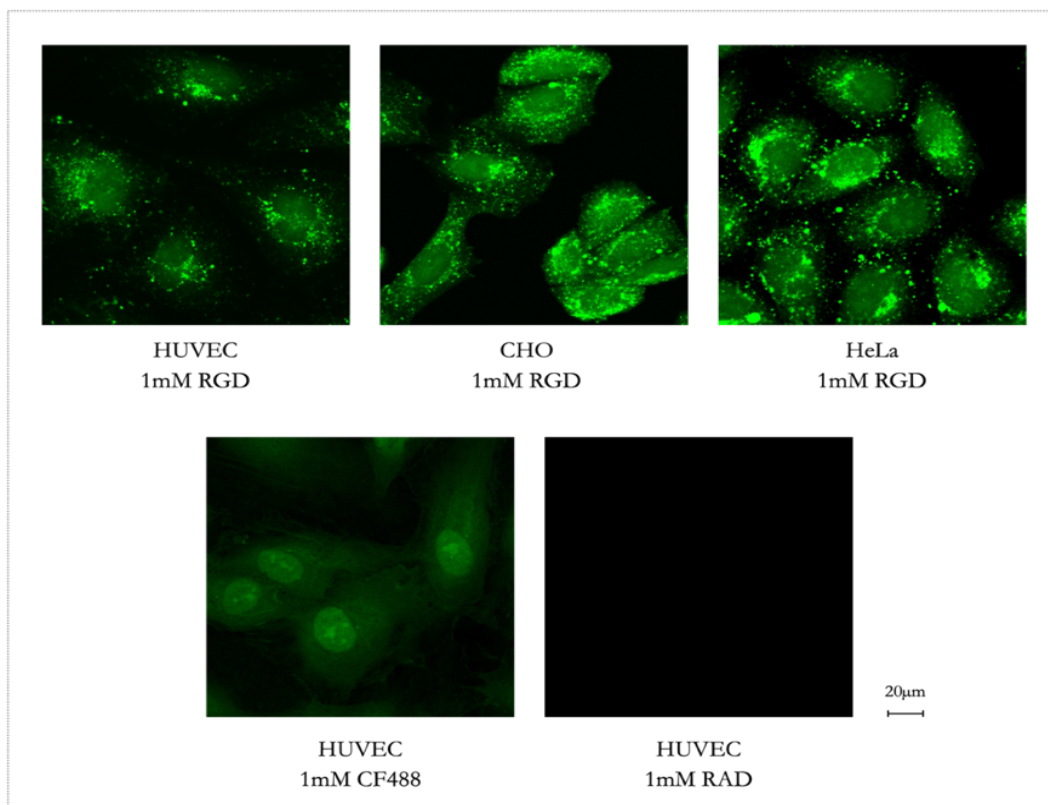


Figure 3.4 1mM monovalent RGD-CF488 binding to HUVEC, CHO and HeLa. Controls for RGD binding with 1mM RAD peptide and 1mM CF488 dye.

## 3.4 Bivalent Scaffold

### 3.4.1. Bivalent RGD Scaffold Preparation

The bivalent scaffolds used in our study were adapted from a previous publication<sup>19</sup>, as detailed in Figure 3.5. The Bivalent Scaffold arm-to-arm spacings were designed and calculated based on dsDNA having an axial rise of 0.34nm per base-pair<sup>26</sup> and were subjected to *in silico* simulations and analysis. Bivalent scaffolds were categorised as rigid as double stranded DNA (dsDNA) is estimated to have persistence lengths of  $\sim 150$  base pairs or  $\sim 50$ nm, of which we are well below.<sup>27</sup> The ligand spacings attributed to the respective Bivalent Scaffolds were calculated and rounded up to the nearest nanometer calculated for a maximum arm-to-arm distance conformation of  $180^\circ$  between scaffold arms. The Bivalent-7 scaffold took into account the reported diameter of the integrin headpiece (5-10nm)<sup>23,28,29</sup> and RGD ligand binding pocket between the  $\alpha$  and  $\beta$  integrin subunits in ligand primed conformations.<sup>23</sup> Given the spatial constraints, Bivalent-7-RGD binding would occur bridging neighbouring integrins clustering in contact with each other. An additional flexible bivalent scaffold, Bivalent-Flex (data not shown) was added as a control for the rigidity of ligand presentation. The third arm of all Bivalent Scaffolds was kept constant across Bivalent

Scaffolds, situated in the plane orthogonal to the ligand binding arms and is annealed to an antihandle conjugated to a dye to probe scaffold localisation.

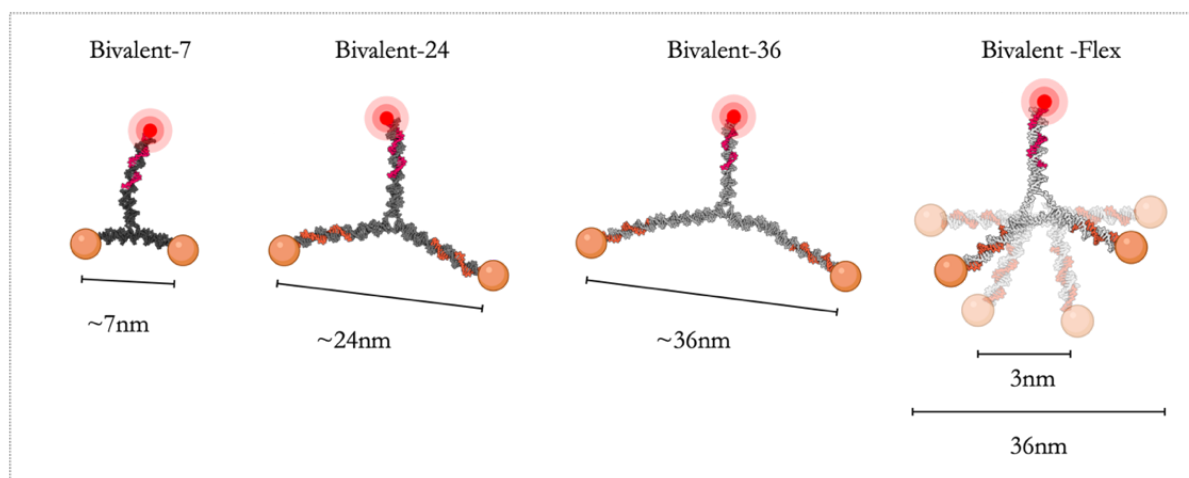


Figure 3.5 Bivalent scaffolds for binding assays. Calculated maximum arm to arm spacing Bivalent-7 (7nm), Bivalent-24 (24nm), Bivalent-36 (36nm). Bivalent-Flex arm to arm spacing calculated to range from 3-36nm.

For the longer scaffolds, Figure 3.5, i.e. Bivalent-24, Bivalent-36 and Bivalent-Flex, the core stands presenting handles (in gray) were first annealed with 1.2X excess of a fluorophore-conjugated strand (in pink) to ensure complete annealing of the fluorescent dyes to the Bivalent Scaffolds. Antihandle strands (in orange) that were peptide ligand conjugated prior are then annealed in a second step. For the Bivalent-7, the core strands (in dark gray) were directly conjugated to the peptide ligands and annealed with a 1.2X excess of the fluorophore-conjugated strand (in pink) in a one-pot reaction.

It is of note that in the case where inter-receptor spacings matches RGD liganded Bivalent Scaffold presentation, more binding sites would be available for the shorter bivalent scaffolds, i.e. Bivalent-7 than the longer scaffolds Bivalent-24 and Bivalent-36. The Bivalent-Flex Scaffold was included as a control for rigidity in ligand spatial presentation in the scaffolds. The Bivalent-Flex Scaffold flexibility stems from a hinge region with three unpaired thymine (T) base pairs at its' core, allowing for flexibility in probing the ensemble of spacings adopted by the Bivalent-36, Bivalent-24 and Bivalent-7 rigid scaffolds, down to 3nm according to calculations. Given the spatial range in ligand presentation of the Bivalent Flex, a distribution of inter-receptor spacings on the cell surface would provide a greater abundance in potential binding sites. Nevertheless, it is hypothesised that the Bivalent-Flex Scaffold whilst being able to probe a larger ensemble of spacings would incur a higher entropic penalty when binding receptors<sup>30-32</sup>, thus being a control for a potential increase in binding efficacy when Bivalent, Rigid ligand presentation is matched to receptor spacing.<sup>32</sup>

AFM imaging was conducted on the longer Bivalent Scaffolds (Bivalent-24, Bivalent-36 and Bivalent-Flex) to confirm tri-armed structure conformations,. The Bivalent-7 scaffold was not imaged due to limiting resolution in probing the shorter arm-to-arm distance of 7nm but should adopt tri-armed conformations as the scaffold core sequences were conserved. Distances of the

arm-to-arm spacing of the bivalent scaffolds were not extracted from AFM due to a non-negligible influence of the surface treatment for imaging on scaffold conformation on the surface and potential deviations of Bivalent Scaffold surface immobilised conformations to conformations adopted in solution.<sup>33</sup>

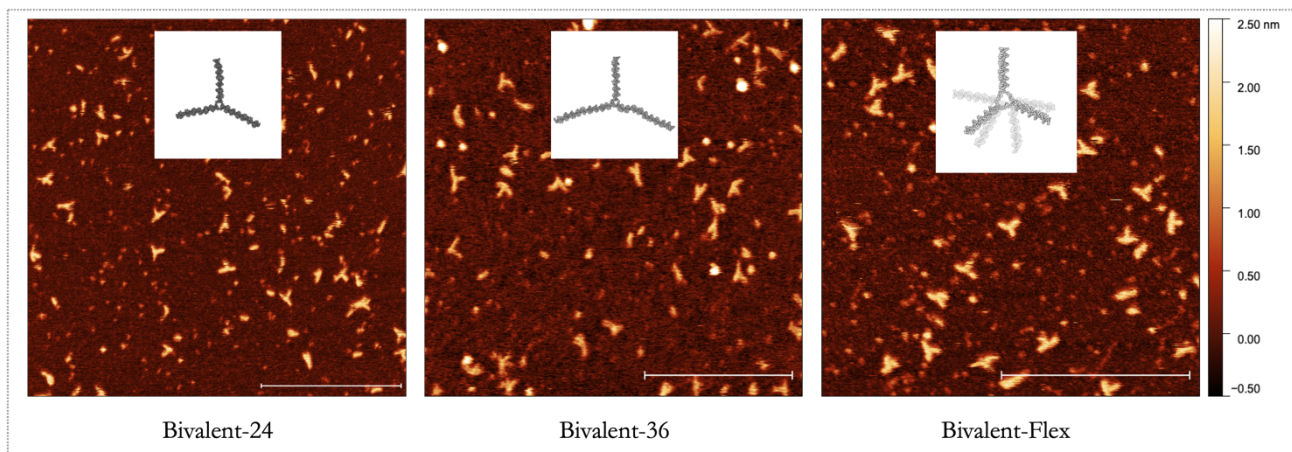


Figure 3.6 AFM images of Bivalent-24, Bivalent-36 and Bivalent-Flex. Scale bar: 200nm.

The longer bivalent scaffolds, Figure 3.6 i.e. Bivalent-24, Bivalent-36 and Bivalent-Flex were designed to present handles of the same sequence for peptide liganded ssDNA annealing. Bivalent-7 were functionalised for peptide ligand conjugation directly on the scaffold core to attain an arm-to-arm spacing of  $\sim 7$ nm. In both cases, a heterobifunctional cross-linker, DBCO-maleimide was employed to conjugate the cysteine bearing peptides to the azide-functionalised ssDNA strands, detailed in Figure 3.7 (A) The peptide conjugated ssDNA functionalisation was characterised by RP-HPLC Figure 3.7 (B) and Native PAGE, Figure 3.7 (C).

Each Bivalent Scaffold was characterised for bivalent ligand presentation added in 1.2X excess per handle by Native PAGE, Figure 3.8. For longer scaffolds, the relative migration of the Bivalent Scaffold cores was compared to the ligand-free antihandle Bivalent Scaffolds and the liganded antihandle Bivalent Scaffolds. Incomplete functionalisation of the Bivalent Scaffolds were incubated with additional excess ligand conjugated antihandles. The migration of one clear band relative to controls for the respective Bivalent Scaffolds were deemed fully functionalised scaffolds. For the Bivalent-7, the relative migration of bands corresponding to stepwise addition of strands composing the Scaffold was used to determine Scaffold formation.



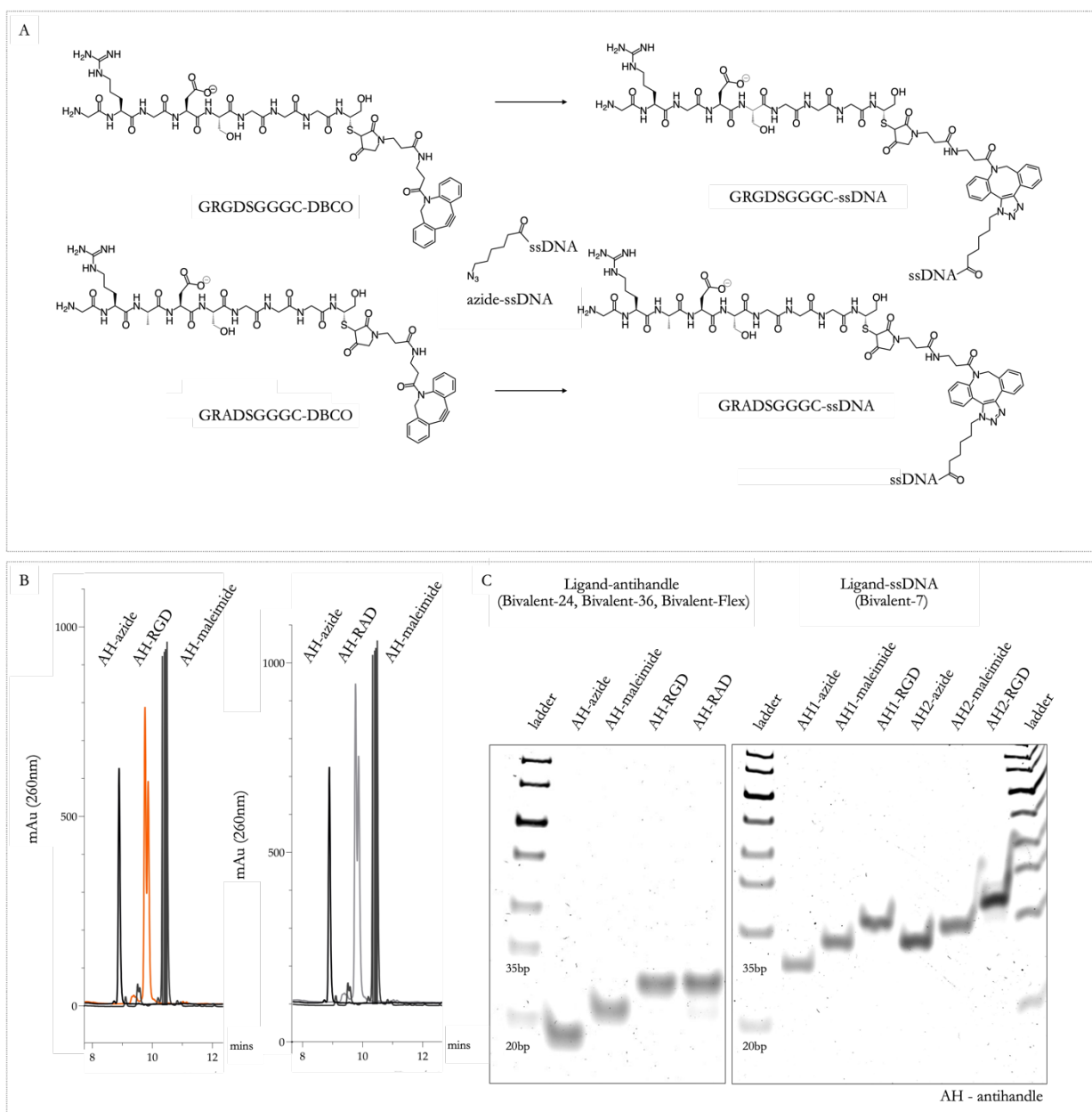


Figure 3.7 Material characterisation. ssDNA antihandle conjugation to peptide via DBCO-maleimide crosslinker using strain promoted alkyne-azide click chemistry and thiol-maleimide reaction. HPLC characterisation of peptide-ssDNA conjugates. 20% Native PAGE characterisation of peptide ssDNA

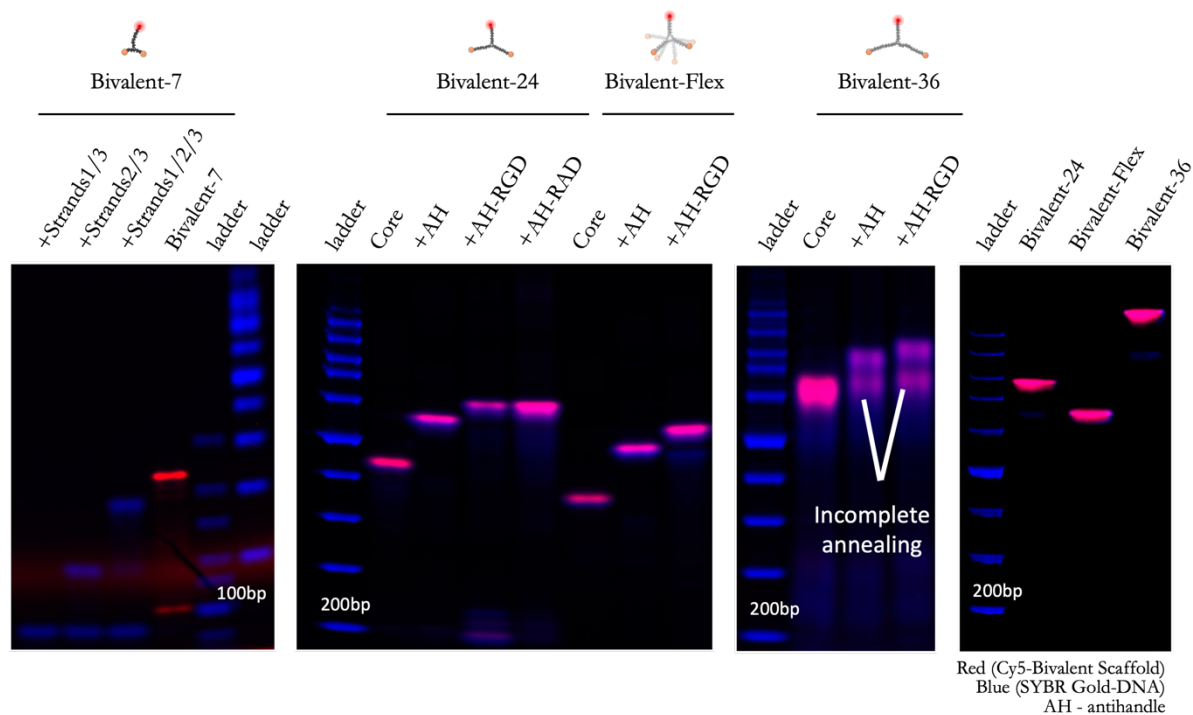


Figure 3.8 PAGE characterisation of Bivalent liganded Scaffolds. The presence of a single band with expected relative migration to smaller structures is indicative of complete scaffold functionalisation.

### 3.4.2. Bivalent RGD Binding Assay

Preliminary analysis was first conducted to determine the RGD-liganded Bivalent Scaffold binding concentration regime using the Bivalent-24-RGD on HUVEC, Figure 3.9 (top) then compared to CHO and HeLa, Figure 3.9 (bottom) It is of note that the monovalent RGD-CF488 binding was not observed in this concentration regime via confocal microscopy.

After establishing the regime of concentration with clear staining of Bivalent-RGD liganded Scaffolds, a concentration of  $15\mu\text{M}$  RGD ( $7.5\mu\text{M}$  Bivalent Scaffold) was employed in the assay investigating the influence of ligand spatial presentation on different Bivalent Scaffold binding to HUVEC, CHO and HeLa. The buffer conditions were adapted based on a publication from Strauss et al.<sup>22</sup> in the RGD liganded Bivalent Scaffold binding assay to prevent aspecific nuclear localisation of the Cy5 bearing Bivalent Scaffolds observed.

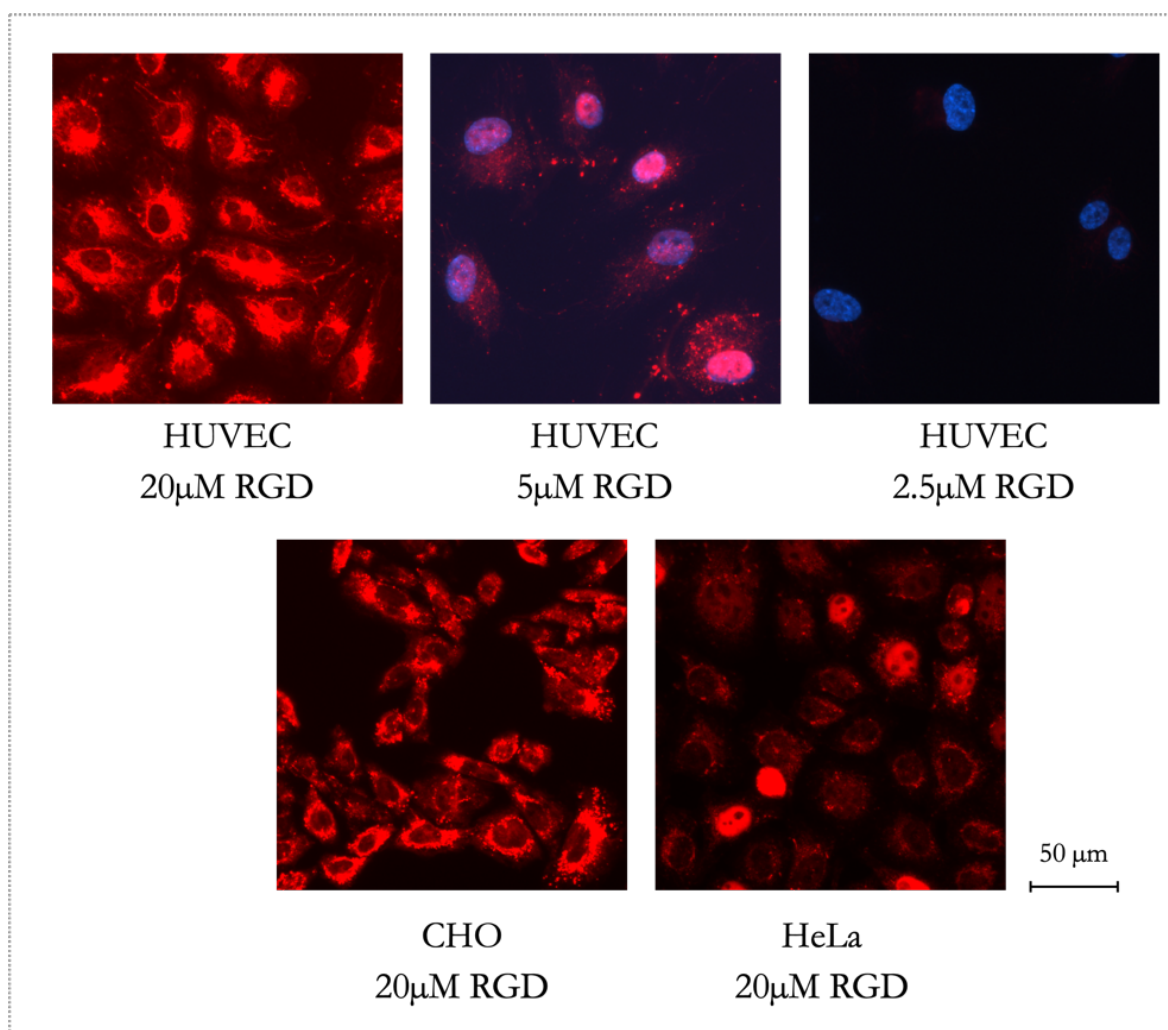


Figure 3.9 Bivalent-24-RGD binding on HUVEC in the micromolar regime. Bivalent-24-RGD binding on CHO and HeLa.

Confocal microscopy images were obtained for the respective RGD liganded bivalent scaffolds on HUVEC, CHO and HeLa, Figure 3.10 (A) in resting conditions and (B) SNAKA51 activated as described in 3.2.12. In our analysis in Figure 3.10 (C) we take into account the integrin  $\alpha_5\beta_1$  receptor, neglecting other RGD-binding integrins as our activation method is specific to the integrin  $\alpha_5\beta_1$  and integrins being constitutively inactive<sup>34-36</sup> or ligand-bound in resting conditions.<sup>35,37</sup>

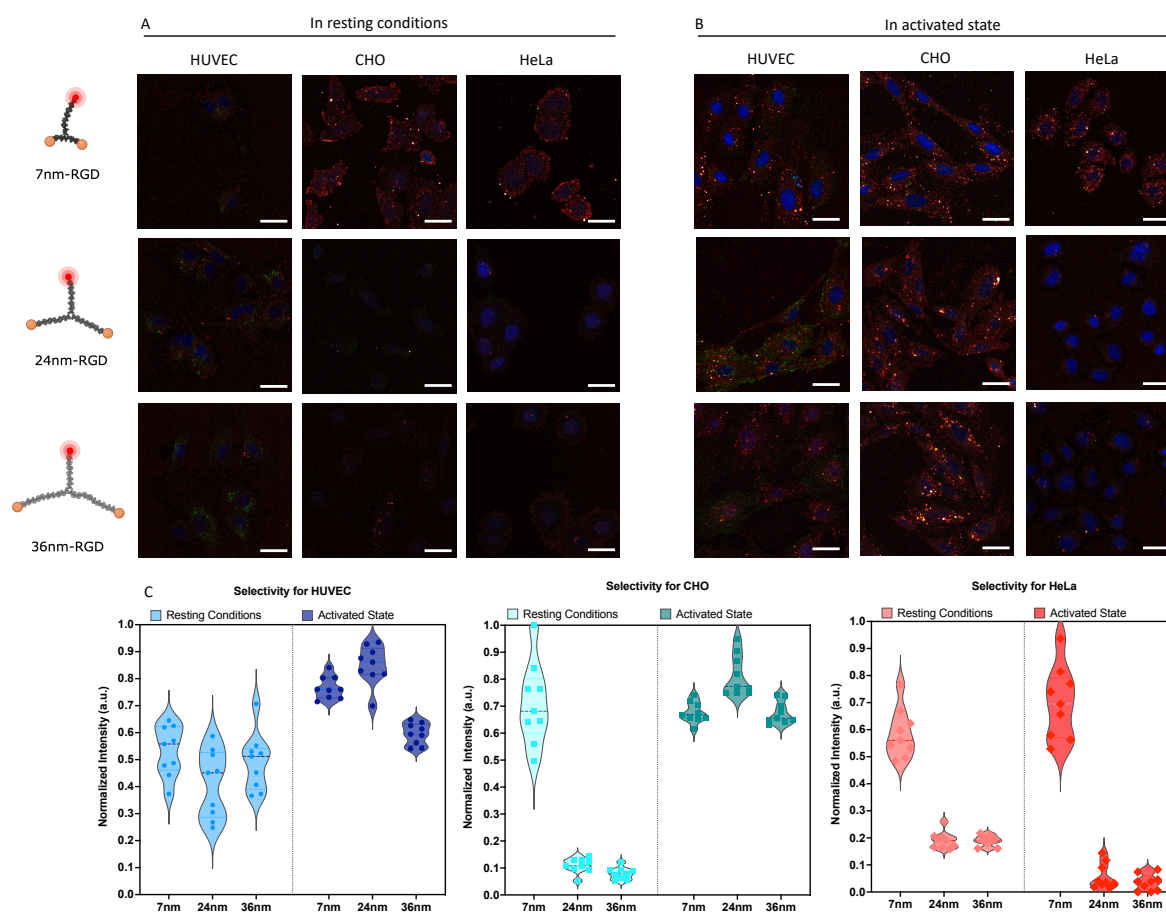


Figure 3.10 Confocal microscopy analysis of spatially constrained integrin staining. (A) Representative overview for non-activated cells (B) Representative overview for activated cells. Images show the DNA-analytes in red (Cy5 label), antibody-stained integrin in green (Alexa 488) and the nucleus in blue (DAPI). Scale bar = 30  $\mu\text{m}$  (C) Quantification of selective binding, in resting conditions and in activated state. Plotted is the globally normalized intensity of scaffold present within the cell boundaries from a Z-projection of confocal images, corrected for background. Data is quantified from nine independent image stacks containing multiple cells per image.

From the confocal microscopy images coupled with RGD liganded scaffold efficiency in binding in Figure 3.10 we observe that all three cell lines show distinct trends in RGD-liganded Bivalent Scaffold binding efficacies depending on activation state. Whilst a notable increase in RGD-liganded Bivalent Scaffold binding efficacies was observed when HUVECs were activated, such a distinction between activation states was not noticeable on CHO and HeLa. Increased binding efficacy of the Bivalent-7 Scaffolds were observed in CHO and HeLa in resting conditions. Whilst HeLa in an activated state showed a higher binding efficacy for the Bivalent-7, all rigid scaffolds bound to HUVEC and CHO with varying efficacies.

It should be noted that cells adopting integrin  $\alpha_5\beta_1$  in extended conformation in resting conditions, i.e. with SNAKA51 staining are predominantly ligand bound.<sup>34</sup> Also, whilst SNAKA51 activation primes the integrin  $\alpha_5\beta_1$  for activation, the subsequent endocytosis of integrin  $\alpha_5\beta_1$  previously ligand bound could offset the abundance of integrins in extended/active conformations on the cell surface.<sup>38</sup> The observed signal of RGD-liganded Bivalent Scaffolds binding to cells in resting conditions, likely occur at sites of unliganded integrin  $\alpha_5\beta_1$  co-clustering with ligand-bound integrins, previously observed by Changede et al.<sup>39</sup> as integrins reportedly adopt inactive

conformations and are diffuse<sup>34-36</sup> or are ligand bound in active conformations on the cell surface.<sup>35,37</sup> The possibility of the RGD-liganded Bivalent Scaffolds binding to other RGD integrins in ligand primed conformations cannot be ruled out either.

The Bivalent-7-RGD binding to CHO cells in resting conditions, whilst not showing a difference in binding efficacy compared to the other Bivalent Scaffolds stained predominantly the cell and nuclear periphery, regions where the integrin  $\alpha_5\beta_1$  reside in nascent and fibrillar adhesions, respectively.<sup>40,41</sup> Whilst the signal was not as marked on the cell periphery, small clusters were observed on the entirety of the HeLa cell surface with larger clusters in the nuclear periphery. The lack of difference between HeLa when activated versus in resting conditions of integrin  $\alpha_5\beta_1$  extended conformations could be attributed to the upregulation of integrin  $\alpha_5\beta_1$  in certain solid tumours, including cervical cancer<sup>42</sup> forming unliganded clusters. These clusters of unliganded integrins are reportedly modulated by cancer-specific intracellular-binding factors promoting cancer progression through the sensing of ECM composition.<sup>43</sup> As such, clusters of Bivalent-7-RGD, bound on the entirety of the HeLa surface in resting conditions observed likely bind to these unliganded integrins. The overall RGD-liganded bivalent scaffold efficacy shows a drastic improvement when HUVECs are activated compared to in resting conditions, explained by the SNAKA51 activation driven clustering of unliganded integrin  $\alpha_5\beta_1$  receptors into dense fibrillar adhesions.<sup>44</sup>

Altogether, the trends in binding efficacy observed across Bivalent Scaffolds in function of integrin  $\alpha_5\beta_1$  receptor in extended conformation expression presented in can be explained as a trade-off in terms of (i) a match of inter-receptor spacing to ligand presentation, (ii) number and density of integrins within a cluster<sup>45-47</sup> (iii) local cluster topography due to thickness of glycocalyx<sup>48-51</sup> (iv) potential binding sites per surface area probed<sup>15</sup> (v) entropic penalty vs enthalpic gain in scaffold binding through relatively rigid or flexible ligand presentation.<sup>32,52</sup> In these experiments, the effect of integrin turnover and adhesion dynamics<sup>53</sup> do not factor into the trends in binding efficacy observed but likely interplay on live cells. As a result, deviations from the trends observed could be expected on live cells where the receptors are not fixed,<sup>54</sup> engaging the role of the glycocalyx<sup>55</sup> and when probing cells in 3D.<sup>56</sup> To elaborate on the complexity in the interpretation of the binding trends observed in terms of trade-off between glycocalyx thickness and enthalpy-entropy compensation, a thicker glycocalyx increases integrin-mediated cell adhesion by trapping them in an activated state once extended from the cell surface.<sup>57,58</sup> On the other hand, a thick glycocalyx does not sterically hinder integrin-ECM binding. From the perspective of an integrin liganded-scaffold however, a thick glycocalyx would sterically hinder binding site accessibility, but stabilise binding events once occurred.<sup>59</sup> As endothelial cells have a thicker glycocalyx<sup>60</sup> and cancer cells frequently overexpress components of the glycocalyx<sup>59</sup> the trends observed on activated HUVEC and HeLa cells with Bivalent-24-RGD and Bivalent-36-RGD could be explained as a negative enthalpic-entropic compensation.<sup>61</sup> The Bivalent-7-RGD which has an additional lower entropic penalty upon binding due to its' lower multiplicity of conformations, lower loss of translational and rotational entropy related to molecular weight<sup>52</sup> and higher "effective molarity"<sup>30</sup>, might further contribute to its' gain in enthalpic-entropic compensation if "trapped" by the cells' glycocalyx, i.e. imposing restrictions on the RGD-scaffolds aforementioned degrees of freedom.

## 3.5 Multivalent, Rigid Scaffold

### 3.5.1. Multivalent Rigid Scaffold Preparation

Building upon the results obtained from RGD-liganded Bivalent Scaffolds, we attempted to enhance the selectivity with multivalent ligand presentation with a Multivalent Rigid Scaffold previously designed in our laboratory.<sup>21</sup> Here, the RGD ligands could be patterned on the 60nm Scaffold with various geometries and spacings for integrin  $\alpha_5\beta_1$  targeting.

Multivalent, Rigid Scaffolds were prepared as detailed in a recent publication,<sup>21</sup> depicted in Figure 3.11 with the Ligand Face bearing 36 potential sites for ligand presentation via handle-antihandle hybridisation and a Fluorescent Probe Face with six integrated Cy5 dyes as probes for signal localisation. An excess of liganded antihandle of 1.6X per functional site was used upon agarose gel characterisation of increasing excess in Alexa488 conjugated antihandles on the Multivalent Scaffold. The antihandles were conjugated to ligands with chemistry detailed in 3.2.6. Preliminary assays were conducted with Multivalent Scaffolds with 36 handles spaced at 7nm for ligand presentation (Multi-36-7).

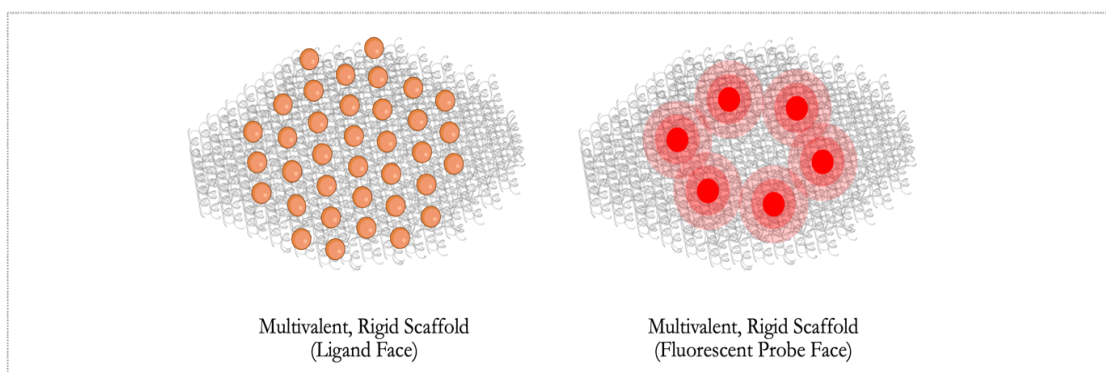


Figure 3.11 Multivalent, Rigid, Scaffold. Ligand presentation and fluorescent dye immobilisation on opposing faces of the scaffold for cell binding assays.

### 3.5.2. Multivalent, Rigid Scaffold RGD Binding Assay

HUVEC binding assays conducted with the Multivalent, Rigid Scaffold characterised in Figure 3.12 yielded results that had high levels of aspecific binding and/or trends that were irreproducible, the best conditions shown in Figure 3.13. PEG-oligolysine coatings were employed to shield the Scaffold resulted in either an elimination of staining or an increase in aspecific staining. Digestion of the endothelial cell glycocalyx previously shown to improve Scaffold staining<sup>49,62</sup> was conducted

on live or fixed cell staining with Multivalent Scaffolds of different ligand valencies and Scaffold concentrations (up to 10nM) did not result in reproducible trends across the biological repeats.

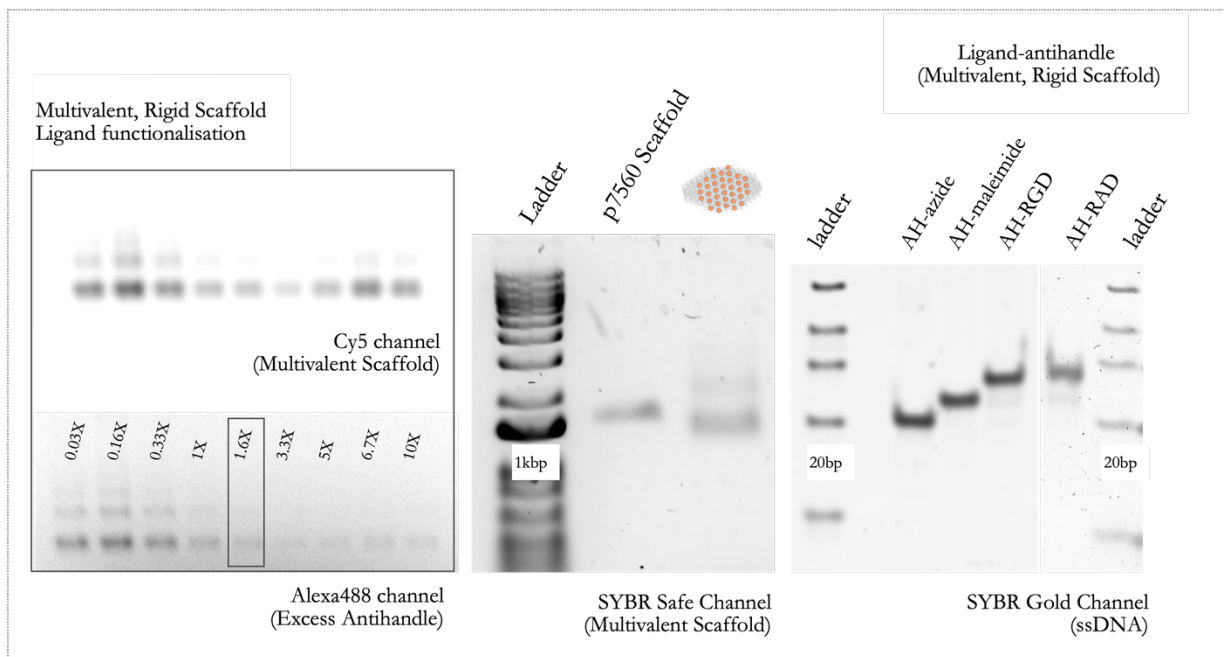


Figure 3.12 Multivalent Scaffold characterisation. (left) Characterisation of excess ligand-antihandles for scaffold functionalisation. (middle) Multivalent Scaffold characterisation (top) Ligand-antihandle Native PAGE characterisation.

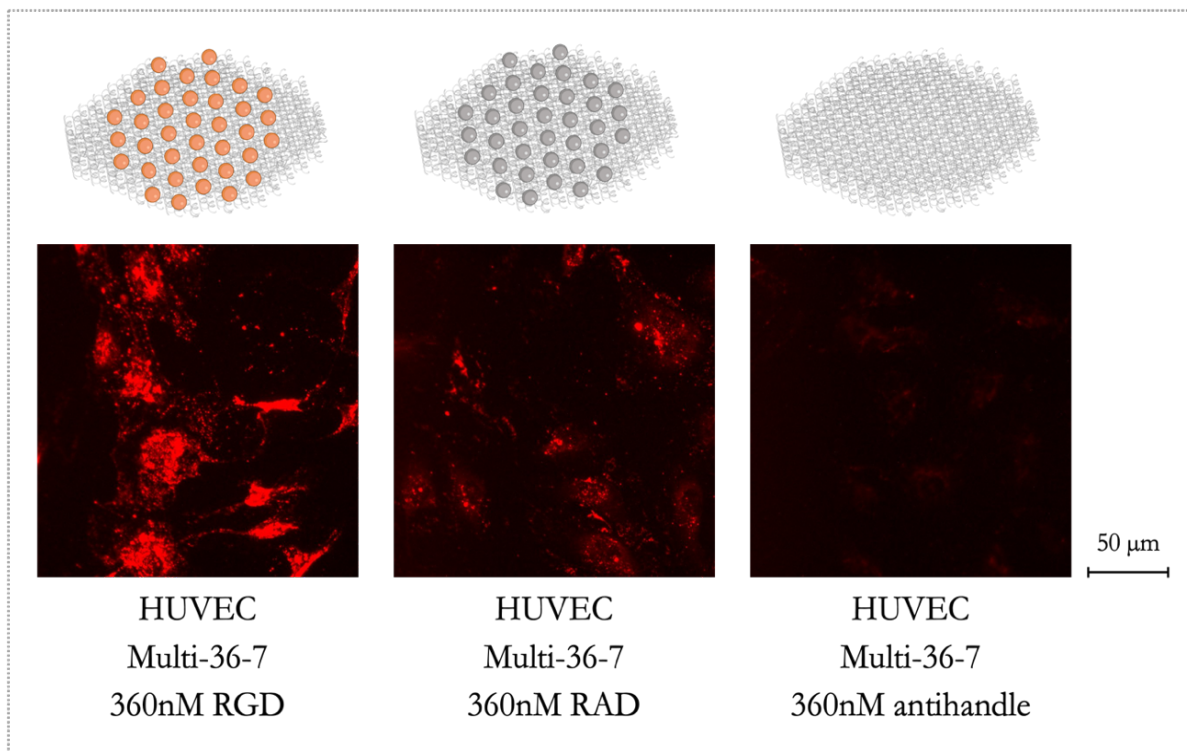


Figure 3.13 HUVEC staining with Multivalent Scaffolds. Cell binding assay with 10nM Multi-36-7 Scaffold, 360nM ligand concentration.

### 3.6 Conclusions

Concluding, our work presents the cell selective  $\alpha_5\beta_1$  integrin targeting using bivalent, spatially controlled scaffolds designed by spatial input from a low-technology, easy-to-implement method to obtain quantitative information on global receptor spacing on the cell surface. We demonstrated the workflow using the  $\alpha_5\beta_1$  integrin, a critical regulator of cell-adhesion but equally important in many diseases. Indeed, a significant cell-type dependent spacing-signature profile was obtained, with clear differences when cells were activated. Translating the spatial information of receptor distribution into DNA-scaffolded multivalent particles, we demonstrated selective interaction within HUVEC and CHO cells, and between their activated and resting state. As the methodology homogenizes the receptor spacing within a pixel, deviations from reality in the special scenario when receptors form nanoclusters, can be expected. This was indeed observed when analyzing HeLa cells. Taken together, the accessibility of the presented approach, combined with the demonstration of differential targeting based on divalent ligand spacing, presents a broadly applicable strategy when selective cell targeting is envisioned.

The trend in binding efficacies observed is also in good agreement with recent findings from Bae et al., where RGD ligands spaced bridging two integrins (S-7nm), three integrins (L-20nm), and two and a half integrins (M-17nm) respectively tapered in efficiency of  $\beta_1$  integrin labelling and stem cell differentiation.<sup>63</sup> The behaviour exhibited by the Rigid Bivalent Scaffolds between clusters on the cell surface versus the diffuse pool of receptors residing outside clusters is akin to the regime of “super-selectivity” proposed by Martinez-Veracoechea et al.<sup>45</sup>

Follow up investigations with RGD-liganded Multivalent Scaffolds encountered difficulties in staining reproducibility and/or high background staining. Conditions investigated to mediate the problem ranged from oligolysine-PEG coatings,<sup>64</sup> glycocalyx digestion,<sup>48,49,60</sup> live and fixed cell staining,<sup>65,66</sup> ligand valencies,<sup>67,68</sup> scaffold concentrations, and cell type (HUVEC, CHO, HeLa). We concluded that the absence of reproducible staining stemmed from one or a combination of factors : (i) functional concentration regime of the Scaffold (here in the low nanomolar regime), also where aspecific interactions could mask specific staining; (ii) mismatch in ligand/antihandle receptor presentation,<sup>69,70</sup> where local topographies either in ligand or receptor presentation could prevent higher valency ligand-receptor interactions; (iii) co-clustering of integrin  $\alpha_5\beta_1$  with integrin receptors in lower affinity conformation (not primed for ligand binding), integrins with lower affinities or do not bind the RGD sequence that are in the vicinity<sup>71-73</sup> and/or other transmembrane receptors.<sup>74,75</sup> Wang et al. were however able induce nanoscale receptor clustering with peptide ligands on sheet like DNA Origami,<sup>76</sup> albeit with structure with a higher degree of flexibility than the Multivalent Scaffold here employed.



### 3.7 Appendix

#### 3.7.1 ssDNA Bivalent Scaffold strands and modifications

Sequence Name	Sequence	Modification
XST-1	GTTGCTAGTGGTGTCCAAAC	5' azide
XST-2	GTTTGGACACTCAGCCTAACGCTAG	5' azide
XST-3	CCATAGACTAGCAACTTTCACCCTAGCGTTAGGCTGACACTAGCAAC	
LT-1	TTCCTCTACCACCTACATCACCTAGCGTTGCTAGTGGTGTCAAACGCTAG	
LT-2	TTCCTCTACCACCTACATCACCTAGCGTTTGGACACTCAGCCTAACGCTAG	
LT-3	CCATAGACTAGCAACTTTCACCCTAGCGTTAGGCTGACACTAGCAACGCTAG	
XLT-1	TTCCTCTACCACCTACATCACGCGTTGCTAGTGTGTCAGCCTAGCGTTGCTAGTGGTGTCCAAACGCTAGAATACTGCAGTACGATC	
XLT-2	TTCCTCTACCACCTACATCACGATCGTACTGCAGTATTCTAGCGTTTGGACACTCAGCCTAACGCTAG	
XLT-3	CCATAGACTAGCAACTTTCACCCTAGCGTTAGGCTGACACTAGCAACGCTAGGCTGACACTAGCAACGC	
FT-1	TTCCTCTACCACCTACATCACCGCGCTAGCGTTTTGGGTCCACGC	
FT-2	TTCCTCTACCACCTACATCACGCGTGGACCCTTTTGCAGCC TGGC	
FT-3	CCATAGACTAGCAACTTTCACCGCCAGGCTGCTTTTCGCTAGCGCG	
Ligand antihandle	GTGATGTAGGTGGTAGAGGAA	3'azide
Dye antihandle	GGTGAAAGTTGCTAGTCTATGG	3' Cy5

#### 3.7.2 ssDNA Multivalent Scaffold strands and modifications

The scaffold and staple sequences are identical to that reported in a recent publication,<sup>21</sup> with the exception of substitutions for ligand presentation and Cy5 probe integration detailed as follows.

#### 3.7.3 Ligand Face strands (Top)

Sequence Name	Sequence
42[160]68[149]	TTATTACATACCACGGAACGCTAAACGTTTCCTCTACCACCTACATCAC

46[76]72[65]	TAAGCCCTAGACGGAATACATGTTTGAGTTCCTCTACCACCTACATCAC
52[186]78[171]	AAATGTCGTCTTAAATTGTAATTCGTGGAGGATTCCTCTACCACCTACATCAC
50[160]76[149]	ATACCGATAAAATACTGCCATAAATAACTTCCTCTACCACCTACATCAC
60[99]86[87]	TACTGGTAAAGTTCAGATTTAGAAAAGGAATTCCTCTACCACCTACATCAC
54[160]80[149]	CAGTACACCTCATAACTCACACGGAAGCTTCCTCTACCACCTACATCAC
44[97]70[87]	AAGGCTTATTGGGCTAGATGGATGGCAATTCCTCTACCACCTACATCAC
50[118]76[108]	GCATAACAGGACTAGCCTTGATCCTTAGTTCCTCTACCACCTACATCAC
51[88]78[87]	ATTACCATAGGGAAAAACATTTCTTTTCCTCTACCACCTACATCAC
56[97]82[87]	AGGCAGGACCAGAAAGAGCGGTTCGGCCATTCCTCTACCACCTACATCAC
33[130]62[129]	CATGCTGAATGGCTTAAATTGAGTTACGCAAGACATTATTTTCCTCTACCACCTACATCAC
45[109]72[108]	AGGGTAATGATTAGGAGCTCCAGCTTCCTCTACCACCTACATCAC
38[118]64[108]	AATGACCGGAAGCCGTCAAATAGAGTCATTCCTCTACCACCTACATCAC
54[118]80[107]	AATCACCCGGTCATGGGAAACATCGGCCITTCCTCTACCACCTACATCAC
52[55]78[44]	AGCACCGCATTGGGGTCTGAAACACGACTTCCTCTACCACCTACATCAC
48[97]74[87]	ATAAGTTCGCAATAGGTGAGGAGTTGGCTTCCTCTACCACCTACATCAC
52[139]78[128]	TTTGCTAACGTTGATATCCGCACAGGGCTTCCTCTACCACCTACATCAC
44[181]70[171]	GCTGACCAGGACGTTTAAATGTTTCCTGTTTCCTCTACCACCTACATCAC
60[144]86[127]	AAACCCCTGCCGTATTAAGGAACAAATAGGGTTTCCTCTACCACCTACATCAC
36[97]62[87]	AGGCATTATTCCTAACCTCCGAATAAAGTTCCTCTACCACCTACATCAC
38[160]64[150]	ATTGAATTCAAAGCTGTGTAGTATTTTATTTCCTCTACCACCTACATCAC
44[55]70[44]	GATTTTACAAAATTTTGAGTCAGAAGGTTTCCTCTACCACCTACATCAC
54[76]80[65]	AGCCGCCTGCCTTTCACCGAATTAGTATTCCTCTACCACCTACATCAC
48[139]74[128]	TAAAGGTACTCCTTGTGGTTGTGCAAGGTTTCCTCTACCACCTACATCAC
46[160]72[149]	TTGTGTCCCAACTTCTATTACGGCAAAGTTCCTCTACCACCTACATCAC
58[118]84[107]	GCTCAGTTATAAGTTCGGTTCACCCAGCATTCCTCTACCACCTACATCAC
48[55]74[44]	TACCAGCAGCAGATCTGAGAGTTGCTGATTTCCTCTACCACCTACATCAC
42[76]68[65]	TGCACCCTACCGCGAGATGAAAAAATCGTTTCCTCTACCACCTACATCAC
37[55]64[65]	AAAACAAAAGGTAAAGTAATGTCTTCTGTATCCTTGTTCCTCTACCACCTACATCAC
44[139]70[129]	CATTACCATTACCTACAAACGTCTGAAATTCCTCTACCACCTACATCAC
40[139]66[129]	GATAAAATTTTGCCAACAAGATCTAGCTTTCCTCTACCACCTACATCAC
56[139]82[128]	TCAGAACGGGATAGAGAGTTGAGGGTGGTTTCCTCTACCACCTACATCAC
40[97]66[87]	TAGAAACGTCCTGAAATCATACTTTTTTTTCCTCTACCACCTACATCAC
50[76]76[65]	AAGGCCGGACAGCAGACCTGAAAACATCTTCCTCTACCACCTACATCAC
42[118]68[107]	GCGGGAGCCGGTATAACAGAAGCCCAATTCCTCTACCACCTACATCAC
48[181]74[171]	AGAATACATACCAAGCCAAGCACGACGTTTCCTCTACCACCTACATCAC

## 3.7.4 Fluorescent Probe Face strands (Bottom)

Sequence Name	Sequence	Modification
17[77]71[87]	GGGACGAGTAACCGAGAACGAGCTATTT	3' Cy5
11[140]77[150]	TTAAGCTCAACTCGTTCCATTACATACA	3' Cy5
11[98]77[109]	CCGAACTGACGCATCTACAGACCACGGA	3' Cy5
5[119]83[130]	GGCGAAACGGTCCACACCCTCTAATCAA	3' Cy5
17[161]71[171]	CGCCATTGTAACAATCATTTATAACAACA	3' Cy5
17[119]71[130]	CAGCTTTGACCGTATTTAATCCCGACTT	3' Cy5

## 3.8 Bibliography

1. Wang, Z. et al. DNA nanotechnology-facilitated ligand manipulation for targeted therapeutics and diagnostics. *Journal of Controlled Release* 340, 292–307 (2021).
2. Seeman, N. C. & Sleiman, H. F. DNA nanotechnology. *Nat Rev Mater* 3, 1–23 (2017).
3. Muro, S. Challenges in design and characterization of ligand-targeted drug delivery systems. *J Control Release* 164, 125–137 (2012).
4. Martinez-Veracochea, F. J. & Frenkel, D. Designing super selectivity in multivalent nano-particle binding. *Proceedings of the National Academy of Sciences* 108, 10963–10968 (2011).
5. Samaržija, I. et al. Integrin Crosstalk Contributes to the Complexity of Signalling and Unpredictable Cancer Cell Fates. *Cancers* 12, 1910 (2020).
6. Young, J. L. et al. Integrin Subtypes and Nanoscale Ligand Presentation Influence Drug Sensitivity in Cancer Cells. *Nano Lett.* 20, 1183–1191 (2020).
7. *Integrin Targeting Systems for Tumor Diagnosis and Therapy.* (Humana Press, 2018).
8. Juliano, R. L., Ming, X., Nakagawa, O., Xu, R. & Yoo, H. Integrin Targeted Delivery of Gene Therapeutics. *Theranostics* 1, 211–219 (2011).
9. Marelli, U. K., Rechenmacher, F., Sobahi, T. R. A., Mas-Moruno, C. & Kessler, H. Tumor Targeting via Integrin Ligands. *Front Oncol* 3, (2013).
10. Zhao, J., Santino, F., Giacomini, D. & Gentilucci, L. Integrin-Targeting Peptides for the Design of Functional Cell-Responsive Biomaterials. *Biomedicines* 8, (2020).
11. Wang, H., Luo, X. & Leighton, J. Extracellular Matrix and Integrins in Embryonic Stem Cell Differentiation. *Biochem Insights* 8, 15–21 (2015).
12. Ruoslahti, E. RGD and other recognition sequences for integrins. *Annu Rev Cell Dev Biol* 12, 697–715 (1996).
13. Pierschbacher, M. D. & Ruoslahti, E. Cell attachment activity of fibronectin can be duplicated by small synthetic fragments of the molecule. *Nature* 309, 30–33 (1984).
14. Dhavalikar, P. et al. Review of Integrin-Targeting Biomaterials in Tissue Engineering. *Advanced Healthcare Materials* 9, 2000795 (2020).
15. Hersel, U., Dahmen, C. & Kessler, H. RGD Modified Polymers: Biomaterials for Stimulated Cell Adhesion and Beyond. *Biomaterials* 24, 4385–415 (2003).
16. Ludwig, B. S., Kessler, H., Kossatz, S. & Reuning, U. RGD-Binding Integrins Revisited: How Recently Discovered Functions and Novel Synthetic Ligands (Re-)Shape an Ever-Evolving Field. *Cancers* 13, 1711 (2021).
17. Bastings, M. M. et al. From phage display to dendrimer display: Insights into multivalent binding. *Journal of the American Chemical Society* 133, 6636–6641 (2011).
18. Kaiser, E., Colecott, R. L., Bossinger, C. D. & Cook, P. I. Color test for detection of free terminal amino groups in the solid-phase synthesis of peptides. *Analytical Biochemistry* 34, 595–598 (1970).
19. Mohri, K. et al. Design and Development of Nanosized DNA Assemblies in Polypod-like Structures as Efficient Vehicles for Immunostimulatory CpG Motifs to Immune Cells. *ACS Nano* 6, 5931–5940 (2012).
20. Zadeh, J. N. et al. NUPACK: Analysis and design of nucleic acid systems. *J Comput Chem* 32, 170–173 (2011).
21. Eklund, A. S., Comberlato, A., Parish, I. A., Jungmann, R. & Bastings, M. M. C. Quantification of Strand Accessibility in Biostable DNA Origami with Single-Staple Resolution. *ACS Nano* (2021)

22. Strauss, S. et al. Modified aptamers enable quantitative sub-10-nm cellular DNA-PAINT imaging. *Nat Methods* 15, 685–688 (2018).
23. Structure of integrin  $\alpha_5\beta_1$  in complex with fibronectin. *The EMBO Journal* 22, 4607–4615 (2003).
24. Bernhagen, D., De Laporte, L. & Timmerman, P. High-Affinity RGD-Knottin Peptide as a New Tool for Rapid Evaluation of the Binding Strength of Unlabeled RGD-Peptides to  $\alpha\nu\beta_3$ ,  $\alpha\nu\beta_5$ , and  $\alpha_5\beta_1$  Integrin Receptors. *Anal. Chem.* 89, 5991–5997 (2017).
25. Kapp, T. G. et al. A Comprehensive Evaluation of the Activity and Selectivity Profile of Ligands for RGD-binding Integrins. *Sci Rep* 7, 39805 (2017).
26. Lederer, H., May, R. P., Kjems, J. K., Baer, G. & Heumann, H. Solution structure of a short DNA fragment studied by neutron scattering. *European Journal of Biochemistry* 161, 191–196 (1986).
27. Mitchell, J. S., Glowacki, J., Grandchamp, A. E., Manning, R. S. & Maddocks, J. H. Sequence-Dependent Persistence Lengths of DNA. *J. Chem. Theory Comput.* 13, 1539–1555 (2017).
28. Lepzelter, D., Bates, O. & Zaman, M. Integrin Clustering in Two and Three Dimensions. *Langmuir* 28, 5379–5386 (2012).
29. Schumacher, S. et al. Structural insights into integrin  $\alpha_5\beta_1$  opening by fibronectin ligand. *Science Advances* 7, eabe9716 (2021).
30. Krishnamurthy, V. M., Semetey, V., Bracher, P. J., Shen, N. & Whitesides, G. M. Dependence of Effective Molarity on Linker Length for an Intramolecular Protein–Ligand System. *J. Am. Chem. Soc.* 129, 1312–1320 (2007).
31. Kubas, H. et al. Multivalent cyclic RGD ligands: influence of linker lengths on receptor binding. *Nuclear Medicine and Biology* 37, 885–891 (2010).
32. Gimeno, A. et al. Minimizing the Entropy Penalty for Ligand Binding: Lessons from the Molecular Recognition of the Histo Blood-Group Antigens by Human Galectin-3. *Angewandte Chemie International Edition* 58, 7268–7272 (2019).
33. Xin, Y., Zargariantabrizi, A. A., Grundmeier, G. & Keller, A. Magnesium-Free Immobilization of DNA Origami Nanostructures at Mica Surfaces for Atomic Force Microscopy. *Molecules* 26, 4798 (2021).
34. Hynes, R. O. Integrins: Bidirectional, Allosteric Signaling Machines. *Cell* 110, 673–687 (2002).
35. Li, J., Yan, J. & Springer, T. A. Low-affinity integrin states have faster ligand-binding kinetics than the high-affinity state. *eLife* 10, e73359 (2021).
36. Arjonen, A., Alanko, J., Veltel, S. & Ivaska, J. Distinct Recycling of Active and Inactive  $\beta_1$  Integrins. *Traffic* 13, 610–625 (2012).
37. Gahmberg, C. G. et al. Regulation of cell adhesion: a collaborative effort of integrins, their ligands, cytoplasmic actors, and phosphorylation. *Quarterly Reviews of Biophysics* 52, (2019).
38. Mana, G., Valdembrì, D. & Serini, G. Conformationally active integrin endocytosis and traffic: why, where, when and how? *Biochem Soc Trans* 48, 83–93 (2020).
39. Changede, R., Cai, H., Wind, S. J. & Sheetz, M. P. Integrin nanoclusters can bridge thin matrix fibres to form cell–matrix adhesions. *Nature Materials* 18, 1366–1375 (2019).
40. Moreno-Layseca, P., Icha, J., Hamidi, H. & Ivaska, J. Integrin trafficking in cells and tissues. *Nat Cell Biol* 21, 122–132 (2019).
41. De Franceschi, N., Hamidi, H., Alanko, J., Sahgal, P. & Ivaska, J. Integrin traffic – the update. *Journal of Cell Science* 128, 839–852 (2015).
42. Hou, J., Yan, D., Liu, Y., Huang, P. & Cui, H. The Roles of Integrin  $\alpha_5\beta_1$  in Human Cancer. *OTT* 13, 13329–13344 (2020).
43. Hamidi, H. & Ivaska, J. Every step of the way: integrins in cancer progression and metastasis. *Nat Rev Cancer* 18, 533–548 (2018).
44. Clark, K. et al. A specific  $\alpha_5\beta_1$ -integrin conformation promotes directional integrin translocation and fibronectin matrix formation. *Journal of Cell Science* 118, 291–300 (2005).
45. Martinez-Veracochea, F. J. & Frenkel, D. Designing super selectivity in multivalent nano-particle binding. *Proceedings of the National Academy of Sciences* 108, 10963–10968 (2011).
46. Curk, T., Dobnikar, J. & Frenkel, D. Optimal multivalent targeting of membranes with many distinct receptors. *Proc. Natl. Acad. Sci. U.S.A.* 114, 7210–7215 (2017).
47. Dubacheva, G. V., Curk, T., Auzély-Velty, R., Frenkel, D. & Richter, R. P. Designing multivalent probes for tunable superspecific targeting. *PNAS* 112, 5579–5584 (2015).
48. Möckl, L. et al. The glycocalyx regulates the uptake of nanoparticles by human endothelial cells in vitro. *Nanomedicine* 12, 207–217 (2017).
49. Wijesekara, P. et al. Accessing and Assessing the Cell-Surface Glycocalyx Using DNA Origami. *Nano Lett.* 21, 4765–4773 (2021).
50. Tseng, C. Y., Wang, W. X., Douglas, T. R. & Chou, L. Y. T. Engineering DNA Nanostructures to Manipulate Immune Receptor Signaling and Immune Cell Fates. *Advanced Healthcare Materials* 11, 2101844 (2022).
51. Paszek, M. J. et al. The cancer glycocalyx mechanically primes integrin-mediated growth and survival. *Nature* 511, 319–325 (2014).

52. Peccati, F. & Jiménez-Osés, G. Enthalpy–Entropy Compensation in Biomolecular Recognition: A Computational Perspective. *ACS Omega* 6, 11122–11130 (2021).
53. Vicente-Manzanares, M. & Horwitz, A. R. Adhesion dynamics at a glance. *J Cell Sci* 124, 3923–3927 (2011).
54. Morzy, D. & Bastings, M. Significance of Receptor Mobility in Multivalent Binding on Lipid Membranes. *Angewandte Chemie International Edition* 61, e202114167 (2022).
55. Paszek, M. J., Boettiger, D., Weaver, V. M. & Hammer, D. A. Integrin Clustering Is Driven by Mechanical Resistance from the Glycocalyx and the Substrate. *PLoS Comput Biol* 5, e1000604 (2009).
56. Yamada, K. M., Pankov, R. & Cukierman, E. Dimensions and dynamics in integrin function. *Braz J Med Biol Res* 36, 959–966 (2003).
57. Campbell, I. D. & Humphries, M. J. Integrin Structure, Activation, and Interactions. *Cold Spring Harbor Perspectives in Biology* 3, a004994–a004994 (2011).
58. Dai, A. et al. The Structure of a Full-length Membrane-embedded Integrin Bound to a Physiological Ligand. *J Biol Chem* 290, 27168–27175 (2015).
59. Möckl, L. The Emerging Role of the Mammalian Glycocalyx in Functional Membrane Organization and Immune System Regulation. *Frontiers in Cell and Developmental Biology* 8, (2020).
60. Reitsma, S., Slaaf, D. W., Vink, H., van Zandvoort, M. A. M. J. & oude Egbrink, M. G. A. The endothelial glycocalyx: composition, functions, and visualization. *Pflugers Arch* 454, 345–359 (2007).
61. Agrawal, N. J. & Radhakrishnan, R. The Role of Glycocalyx in Nanocarrier-Cell Adhesion Investigated Using a Thermodynamic Model and Monte Carlo Simulations. *J. Phys. Chem. C* 111, 15848–15856 (2007).
62. U. Atukorale, P. et al. Influence of the glycocalyx and plasma membrane composition on amphiphilic gold nanoparticle association with erythrocytes. *Nanoscale* 7, 11420–11432 (2015).
63. Bae, G. et al. Receptor-Level Proximity and Fastening of Ligands Modulates Stem Cell Differentiation. *Advanced Functional Materials*, 2200828 (2022).
64. Ponnuswamy, N. et al. Oligolysine-based coating protects DNA nanostructures from low-salt denaturation and nuclease degradation. *Nat Commun* 8, 15654 (2017).
65. Navas-Moreno, M. et al. Nanoparticles for live cell microscopy: A surface-enhanced Raman scattering perspective. *Sci Rep* 7, 4471 (2017).
66. Thurn, K. T. et al. Nanoparticles for Applications in Cellular Imaging. *Nanoscale Res Lett* 2, 430–441 (2007).
67. Huang, D., Patel, K., Perez-Garrido, S., Marshall, J. F. & Palma, M. DNA Origami Nanoarrays for Multivalent Investigations of Cancer Cell Spreading with Nanoscale Spatial Resolution and Single-Molecule Control. *ACS Nano* 13, 728–736 (2019).
68. Veneziano, R. et al. Role of nanoscale antigen organization on B-cell activation probed using DNA origami. *Nature Nanotechnology* 15, 716–723 (2020).
69. Liu, Y. et al. The effects of overhang placement and multivalency on cell labeling by DNA origami. *Nanoscale* 13, 6819–6828 (2021).
70. Cremers, G. A. O. et al. Determinants of Ligand-Functionalized DNA Nanostructure–Cell Interactions. *J. Am. Chem. Soc.* 143, 10131–10142 (2021).
71. Pulous, F. E. & Petrich, B. G. Integrin-dependent regulation of the endothelial barrier. *Tissue Barriers* 7, 1685844 (2019).
72. Sheppard, D. Endothelial integrins and angiogenesis: not so simple anymore. *J Clin Invest* 110, 913–914 (2002).
73. Wolpe, A. G., Ruddiman, C. A., Hall, P. J. & Isakson, B. E. Polarized Proteins in Endothelium and Their Contribution to Function. *JVR* 58, 65–91 (2021).
74. Grove, L. M. et al. Urokinase-type Plasminogen Activator Receptor (uPAR) Ligation Induces a Raft-localized Integrin Signaling Switch That Mediates the Hypermotile Phenotype of Fibrotic Fibroblasts \*. *Journal of Biological Chemistry* 289, 12791–12804 (2014).
75. Ferraris, G. M. S. et al. The interaction between uPAR and vitronectin triggers ligand-independent adhesion signalling by integrins. *EMBO J* 33, 2458–2472 (2014).
76. Wang, Y., Baars, I., Fördös, F. & Högberg, B. Clustering of Death Receptor for Apoptosis Using Nanoscale Patterns of Peptides. *ACS Nano* 15, 9614–9626 (2021).
77. Ye, N. et al. Direct observation of  $\alpha$ -actinin tension and recruitment at focal adhesions during contact growth. *Exp Cell Res* 327, 57–67 (2014).
78. Pasapera, A. M., Schneider, I. C., Rericha, E., Schlaepfer, D. D. & Waterman, C. M. Myosin II activity regulates vinculin recruitment to focal adhesions through FAK-mediated paxillin phosphorylation. *Journal of Cell Biology* 188, 877–890 (2010).
79. Chen, C. S., Alonso, J. L., Ostuni, E., Whitesides, G. M. & Ingber, D. E. Cell shape provides global control of focal adhesion assembly. *Biochemical and Biophysical Research Communications* 307, 355–361 (2003).
80. Legerstee, K., Geverts, B., Slotman, J. A. & Houtsmuller, A. B. Dynamics and distribution of paxillin, vinculin, zyxin and VASP depend on focal adhesion location and orientation. *Scientific Reports* 9, 10460 (2019).
81. Gardel, M. L., Schneider, I. C., Aratyn-Schaus, Y. & Waterman, C. M. Mechanical Integration of Actin and Adhesion Dynamics in Cell Migration. *Annu Rev Cell Dev Biol* 26, 315–333 (2010).

82. Zamir, E. & Geiger, B. Molecular complexity and dynamics of cell-matrix adhesions. *Journal of Cell Science* 114, 3583–3590 (2001).
83. Tang, Q. & Han, D. Obtaining Precise Molecular Information via DNA Nanotechnology. *Membranes* 11, 683 (2021).
84. Li, X. et al. DNA-Based Molecular Engineering of the Cell Membrane. *Membranes* 12, 111 (2022).
85. Huang, J. et al. Arranging Small Molecules with Sub-Nanometer Precision on DNA Origami Substrates for the Single-Molecule Investigation of Protein-Ligand Interactions. *Small Structures* (2022).
86. Ambrosetti, E. et al. A DNA-nanoassembly-based approach to map membrane protein nanoenvironments. *Nat. Nanotechnol.* 16, 85–95 (2021).
87. Scheepers, M. R. W., IJzendoorn, L. J. van & Prins, M. W. J. Multivalent weak interactions enhance selectivity of interparticle binding. *PNAS* (2020).
88. Miyazaki, N., Iwasaki, K. & Takagi, J. A systematic survey of conformational states in  $\beta_1$  and  $\beta_4$  integrins using negative-stain electron microscopy. *Journal of Cell Science* 131, jcs216754 (2018).
89. Su, Y. et al. Relating conformation to function in integrin  $\alpha_5\beta_1$ . *Proc. Natl. Acad. Sci. U.S.A.* 113, E3872-3881 (2016).
90. Aota, S., Nomizu, M. & Yamada, K. M. The short amino acid sequence Pro-His-Ser-Arg-Asn in human fibronectin enhances cell-adhesive function. *Journal of Biological Chemistry* 269, 24756–24761 (1994).
91. Liu, Y. et al. HUVEC cell affinity evaluation and integrin-mediated mechanism study on PHSRN-modified polymer. *Colloids and Surfaces B: Biointerfaces* 84, 6–12 (2011).
92. Singh, J. P. & Young, J. L. The cardiac nanoenvironment: form and function at the nanoscale. *Biophys Rev* 13, 625–636 (2021).
93. Young, J. L. et al. Integrin Subtypes and Nanoscale Ligand Presentation Influence Drug Sensitivity in Cancer Cells. *Nano Lett.* 20, 1183–1191 (2020).
94. Kubiak, A. et al. Stiffening of DU145 prostate cancer cells driven by actin filaments – microtubule crosstalk conferring resistance to microtubule-targeting drugs. *Nanoscale* 13, 6212–6226 (2021).
95. Ungai-Salánki, R. et al. Single-cell adhesion strength and contact density drops in the M phase of cancer cells. *Sci Rep* 11, 18500 (2021).

# Chapter 4 Cell response to RGD-liganded rigid, multivalent DNA scaffolds

A study of integrin ligand presentation for cell adhesion and migration revealed to be differently modulated in the 35nm to 70nm regime<sup>1</sup> with others reporting on activated integrin availability being more pronounced when ligands were not presented in a homogeneous manner.<sup>2-4</sup> Recent findings have also demonstrated the ability of receptors to cluster and bind ligands spaced 7nm apart on different cell types. This raises the question if ligand geometries in the sub-60nm regime elicits selective cell adhesion or migratory response especially given that these spacings (<100nm) are within the regime of periodic spacings found on fibronectin.<sup>5-7</sup>

To test the hypothesis, we employ randomly immobilised Multivalent Scaffolds presenting RGD ligands with different local (intra-scaffold) and global (inter-scaffold) spacings and geometries to study the impact of ligand presentation on those length scales on HUVEC adhesion formation. The resulting regimes of adhesion clusters formed revealed boundaries in peripheral versus central Multivalent Scaffold ligand presentation in triggering selective cell response in the regime of inter adhesion cluster spacings reported by Schlichthaerle et al. of 20-30nm.<sup>8</sup> Interestingly, ligands bridging the periphery and centre of the Multivalent Scaffold resulted in subpopulations of HUVECs displaying distinct regimes of cell adhesion. Of note, the heterogeneity in ligand spacings arising from randomly absorbed Multivalent Scaffolds with a full coverage of 36 ligands was not capable of inducing large adhesion cluster formation.

Author contributions : Experimental design, planning, data processing: E.E.Kurisinkal. Experimental work and confocal imaging: M.M.Koga.

## 4.1 Introduction

Cell adhesion is mediated by integrins from initial adhesion to clustering upon binding to ECM ligands, where adhesion maturation follows cell spreading and flattening.<sup>9,10</sup> Integrins engagement is reportedly influenced by ligand geometries,<sup>9,11</sup> dynamically shaping the actin cytoskeleton, directing cell shape and motility.<sup>12</sup> Disruptions in the focal adhesions machinery including integrin ligand binding have otherwise been implicated in diseases.<sup>13,14</sup> Since an initial study reporting on a minimal adhesion unit for fibronectin of 4 liganded integrins within 60nm of spacing,<sup>15</sup> studies

have been conducted investigating patterns of ligands in 1D versus 2D,<sup>11,16–19</sup> probing integrin subtype specific spatial tolerance<sup>20,21</sup> and the influence of global versus local ligand spacings.<sup>2,22</sup>

Recent findings from Chapter 3 revealed the ability of integrin  $\alpha_5\beta_1$  on HUVECs to cluster upon SNAKA51 antibody activation, binding to RGD-liganded Bivalent Scaffolds with rigid nanoscale spacings. This led us to probe integrin  $\alpha_5\beta_1$  the engagement for HUVECs adhesion in terms of geometries of local valencies and spacings at different global inter-geometry spacings. For this, we employ Multivalent Scaffolds of 60nm in diameter with triangular or hexagonal RGD ligand geometries ranging 7-25nm. Monovalent RGD and complete coverage (36 RGD ligands) were included as controls. Here we test the ability of low density, sub-30nm ligand geometric patterns in engaging HUVEC adhesion formation with inter-ligand geometry spacings of 60nm (scaffold dimensions) and below Figure 4.1.

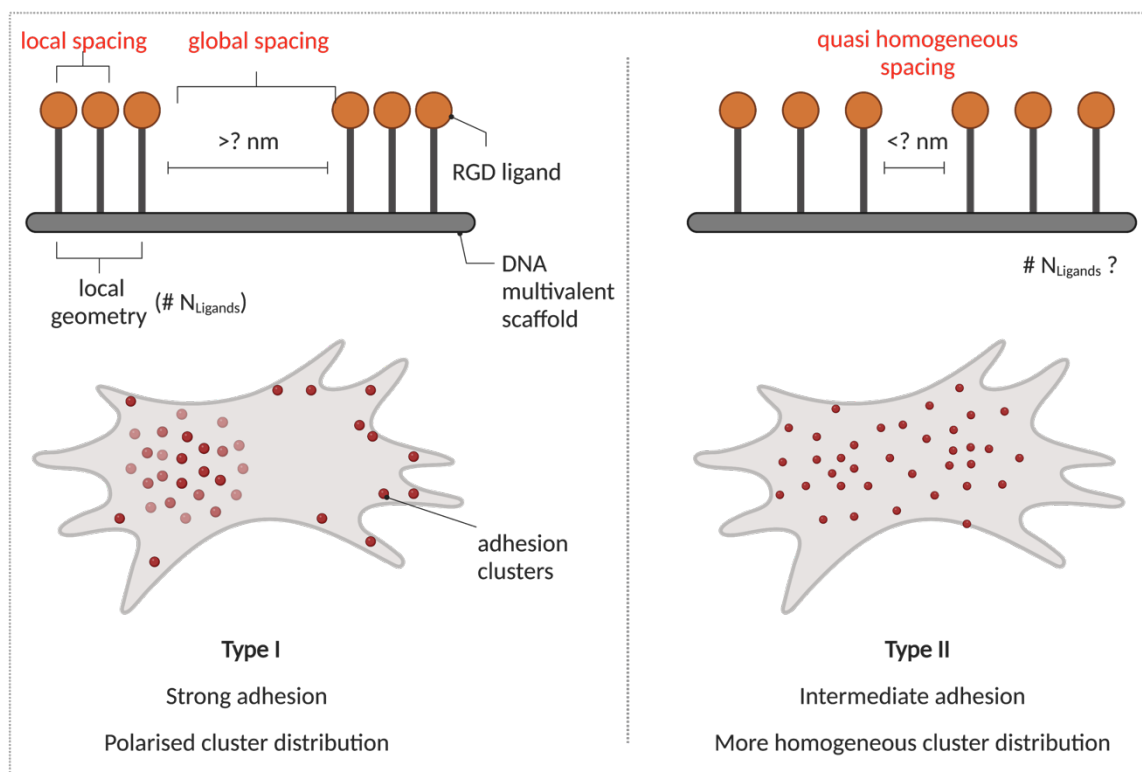


Figure 4.1 Chapter overview. HUVEC adhesion cluster formation to RGD liganded Multivalent Scaffolds with geometries of local valencies and spacings at varying global inter-geometry spacings.

As cell response is mediated by an ensemble of factors, not merely RGD ligand geometry, we include other hallmarks of cell adhesion, notably actin cytoskeleton formation (F-actin), adhesion formation (talin-1 and integrin  $\alpha_5\beta_1$  in extended conformations) as well as cell and nucleus shape in our analysis of HUVEC cell response to ligand presentation.<sup>10</sup> We then analyse HUVEC response to the RGD-ligand presentations.



## 4.2 Methods and materials

### 4.2.1. Materials

Unless otherwise specified, reagents were used as received without further modification. Deionized water obtained from a Milli-Q water purification system was used for all experiments. DPBS (Cat.No. 14040091) and BSA 7.5% solution (Cat.No. 15260037) were purchased from Life Technologies EU BV. All buffers were filtered with 0.22 $\mu$ m PES syringe filters (Cat.No. 431229, Corning) or PES bottle filters (Cat.No. 431097, Corning). HUVEC (Cat.No. C2517AS), Reagent Pack™ Subculture Reagents (Cat.No. CC-5034) and EGM2 endothelial cell growth medium-2 bulletKit (Cat.No. CC-3162) was purchased from Lonza, Basel, Switzerland. 0.05% Trypsin-EDTA (Cat.No. 25300054) was purchased from Gibco. Donkey Anti-Rabbit IgG H&L Alexa Fluor® 647 (Cat.No. 150075) 1:500, DAPI staining solution (Cat.No. ab228549) 1:1000, Rhodamine-Phalloidin (Cat.No. ab235138) and Goat Anti-Mouse IgG H&L Alexa Fluor® 488 (Cat.No. ab150113) 1:500 were purchased from abcam. Talin-1 Polyclonal antibody (Cat.No.14169-1-AP) was purchased from Proteintech. Integrin alpha 5/CD49e antibody (SNAKA51) (Cat.No. NBP2-50146) 1:250 was purchased from Novus Biologicals. ibidi  $\mu$ -Slide Angiogenesis Glass bottom (Cat.No. 81507) was purchased from Vitaris AG. Tris Buffer, 2M, (Cat.No. BP1759), Piperazine-N,N'-bis(2-ethanesulfonic acid) 1M, PIPES (Cat.No. 15404879), Methanol (Cat.No. M/4060/PB17) Tris-borate-EDTA, TBE Buffer, (10X) (Cat.No. BP1333-1) and 4%PFA (Cat.No. 15424389) was purchased from Fisher Scientific. ( $\pm$ )-6-Hydroxy-2,5,7,8-tetramethylchromane-2-carboxylic acid, Trolox, 97% (Cat.No. 238813), 3,4-Dihydroxybenzoic acid, >97%, PCA (Cat.No. 37580), Protocatechuate 3,4-Dioxygenase from *Pseudomonas* sp., PCD (Cat.No. P8279), Dextran sulfate sodium salt from *Leuconostoc* spp. mol wt 6,500-10,000, (Cat.No. D4911), Sodium chloride solution 5M (Cat.No. S5150), Ethylene glycol-bis(2-aminoethylether)-N,N,N',N'-tetraacetic acid, EGTA (Cat.No. 200-651-2), Sucrose (Cat.No. S0389), Deoxyribonucleic acid, single stranded from salmon testes (Cat.No. D7656), 1-Hydroxybenzotriazole hydrate, HOBt (Cat.No. 711489), dichloromethane, DCM (Cat.No. 270997), Trifluoroacetic acid, TFA (Cat.No. T6508), Phenol (Cat.No. 33517), Diethyl ether (Cat.No. 32203), Dibenzocyclooctyne-maleimide, DBCO-maleimide, (Cat.No. 760668), Anhydrous Dimethyl sulfoxide, DMSO (Cat.No. 472301), and Magnesium Chloride solution 1M (Cat.No. M1028) was purchased from Merck. Ethylenediaminetetraacetic acid 0.5M, EDTA (Cat.No. J60292) and 1,2 ethanedithiol, EDT (Cat.No. L12865) was purchased from Alfa Aesar. Glycerol (Cat.No. AB113718), O-benzotriazole-N,N,N',N'- tetramethyluroniumhexafluorophosphate, HBTU (Cat.No. AB12886), diisopropylethylamine, DIPEA (Cat.No. AB182190) and N-methylpyrrolidine, NMP (Cat.No. AB182195) were purchased from ABCR. Tween-20 (Cat.No. BIT0803) and Tris hydrochloride, Tris-HCl (Cat.No. BIT1513) was purchased from Apollo Scientific. Potassium chloride (Cat.No. 6781.1), Agarose (Cat.No. 3810.2), Triethylamine, TEA (Cat. No. X875.2) and Sodium chloride (Cat.No. 3957.1) was purchased from Carl Roth. Fmoc protected peptides were purchased from Merck as follows : Fmoc-Cys(Trt)-OH (Cat.No. 8520080025), Fmoc-Gly-OH (Cat.No. 8520010025), Fmoc-Arg(Pbf)-OH (Cat.No. 8520670025), Fmoc-Ala-OH (Cat.No. 8520030025), Fmoc-Asp(OtBu)-OH, (Cat.No. 8520050025), Fmoc-Ser(tBu)-OH (Cat.No. 8520190025). Fmoc-Rink Amide MBHA resin (Cat.No. AS-20083) was

purchased from Anaspec. Argon ALPHAGAZ™ (Cat.No. P0022L50S2A001) was purchased from Air Liquide. ssDNA scaffold type p7560 (Cat.No. M1-30) was obtained from Tilibit. 40% acrylamide and bis-acrylamide solution 19:1, (Cat.No. 1610144) was purchased from Bio-Rad. Ammonium persulfate, APS (Cat.No. 231-786-5) was purchased from VWR. N,N,N',N'-tetramethylethylenediamine, TEMED (Cat.No. A1148), Gold Nucleic Acid Gel Stain (Cat.No. S11494), SYBR™ Safe DNA Gel Stain, (Cat.No. S33102), GeneRuler Ultra Low Range DNA Ladder (Cat.No. SM1213), 1kb Plus DNA Ladder (Cat.No. 10787018), 6X DNA Loading Dye (Cat.No. R0611), TriTrack DNA Loading Dye (Cat.No. R1161), Zeba™ Micro Spin Desalting Columns, 7K MWCO (Cat.No. 89883), Pierce™ C18 Spin Columns (Cat.No. 89870), Streptavidin (Cat.No. 21122) and Pierce™ Immobilized TCEP Disulfide Reducing Gel (Cat.No. 77712) were purchased from Thermo Fisher Scientific. Acetonitrile >99.9% HPLC grade, (Cat. No. FSHA/0627/17-4) was purchased from Chemie Brunschwig AG.

#### 4.2.2. ssDNA strands

All ssDNA strands listed below were ordered from Integrated DNA Technologies, Coralville, Iowa, USA, with modification when indicated in Appendix 4.5.2.

#### 4.2.3. Instruments

Reverse phase analytical High Pressure Liquid Chromatography (RP-HPLC) (Dionex Ultimate 3000 U-HPLC, Thermo Scientific) equipped with Hypersil Gold™ C18, 150x4 mm column (3µm diameter) was used for peptide and peptide conjugated characterisation. Peptide molecular weight was analysed by electrospray ionization mass spectrometry (ESI-MS) (LTQ Orbitrap ELITE ETD, ThermoFisher Scientific). HERMLE Z366 HK centrifuge was used for centrifugation steps. Agarose and Polyacrylamide (PAGE) gel electrophoresis were performed in or Biometra eco-mini gel tank (Analytic Jena). Gel images were acquired by the Bio-Rad ChemiDoc MP imaging system (Hercules, California, USA) and analysed with Bio-Rad ImageLab software. Fluorescence intensity measurements and imaging of samples were performed on the BioTek™ Cytation 5™ and Gen5 software, Version 3.10 (Winooski, Vermont, USA). ssDNA and dsDNA concentrations were acquired from the Quawell Q9000 nanodrop spectrometer. Annealing programs of DNA scaffolds were conducted on the Biometra trio thermocycler (Analytical Jena). Confocal imaging was conducted on a Zeiss LSM980 with Colibri 5 illumination for fluorescence and ZEN Blue software version 3.4.91.

#### 4.2.4. Multivalent, Rigid DNA Scaffold preparation & characterisation

RGD peptide synthesis and characterisation and ssDNA-peptide conjugation was performed as detailed in 3.4.1. Multivalent, Rigid DNA Scaffold were prepared as detailed a publication by Eklund et al.<sup>23</sup> Ligand functionalised ssDNA antihandle were annealed in 3X molar excess per handle to the Multivalent, Rigid Scaffold was performed in a Thermal Cycler with the following program : Samples were heated to 37°C for 2h, cooled to 28°C over 12h and stored at 4°C. 5µL,

10nM samples were loaded on 1% agarose gels with 1kb Plus ladder as reference. Peptide antihandle annealing was tested with further incubation with 3X molar excess of Cy5 conjugated antihandles. Gels were run for 90 mins at 70V.

Multivalent Scaffold surface immobilisation was adapted from a previous publication.<sup>24</sup> Streptavidin was diluted to a concentration of 300nM in MilliQ, coated on wells and stored at 4°C overnight. Wells were washed with PBS and blocked with 3% BSA for 30 minutes at 37°C prior to Multivalent Scaffold immobilisation. Multivalent Scaffolds, 4nM were immobilised for 30 mins at RT in EGM2-/Mg-Na/BSA (media without FBS supplemented with 18mM MgCl<sub>2</sub>, 5mM NaCl and 3% BSA). Wells were washed with EGM2-/Mg-Na/BSA prior to cell seeding.

#### 4.2.5. HUVEC response to RGD liganded Multivalent, Rigid DNA Scaffold

HUVECs were seeded for at least 24h at 37°C, 5% CO<sub>2</sub>, 95% relative humidity. HUVECs were serum starved overnight and incubated for 1h in full media prior to experiments. HUVECs were trypsinised, resuspended in EGM2-/Mg-Na/BSA, seeded in experimental wells and incubated at 37°C, 5% CO<sub>2</sub>, 95% relative humidity. After 1h, the wells were washed with EGM2-/Mg-Na/BSA and incubated for a further 1h30. The following steps were conducted at RT. Cells were fixed in 2%PFA and 1X cytoskeleton buffer (1M NaCl, 0.1M PIPES, 30mM MgCl<sub>2</sub>, 10mM EGTA, 10mM sucrose) for 15min then washed with Multivalent Scaffold Buffer (18mM MgCl<sub>2</sub>, 5mM NaCl, 5mM TRIS, 1mM EDTA) and imaged in Multivalent Scaffold Imaging Buffer (In PBS 1X : 0.5M NaCl, 18mM MgCl<sub>2</sub>, Trolox 1X, PCA 1X, PCD 1X)

Stock solutions for the imaging buffers were prepared as follows<sup>25</sup> : (i) Trolox 100X (100mg Trolox, 430µL 100% methanol, 345µL 1M NaOH, 3.2mL MilliQ) (ii) PCA 40X (154mg PCA in total 10mL MilliQ after pH 9.0 adjustment with NaOH) (iii) PCD 100X (9.3mg PCD in 13.3mL PCD buffer) (iv) PCD buffer (100mM TRIS-HCl pH8, 50mM KCl, 1mM EDTA, 50% glycerol)

Confocal microscopy 63X images were acquired in 3 channels, DAPI, Alexa647, Alexa546 and Alexa488. The images were acquired as z-stacks of 0.4µm. Images of single cells were post-processed in Fiji software in all channels as follows, (i) hard thresholded (ii) LUT, Alexa647 : Red Hot; Alexa546 : Orange Hot; Alexa488 : Green; DAPI : Blue.

### 4.3 HUVEC adhesion to RGD liganded Multivalent Scaffolds

#### 4.3.1 RGD liganded Multivalent Scaffolds

Multivalent Scaffolds Figure 4.2. (top) were characterised by AGE prior to experiments, Figure 4.2. (bottom) having 36 potential sites for functionalisation. Multivalent Scaffolds were then immobilised as described in 4.2.4 with 7 biotinylated ssDNA annealed on the bottom face of the scaffold. Streptavidin was immobilised for complete surface coverage and biotinylated Multivalent Scaffolds immobilised subsequently. Scaffolds were prepared to present valencies of 1, 3, 6 and 36. Ligands were spaced at ~7nm (Multi-3-7 and Multi-6-7) or ~ 25nm for Multi-3-25 and ~20nm Multi-6-20 as characterised in a recent publication from our laboratory.<sup>23</sup> Ligand geometries on the

Multivalent Scaffolds were designed to be centrally located, in the periphery of the scaffold or bridging the centre and periphery of the scaffold. This allows us to probe different global inter-ligand geometry spacings ranging from 60nm (Mono-1) to being in contact (Multi-6-20 and Multi-36-7). Multi-36-7 was included as a control for geometric presentation of RGD ligands with a saturating density of 36 RGD ligands on the Multivalent Scaffold. RGD Ligand-antihandle were synthesised and characterised as detailed in Chapter 3.

#### 4.3.2 HUVEC response to RGD liganded Multivalent Scaffolds

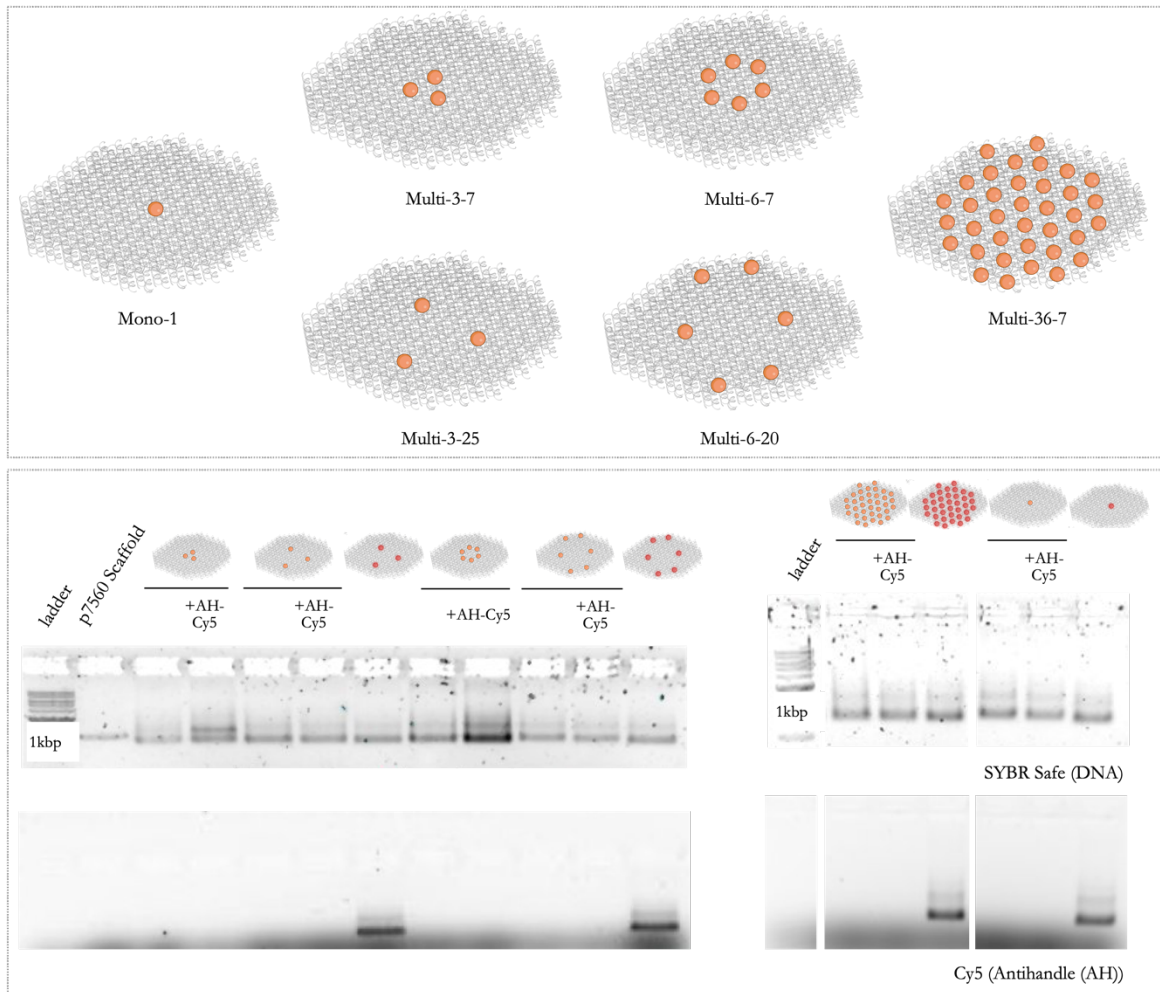


Figure 4.2 Top : Multivalent Scaffold ligand geometries and spacings. Bottom : Characterisation scaffold functionalisation with Cy5 conjugated antihandles annealed in excess to pre-ligand functionalised Multivalent Scaffolds.

In our experiments, we assessed cell adhesion within 3h of seeding previously serum-starved cells in media without FBS to prevent any cell adhesion due exogenous or endogenous Fibronectin.<sup>26,27</sup> Although the global density of RGD ligands per surface area varies across the valencies tested, that is the valencies of 36, 6 and 3 have respectively the proportional increase in ligand density compared to the Monovalent Scaffold, we estimate that the local RGD ligand geometry and inter-geometry distances, Figure 4.3 would prevail in cell adhesion formation allowing us to compare the conditions despite different overall ligand densities. This is based on previous reports of local

RGD ligand geometry dictating cell adhesion<sup>11,16</sup> beyond a critical minimum average (global) density, reportedly  $1\text{fmol cm}^{-2}$  for cell spreading and  $10\text{fmol cm}^{-2}$  for focal contact and stress fibre formation,<sup>9</sup> of which we are an order of magnitude of concentration higher with the most conservative estimates. A uniform distribution of Multivalent Scaffolds is unlikely to provide a significant advantage in regulating cell response in comparison to our experimental setup. This has been posited by the heterogeneity of integrin cluster distribution and the average number of integrins on the cell surface within the Scaffold area and immediate vicinity likely being insensitive to local disorder in interparticle RGD spacing between Multivalent Scaffold due to random scaffold adsorption, albeit at a given island size.<sup>28,29</sup>

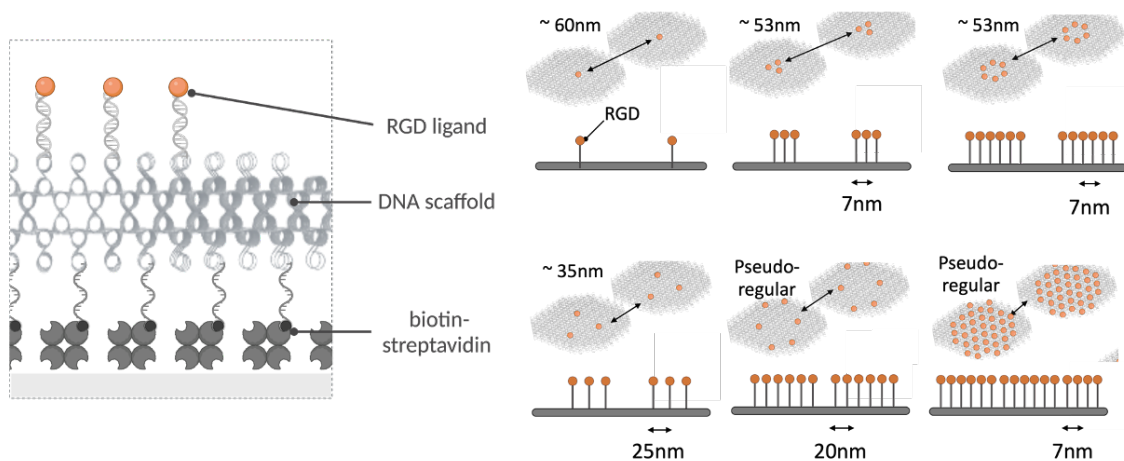


Figure 4.3 (Left) Surface immobilisation of RGD-liganded Multivalent Scaffolds. (Right) RGD local versus global ligand surface presentation.

The adhesion complex is composed of multiple proteins that vary in abundance and composition in time, but all comprise actin cytoskeleton, talin and integrin transmembrane receptors.<sup>30,31</sup> In our analysis of RGD ligand mediated cell adhesion, we use the following markers, Figure 4.4 (i) SNAKA51 activation specific antibody, to localise clusters of integrin  $\alpha_5\beta_1$  in extended conformations (ii) Phalloidin that stains filamentous-actin (F-actin), to analyse actin cytoskeleton distribution (iii) Talin-1 antibody that binds to talin that links integrin  $\beta$  tails to the actin cytoskeleton<sup>32</sup> when integrin  $\alpha_5\beta_1$  undergoes mechanotransduction upon ligand binding<sup>33</sup> and (iv) DAPI for the nucleus. Colocalisation of talin-1, SNAKA51 and F-actin is a marker of nascent adhesion formation.<sup>34</sup> The SNAKA51 antibody binds to integrin  $\alpha_5\beta_1$  high-ligand affinity extended conformations predominantly adopted by ligand bound integrins<sup>35,36</sup>, localising sites of integrin clustering when bound to the RGD ligands presented. The SNAKA51 activation specific antibody was chosen as a marker to distinguish activation-specific conformations from other integrin  $\alpha_5\beta_1$  conformations highly expressed on the endothelial cell surface. It should be noted that other RGD integrins present on HUVECs could also mediate cell adhesion, e.g. integrin  $\alpha_v\beta_3$ , albeit having relatively lower expression levels, weaker binding affinities or unliganded but residing within adhesions.<sup>19,37-39</sup> This should make integrin  $\alpha_5\beta_1$  the dominant receptor in engaging RGD ligands on HUVECs. Also, focal adhesion assembly in endothelial cells showed the successive recruitment of integrin  $\alpha_v\beta_3$  upon integrin  $\alpha_5\beta_1$  engagement.<sup>40</sup> Additionally, the localisation of the clusters of

integrin  $\alpha_5\beta_1$  either at the periphery of the cell or the cell interior relates to the maturity of the adhesions with nascent adhesion and focal adhesions closer to the cell periphery and fibrillar adhesions more centrally located within the cell.<sup>41</sup>

Talin-1 is an early adaptor protein that binds to activated integrins and promotes clustering.<sup>30,32,42</sup> In all models of mechanotransduction of integrins either inside-out (activation through intracellular signalling), outside-in (activation from integrin ligand binding), and ECM bound integrin regulation of bond strength, the ligand-receptor complex engages the actin cytoskeleton through talin, i.e. talin is only subjected to mechanical force when bound to integrin and the actin cytoskeleton.<sup>31,42</sup> As such, an antibody that binds to the Talin-1 isoform was chosen as a marker of FA formation as Talin-2 is reportedly absent on endothelial cells.<sup>31,43</sup>

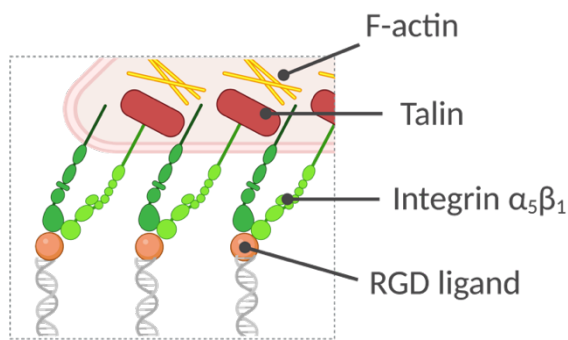


Figure 4.4 Focal adhesion markers employed. RGD ligands presented on DNA Scaffolds for integrin binding and subsequent talin and F-actin recruitment.

Phalloidin is a cyclic peptide that binds and stabilises F-actin and is commonly used in conjugation with fluorescent dyes to stain the cell actin-cytoskeleton.<sup>44</sup> F-actin staining would give us insight on actin fibre formation, localisation and thickness as well as give us insight on the general cell morphology and migratory versus adhesive behaviour of the cells.<sup>45,46</sup>

In our analysis, we take into account the overall cell morphology, dictated by the actin cytoskeleton and the nuclear morphology that in addition to responding to ligand geometry, has been shown to reflect local topography and integrity of cytoskeletal organisation in mechanical stress modulation.<sup>47-49</sup> Images considered in our discussion were of cells that were attached to substrates, not actively dividing and were void of contacts with other cells.

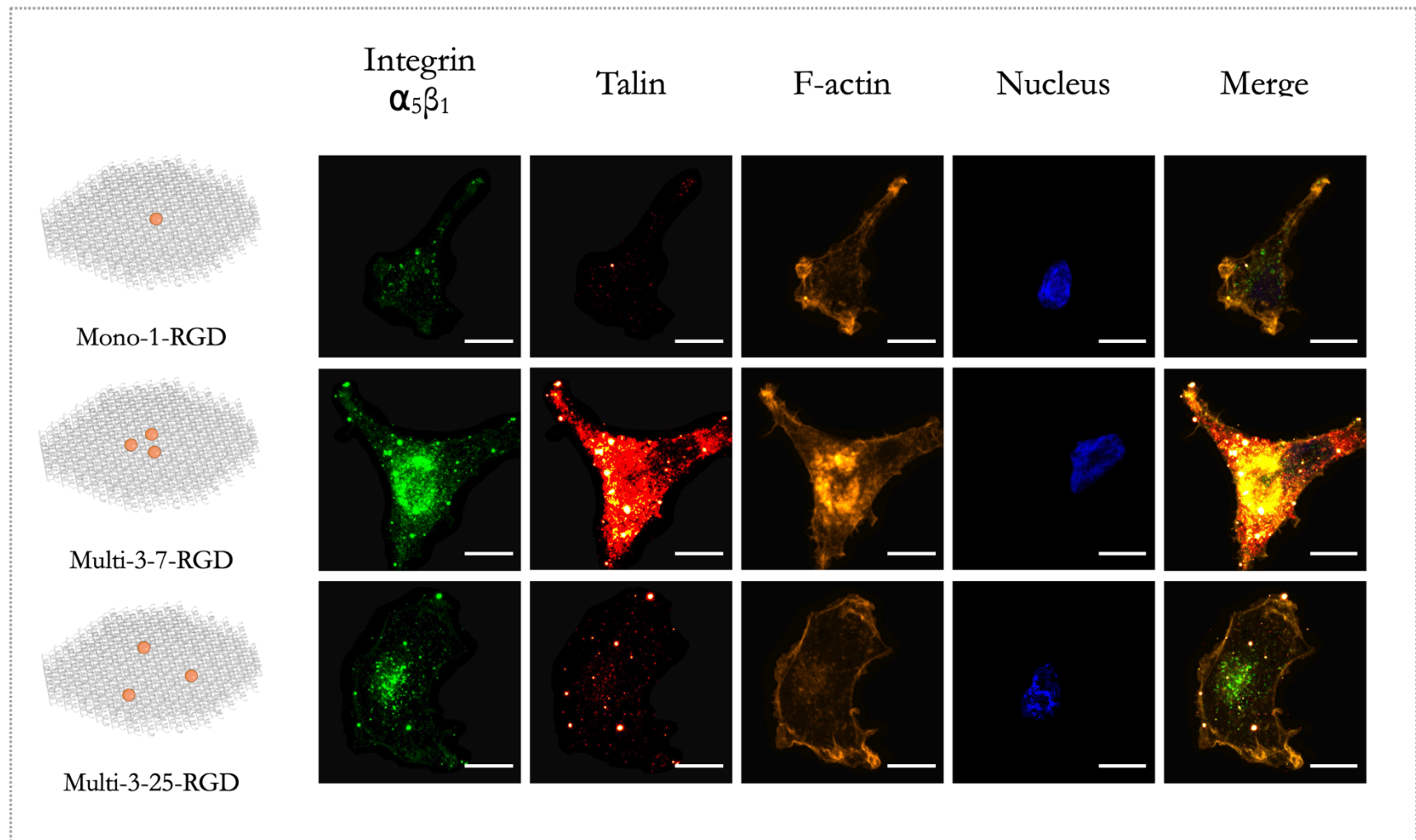


Figure 4.5 Adhesion marker (integrin  $\alpha_5\beta_1$ , talin, f-actin, nucleus) staining of HUVECs adhering to Mono-1-RGD, Multi-3-7-RGD and Multi-3-25-RGD. Scale bar: 10 $\mu$ m.

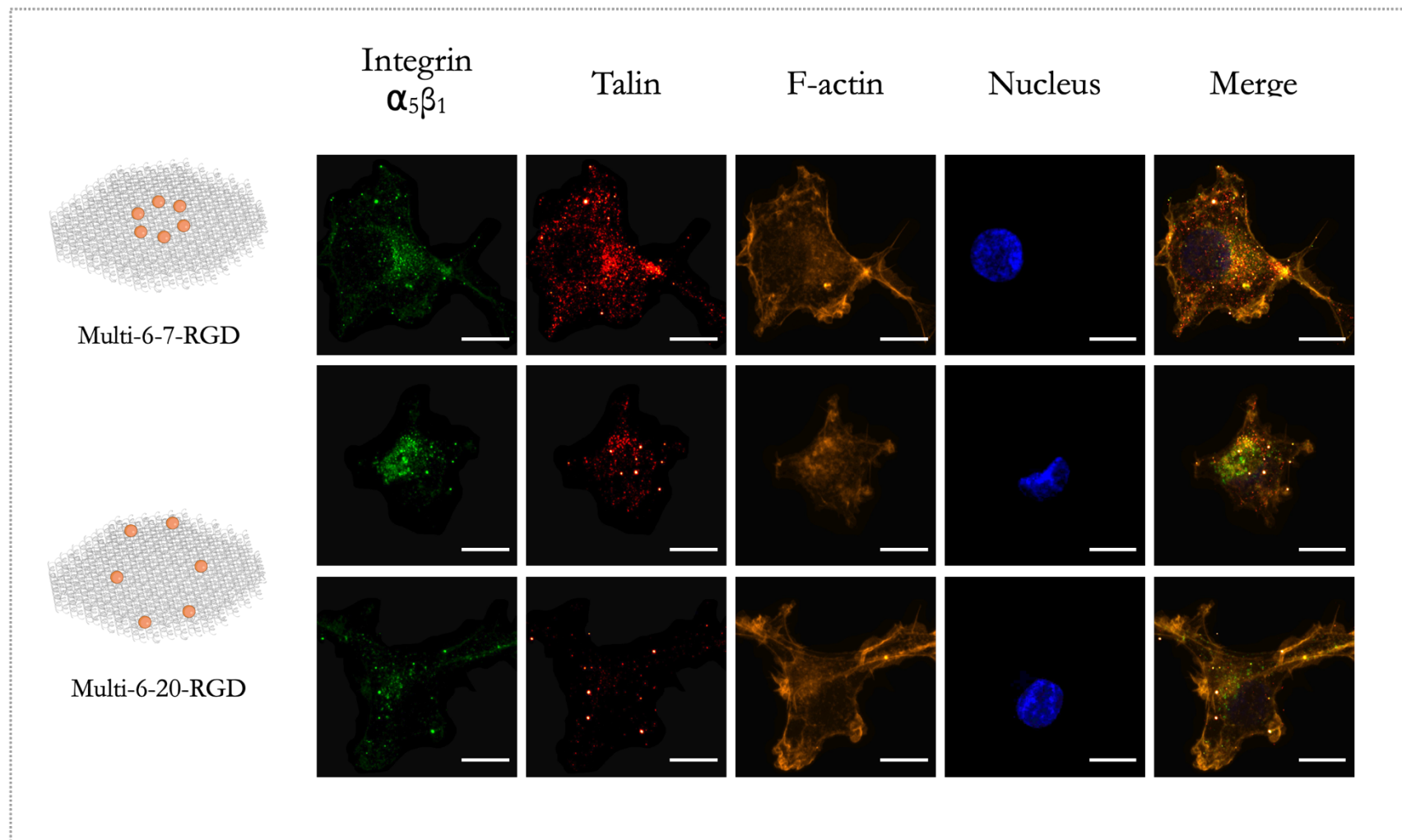


Figure 4.6 Adhesion marker (integrin  $\alpha_5\beta_1$ , talin, f-actin, nucleus) staining of HUVECs adhering to Multi-6-7-RGD and Multi-6-20-RGD. Scale bar: 10 $\mu\text{m}$ .



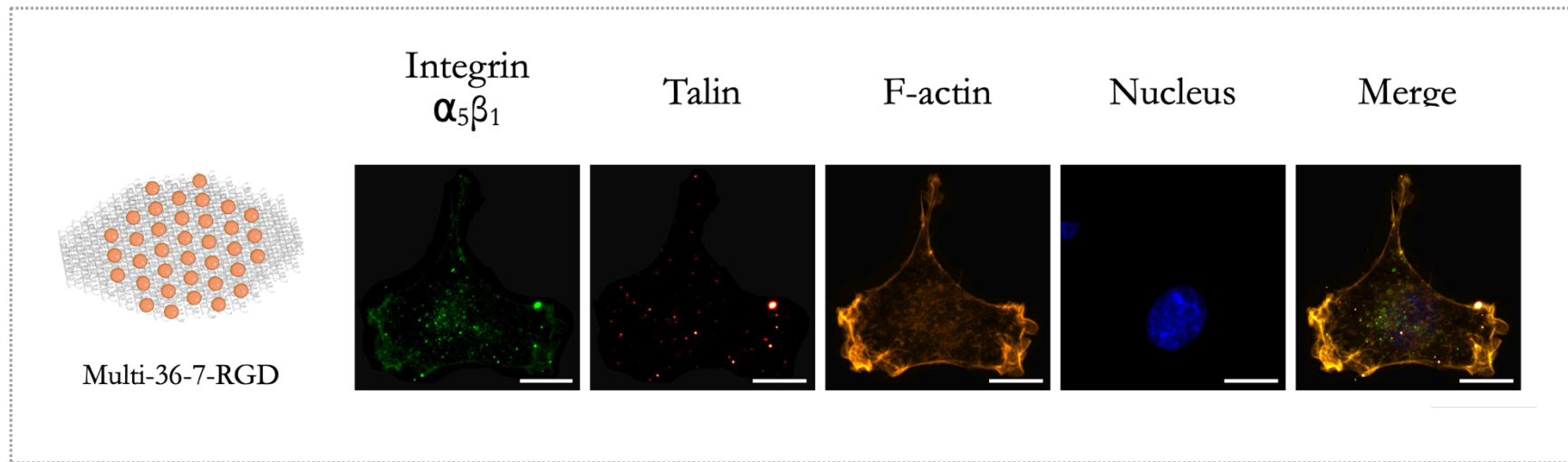


Figure 4.7 Adhesion marker (integrin  $\alpha_5\beta_1$ , talin, f-actin, nucleus) staining of HUVECs adhering to Multi-36-7-RGD. Scale bar: 10 $\mu$ m.

Markers	Talin Clusters (Size, Intensity, Density)	F-actin Actin (Phenotype/Localisation)	Integrin $\alpha 51$			Nucleus	
			Cluster Type	Clusters (Size, Intensity, Density)	Localisation		Colocalisation (Talin+F-actin)
Mono-RGD	-	Smooth +/-	n.a.	-	n.a.	-	Irregular
	-	Peripheral ruffles ++		-	n.a.	-	
	-			-	n.a.		
Multi-3-7-RGD	++	Smooth +	I	-	Interior +	+	Irregular
	++	Interior ++, Peripheral ruffles +/-		+/-	Interior +/-	+	
	+++			+/-	Periphery +/-		
Multi-3-25-RGD	+/-	Smooth ++	II	+	Interior+	+/-	Regular
	+/-	Peripheral ruffles +/-		+/-	Periphery+/-	+/-	
	-			+			
Multi-6-7-RGD	++	Smooth ++	I	+	Interior +	+	Regular
	+	Peripheral ruffles +/-		+/-	Periphery +/-	+	
	++			-			
Multi-6-20-RGD	varied	Smooth ++	I/II	varied	Interior +++	++	Regular
	varied	Interior (diffuse) ++, Periphery +		varied	Periphery +	++	
	varied			varied			
Multi-36-7-RGD	+/-	Smooth +	II	+/-	Interior++	+/-	Regular
	+/-	Peripheral ruffles ++		+	Periphery+	+/-	
	-			-			

Table 1 Analysis of adhesion markers of HUVECs adhering to RGD-liganded Multivalent Scaffolds

Analysis of adhesion marker staining on HUVECs adhering to the respective RGD liganded Multivalent Scaffolds are detailed in Table 1. Integrin  $\alpha_5\beta_1$  expression in extended, high-affinity conformations was marked in all conditions except Mono-RGD. This is likely due to the insufficient local density of RGD ligands within a 60nm radius in driving integrin  $\alpha_5\beta_1$  clustering.<sup>2,15</sup> The adhesion of the HUVECs in these conditions are likely aspecific to the charged, hydrophilic surface of the Mono-RGD.<sup>50</sup>

Integrin  $\alpha_5\beta_1$  in extended conformations colocalises with talin-1 to varying degrees in all RGD-liganded geometries besides Multivalent Scaffold-1-RGD with different cluster distributions in Figure 4.5 to Figure 4.7. Broadly, the HUVECs adhering to RGD-liganded Multivalent Scaffolds above valency 1 exhibit two distinct types of integrin  $\alpha_5\beta_1$  extended conformation-talin cluster formation, apparent in the talin and integrin channels, Figure 4.8; Type I : polarised large clusters of integrin  $\alpha_5\beta_1$  in extended conformation-talin clusters with varying degrees of colocalisation and Type II : smaller, more homogeneous distributed clusters of talin mirroring localisation trends of integrin  $\alpha_5\beta_1$  extended conformation cluster distributions but not integrin  $\alpha_5\beta_1$  extended conformation cluster density nor intensity.

We hypothesise that the distinction in the two types of integrin  $\alpha_5\beta_1$  extended conformation-talin clusters in Figure 4.5 to Figure 4.7 arises from competing integrin receptor clusters between neighbouring RGD-liganded Multivalent Scaffold in Type II cluster distributions. Type II cluster formation reflects that observed in global random ligand presentation.<sup>46</sup> In Type I clusters, the asymmetric accumulation of integrin  $\alpha_5\beta_1$  in extended conformations-talin clusters is likely from intra RGD-ligand integrin binding coupled with local distribution of RGD-liganded Multivalent Scaffold distribution (local disorder). Briefly, it has been posited in simulations in parallel settings, that the intra RGD-liganded Multivalent Scaffold geometry could be obscured in Type II clusters by ligand clusters of inter RGD-liganded Multivalent Scaffolds, resulting in a general reduction in bound integrins.<sup>29</sup> Experimental findings of force loading of integrins at different spacings

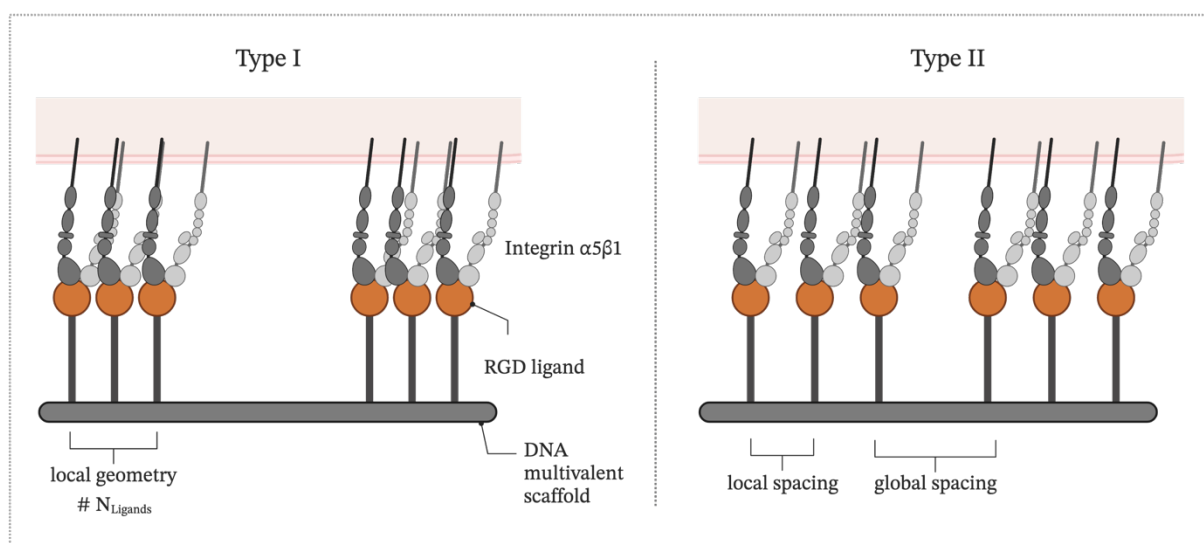


Figure 4.8 Depiction of adhesion cluster formation upon integrin  $\alpha_5\beta_1$  receptor binding to different local ligand geometries and global spacings.

exhibited the advantages of local disorder on adhesion formation.<sup>2</sup> The asymmetric accumulation of FAs in Type I clusters is accompanied by a local increase in concentration of F-actin, could be due to corresponding to increase in tension exerted locally polarising adhesion cluster formation.<sup>2,10</sup> The Type I pattern of integrin  $\alpha_5\beta_1$  extended conformation-talin clustering also indicates that co-clusters of ligand-bound and ligand free integrin  $\alpha_5\beta_1$  amplify cell response to low ligand densities.<sup>19,51,52</sup> Otherwise, integrin  $\alpha_5\beta_1$  in extended conformations and talin clusters (apart Mono-RGD) that co-localise centrally in the periphery of the nucleus observed predominantly in Type 1 clusters, likely reside in more mature adhesions, fibrillar, although lacking streak-like morphology.<sup>53</sup> This observation was made after 1h of HUVEC adhesion to rigid substrates, where after 6h, their findings suggested the translocation of the integrin  $\alpha_5\beta_1$  to enlarged focal adhesions in the ventral region of the cell.<sup>54</sup>

In general, our findings are within agreement of a universal length scale for integrin clustering between 58-73nm, albeit likely being on the lower end for HUVECs.<sup>16</sup> We ruled out the possibility of a mis-match in integrin  $\alpha_5\beta_1$  receptor adhesion site spacing within a cluster with RGD-liganded presentation, previously observed to reduce binding<sup>55</sup> in the cases where Type II clusters were formed as the trend was observed in Multi-36-7-RGD scaffolds where ligand availability was ample for binding and that ligands were spaced at 7nm previously shown to bind to clustered integrin  $\alpha_5\beta_1$ , in 3.2.11.

The HUVECs seeded on RGD-liganded Multivalent Scaffolds, in Figure 4.5 to Figure 4.7 display cell morphologies void of pronounced filopodia, instead exhibiting regions of cytoplasmic ruffle-like protrusions dense in cortical actin.<sup>56</sup> These ruffle protrusions are usually found at the leading edge of motile cells and in the absence of cell junctions.<sup>57</sup> Here, the ruffle distribution also suggests the absence of directional migration as expected from the absence of factors inducing chemotaxis, haptotaxis (globally) or mechanotaxis that would drive directional migration.<sup>56</sup> The seemingly random protrusions of the F-actin network is likely triggered by both ligand clusters on the RGD-liganded Multivalent Scaffolds and local nanotopography of the immobilised discs. Nanotopography has also been reported to alter membrane curvature and promote endocytosis,<sup>58,59</sup> reviewed by Luo et al.<sup>60</sup>

Endothelial actin filaments mediate a number of processes ranging from endo- and exocytosis, cell shape, polarity, cell-substrate, migration and cell-cell adhesion.<sup>57</sup> In our findings, the absence of stress fibres, i.e. perinuclear, dorsal and ventral<sup>61-63</sup> besides the circumferential rim could be attributed to the RGD-liganded Multivalent Scaffold substrate being less rigid than cell culture substrates, the lack of shear stress under flow in our experimental conditions,<sup>61,64,65</sup> focal adhesion anchored F-actin having lower incidence in venous endothelia or vasculatures of the umbilical cord (HUVEC),<sup>66</sup> serum-starvation,<sup>67</sup> the absence of cell-cell junctions<sup>57,68,69</sup> and actin reorganization to stress fibres being a hallmark of endothelial response to inflammation, i.e. the HUVECs in our experiments being in resting conditions.<sup>57,63</sup> For instance, stress fibres were observed as a response to inflammation in HUVECs seeded on FN that is deposited in remodelling the subendothelial basement membrane in lesion development<sup>57,70</sup> and in studies with subconfluent and confluent HUVEC populations.<sup>57,71,72</sup> Given the high density of F-actin in Type I integrin  $\alpha_5\beta_1$  extended conformation-talin clusters, nucleation of actin polymerisation likely takes place in the

region, providing sites for fibre elongation just at a slower rate as has been reported for non-filopodia presenting HUVECs<sup>63,73</sup> or upon cell junction formation.

F-actin staining of HUVECs on different RGD-liganded Multivalent Scaffolds in Figure 4.5 to Figure 4.7 exhibit structures associated with migration at the cell periphery as observed on osteoblast behaviour on substrates with nanotopography, i.e. ruffles.<sup>49</sup> In this study, cells were shown to have increased migratory behaviour in random directions on nanostructured surfaces (ranging 250nm upwards) compared to flat substrates with larger nanotopographies leading to decrease in cell migration. On the other hand, endothelial filopodia, in addition to being sites of ECM attachment, is a prominent feature in motile cells<sup>74</sup>, was observed to not be in abundance in our dataset. We attribute this to our single-cell analysis where intracellular junctions are not present and PECAM-1, one of the regulators of filopodia extension being enriched at intercellular junctions<sup>74</sup> and filopodia -type and lamellipodia-type morphologies being more abundant in fibroblasts, keratinocytes, and subtype of endothelial cells, i.e endothelial tip cells versus venous cells.<sup>73,75</sup> It should be noted that the absence of filopodia in HUVECs does not impair migration, albeit decreasing the speed at which endothelial cells migrate.<sup>73</sup>

Actin reservoirs in the middle of HUVECs observed in Multi-3-7-RGD and Multi-6-LH-RGD have been occasionally observed in migrating cells in response to substrate topography in the absence of cell adhesive ligands.<sup>76</sup> The accumulation of actin in the centre of the HUVECs is likely due to endocytic mechanisms for the internalisation of integrins amongst other proteins, known to be triggered upon cell adhesion to the ECM.<sup>77-79</sup> The endocytosis of integrins  $\alpha_5\beta_1$  in active conformations has been observed in fibrillar adhesion,<sup>36</sup> where integrin  $\alpha_5\beta_1$  localisation would be an indication of adhesion maturity and cell polarisation.<sup>80</sup>

Of note, HUVECs analysed in our dataset also showed a deviation in cell morphology from the typical “cobblestone” morphology showing a more fibroblastic/mesenchymal morphology as observed prior when sparsely populated.<sup>68</sup> Nuclear shape is known to be influenced by the actin cytoskeleton, acting as springs that prevent nuclear deformation from external forces.<sup>47</sup> As shown in 3T3 cells, disruptions or reductions of the actin cytoskeleton led to losses in nucleus circularity and an increase in the magnitude of nuclear deformation.<sup>47</sup> This is posited as the reason for nuclear deformations observed on HUVECs with greater actin cytoskeleton network angularity, lower overall F-actin volume and lower cell circularity in HUVECs adhered on Mono-RGD and Multivalent-3-7-RGD Scaffolds. Here, the inability for the actin cytoskeleton to modulate stress undergone by the nucleus can be traced back to insufficient integrin  $\alpha_5\beta_1$  engagement, in triggering talin colocalisation and stable adhesion formation.

#### 4.4 Conclusions

Endothelial cell integrins are polarised in distribution when engaging the ECM.<sup>65,81</sup> As such, the spatial and geometric patterning of ECM ligands, here RGD, have the capacity to modulate HUVEC substrate adhesive behaviour. We established that within the boundaries of our

experiments, inter-ligand geometries spaced above a minimum 35nm between geometries induced polarised adhesion formation, in good agreement with inter-adhesion cluster spacings reported.<sup>8</sup> Ligand patterning on Multivalent Scaffolds ranging from the centre of the scaffold, extending to the periphery induce polarised adhesion cluster formation in a cell subpopulations whilst pseudo regular integrin ligand presentation (<35nm in local and global spacings), Figure 4.9 resulted in more homogeneous adhesion cluster distribution.

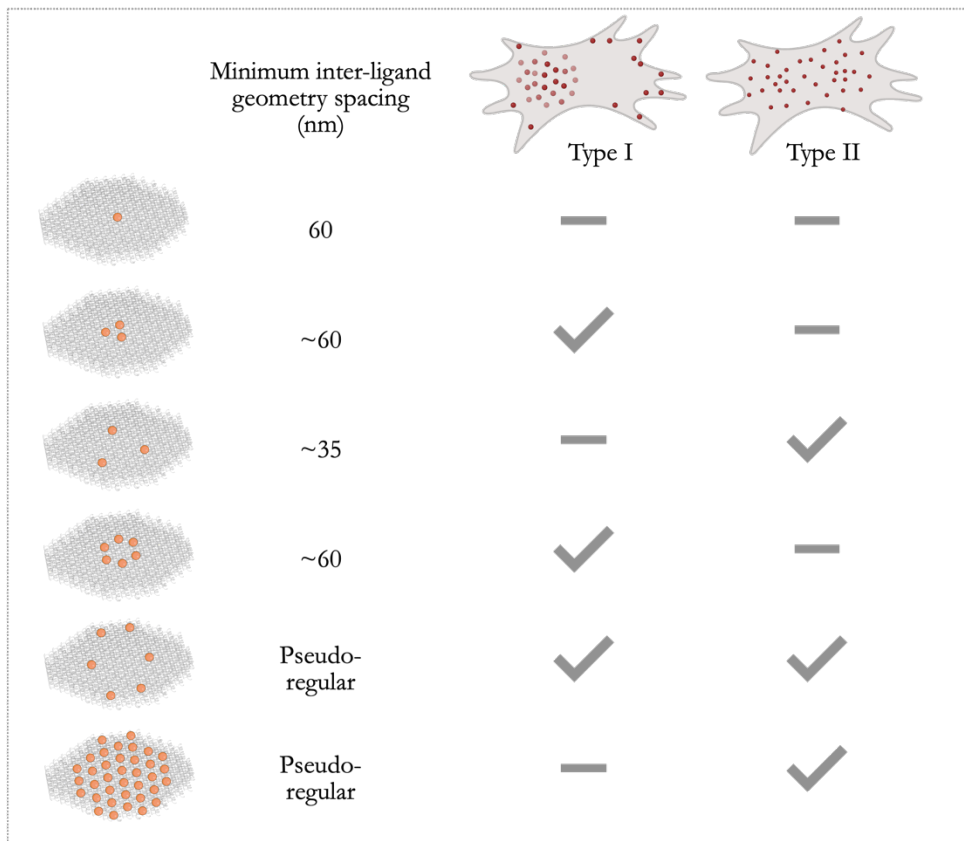


Figure 4.9 Calculated minimum inter-ligand geometry spacings for the respective Multivalent Scaffolds. Observation of Type I or Type II cluster formation on HUVECs adhering to RGD-liganded Multivalent Scaffolds.

Hence, we categorise two types of adhesion cluster formed on HUVECs into Type I being the formation of large adhesion clusters that are polarised on HUVECs. Type II adhesion clusters were instead smaller homogeneous clusters more regularly spaced out on HUVECs.

The deviation from Type I to Type II cluster formation is explained through the masking of intra- with inter-Multivalent Scaffold RGD ligand geometries. Within the boundaries of the current experimental setup, stronger adhesion derived from larger, more polarised adhesion clusters Type I arises from RGD-ligand scaffold presentation where (1) there is sufficient RGD ligands on the Multivalent Scaffold and (2) intra-Multivalent Scaffold RGD ligand geometry is not “diluted” by inter-Multivalent Scaffold RGD ligand geometry and density in scaffold packing.

In agreement with a previous study on cell spreading,<sup>15</sup> HUVECs on Mono-RGD were unable to induce integrin  $\alpha_5\beta_1$  receptor clustering, nor trigger talin recruitment. HUVECs on Multi-3-7-RGD

and Multi-6-SH-RGD Scaffolds exhibited adhesion clusters, albeit with irregular nuclei as observed in Multi-3-7RGD. The two types of adhesion clusters observed in HUVECs on Multi-6-SH-RGD and Multi-6-LH-RGD is attributed to random adsorption of the Scaffolds to the surface resulting in HUVEC adhesion cluster Type I response to intra-RGD ligand geometries and Type II response to competing inter- and intra- RGD ligand geometries. In regions where the RGD-ligand geometries are sufficiently spaced out, the intra RGD ligand geometry likely trumps leading to adhesion cluster formation Type I. In regions where the RGD-liganded Multivalent Scaffolds are in close contact, bridging adhesions it is likely that a quasi-global ligand density response will be observed, with no noticeable influence of ligand valency on cell adhesion. Neighbouring adhesions will in this case compete in sequestering available integrins in the vicinity leading to an overall reduction in bound integrins within an adhesion cluster as the density of integrins in the vicinity is decreased.<sup>2,29</sup> Put together, our findings build upon previous reports on minimal matrix adhesion units<sup>15,16,20</sup> considering the boundaries between global and local ligand geometries in inciting adhesion clusters on HUVECs in cluster formation.

## 4.5 Appendix

### 4.5.1 ssDNA Multivalent Scaffold strands and modifications

The scaffold and staple sequences are identical to that reported in a recent publication,<sup>23</sup> with the exception of substitutions for ligand presentation detailed as follows.

### 4.5.2 Ligand Face strands (Top)

DO36 strands were identical to that described in 3.7.2.

Sequence Name	Sequence	Particle for which strand was substituted
42[160]68[149]	TTATTACATACCACGGAACGCTAAACGTTTCCTCTAC CACCTACATCAC	DO3-25
50[118]76[108]	GCATAACAGGACTAGCCTTGATCCTTAGTTCCTCTAC CACCTACATCAC	DO1, DO3-7, DO3-25
51[88]78[87]	ATTACCATAGGGAAAAACATTTCTTTCCTCTACCACC TACATCAC	DO6-SH
56[97]82[87]	AGGCAGGACCAGAAAGAGCGGTCGGCCATTTCCTCTA CCACCTACATCAC	DO6-LH
33[130]62[129]	CATGCTGAATGGCTTAATTGAGTTACGCAAGACATT ATTTCTCTACCACCTACATCAC	DO6-LH
45[109]72[108]	AGGGTAATGATTAGGAGCTCCAGCTTCCTCTACCACC TACATCAC	DO3-7, DO6- SH

54[118]80[107]	AATCACCCGGTCATGGGAAACATCGGCCITTCCTCTAC CACCTACATCAC	DO6-SH
48[97]74[87]	ATAAGTTCGCAATAGGTGAGGAGTTGGCTTCCTCTA CCACCTACATCAC	DO3-7, DO6-SH
52[139]78[128]	TTTGCTAACGTTGATATCCGCACAGGGCTTCCTCTAC CACCTACATCAC	DO6-SH
36[97]62[87]	AGGCATTATTCTTAACCTCCGAATAAAGTTCCTCTAC CACCTACATCAC	DO6-LH
48[139]74[128]	TAAAGGTACTCCTTGTGGTTGTGCAAGGTTTCCTCTAC CACCTACATCAC	DO6-SH
46[160]72[149]	TTGTGTCCCAACTTCTATTACGGCAAAGTTCCTCTAC CACCTACATCAC	DO6-LH
56[139]82[128]	TCAGAACGGGATAGAGAGTTGAGGGTGGTTCCTCT ACCACCTACATCAC	DO6-LH
40[97]66[87]	TAGAAACGTCCTGAAATCATACTTTTTTTTCCTCTACC ACCTACATCAC	DO3-25

## 4.6 Bibliography

1. Di Russo, J. et al. Integrin  $\alpha 5\beta 1$  nano-presentation regulates collective keratinocyte migration independent of substrate rigidity. *eLife* 10, e69861 (2021).
2. Oria, R. et al. Force loading explains spatial sensing of ligands by cells. *Nature* 552, 219-+ (2017).
3. Saux, G. L., Magenau, A., Böcking, T., Gaus, K. & Gooding, J. J. The Relative Importance of Topography and RGD Ligand Density for Endothelial Cell Adhesion. *PLOS ONE* 6, e21869 (2011).
4. Maynard, S. A. et al. Nanoscale Molecular Quantification of Stem Cell–Hydrogel Interactions. *ACS Nano* 14, 17321–17332 (2020).
5. Vogel, V. MECHANOTRANSDUCTION INVOLVING MULTIMODULAR PROTEINS: Converting Force into Biochemical Signals. *Annual Review of Biophysics and Biomolecular Structure* 35, 459–488 (2006).
6. Vogel, V. & Sheetz, M. Local force and geometry sensing regulate cell functions. *Nat Rev Mol Cell Biol* 7, 265–275 (2006).
7. Carreiras, F. et al. Involvement of  $\alpha v\beta 3$  integrin and disruption of endothelial fibronectin network during the adhesion of the human ovarian adenocarcinoma cell line IGROV1 on the human umbilical vein cell extracellular matrix. *International Journal of Cancer* 99, 800–808 (2002).
8. Schlichthaerle, T., Lindner, C. & Jungmann, R. Super-resolved visualization of single DNA-based tension sensors in cell adhesion. *Nat Commun* 12, 2510 (2021).
9. Massia, S. P. & Hubbell, J. A. An RGD Spacing of 440 nm Is Sufficient for Integrin  $\alpha v\beta 3$ -Mediated Fibroblast Spreading and 140 nm for Focal Contact and Stress Fiber Formation. *The Journal of Cell Biology* 114, 1089–1100 (1991).
10. Chen, C. S., Alonso, J. L., Ostuni, E., Whitesides, G. M. & Ingber, D. E. Cell shape provides global control of focal adhesion assembly. *Biochemical and Biophysical Research Communications* 307, 355–361 (2003).
11. Changede, R., Cai, H., Wind, S. & Sheetz, M. P. Ligand Geometry Controls Adhesion formation via Integrin Clustering. 435826 (2018).
12. Hynes, R. O. Integrins: Bidirectional, Allosteric Signaling Machines. *Cell* 110, 673–687 (2002).
13. Winograd-Katz, S. E., Fässler, R., Geiger, B. & Legate, K. R. The integrin adhesome: from genes and proteins to human disease. *Nat Rev Mol Cell Biol* 15, 273–288 (2014).
14. Vicente-Manzanares, M. & Sánchez-Madrid, F. Targeting the integrin interactome in human disease. *Current Opinion in Cell Biology* 55, 17–23 (2018).
15. Schwartzman, M. et al. Nanolithographic Control of the Spatial Organization of Cellular Adhesion Receptors at the Single-Molecule Level. *Nano Lett.* 11, 1306–1312 (2011).
16. Arnold, M. et al. Activation of Integrin Function by Nanopatterned Adhesive Interfaces. *ChemPhysChem* 5, 383–388 (2004).



17. Arnold, M. et al. Cell interactions with hierarchically structured nano-patterned adhesive surfaces. *Soft Matter* 5, 72–77 (2009).
18. Cavalcanti-Adam, E. A., Aydin, D., Hirschfeld-Warneken, V. C. & Spatz, J. P. Cell adhesion and response to synthetic nanopatterned environments by steering receptor clustering and spatial location. *HFSP Journal* 2, 276–285 (2008).
19. Changede, R., Cai, H., Wind, S. J. & Sheetz, M. P. Integrin nanoclusters can bridge thin matrix fibres to form cell–matrix adhesions. *Nature Materials* 18, 1366–1375 (2019).
20. Young, J. L. et al. Integrin Subtypes and Nanoscale Ligand Presentation Influence Drug Sensitivity in Cancer Cells. *Nano Lett.* 20, 1183–1191 (2020).
21. Schaufler, V. et al. Selective binding and lateral clustering of  $\alpha 5 \beta 1$  and  $\alpha v \beta 3$  integrins: Unraveling the spatial requirements for cell spreading and focal adhesion assembly. *Cell Adh. Migr.* 10, 505–515 (2016).
22. Hawkes, W. et al. Probing the nanoscale organisation and multivalency of cell surface receptors: DNA origami nanoarrays for cellular studies with single-molecule control. *Faraday Discuss.* 219, 203–219 (2019).
23. Eklund, A. S., Comberlato, A., Parish, I. A., Jungmann, R. & Bastings, M. M. C. Quantification of Strand Accessibility in Biostable DNA Origami with Single-Staple Resolution. *ACS Nano* (2021).
24. Bastings, M. M. et al. From phage display to dendrimer display: Insights into multivalent binding. *Journal of the American Chemical Society* 133, 6636–6641 (2011).
25. Strauss, S. et al. Modified aptamers enable quantitative sub-10-nm cellular DNA-PAINT imaging. *Nat Methods* 15, 685–688 (2018).
26. Clark, R. A., Folkvord, J. M. & Nielsen, L. D. Either exogenous or endogenous fibronectin can promote adherence of human endothelial cells. *J Cell Sci* 82, 263–280 (1986).
27. Massia, S. P. & Hubbell, J. A. Vascular endothelial cell adhesion and spreading promoted by the peptide REDV of the IICS region of plasma fibronectin is mediated by integrin  $\alpha 4 \beta 1$ . *J Biol Chem* 267, 14019–14026 (1992).
28. Talbot, J., Tarjus, G., Van Tassel, P. R. & Viot, P. From car parking to protein adsorption: an overview of sequential adsorption processes. *Colloids and Surfaces A: Physicochemical and Engineering Aspects* 165, 287–324 (2000).
29. Comisar, W. A., Mooney, D. J. & Linderman, J. J. Integrin Organization: Linking Adhesion Ligand Nanopatterns with Altered Cell Responses. *J Theor Biol* 274, 120–130 (2011).
30. Legerstee, K. & Houtsmuller, A. B. A Layered View on Focal Adhesions. *Biology* 10, 1189 (2021).
31. Gough, R. E. & Goult, B. T. The tale of two talins – two isoforms to fine-tune integrin signalling. *FEBS Letters* 592, 2108–2125 (2018).
32. Calderwood, D. A., Campbell, I. D. & Critchley, D. R. Talins and kindlins: partners in integrin-mediated adhesion. *Nat Rev Mol Cell Biol* 14, 503–517 (2013).
33. Romero, S., Le Clainche, C. & Gautreau, A. M. Actin polymerization downstream of integrins: signaling pathways and mechanotransduction. *Biochemical Journal* 477, 1–21 (2020).
34. Henning Stumpf, B., Ambriović-Ristov, A., Radenovic, A. & Smith, A.-S. Recent Advances and Prospects in the Research of Nascent Adhesions. *Frontiers in Physiology* 11, (2020).
35. Su, Y. et al. Relating conformation to function in integrin  $\alpha 5 \beta 1$ . *Proc. Natl. Acad. Sci. U.S.A.* 113, E3872–3881 (2016).
36. Clark, K. et al. A specific  $\alpha 5 \beta 1$ -integrin conformation promotes directional integrin translocation and fibronectin matrix formation. *Journal of Cell Science* 118, 291–300 (2005).
37. Cai, W.-J. et al. Activation of the integrins  $\alpha 5 \beta 1$  and  $\alpha v \beta 3$  and focal adhesion kinase (FAK) during arteriogenesis. *Mol Cell Biochem* 322, 161–169 (2009).
38. Kapp, T. G. et al. A Comprehensive Evaluation of the Activity and Selectivity Profile of Ligands for RGD-binding Integrins. *Sci Rep* 7, 39805 (2017).
39. Alghisi, G. C., Ponsonnet, L. & Rüegg, C. The Integrin Antagonist Cilengitide Activates  $\alpha v \beta 3$ , Disrupts VE-Cadherin Localization at Cell Junctions and Enhances Permeability in Endothelial Cells. *PLoS One* 4, e4449 (2009).
40. Diaz, C., Neubauer, S., Rechenmacher, F., Kessler, H. & Missirlis, D. Recruitment of  $\alpha v \beta 3$  integrin to  $\alpha 5 \beta 1$  integrin-induced clusters enables focal adhesion maturation and cell spreading. *J Cell Sci* 133, (2020).
41. Ilić, D. et al. FAK promotes organization of fibronectin matrix and fibrillar adhesions. *Journal of Cell Science* 117, 177–187 (2004).
42. Sun, Z., Costell, M. & Fässler, R. Integrin activation by talin, kindlin and mechanical forces. *Nat Cell Biol* 21, 25–31 (2019).
43. Monkley, S. J. et al. Endothelial cell talin1 is essential for embryonic angiogenesis. *Developmental Biology* 349, 494–502 (2011).
44. Belin, B. J., Goins, L. M. & Mullins, R. D. Comparative analysis of tools for live cell imaging of actin network architecture. *BioArchitecture* 4, 189–202 (2014).

45. Tafazzoli-Shadpour, M., Mohammadi, E. & Torkashvand, E. Chapter Six - Mechanics of actin filaments in cancer onset and progress. in *International Review of Cell and Molecular Biology* (eds. Thomas, C. & Galluzzi, L.) vol. 355 205–243 (Academic Press, 2020).
46. F, K., Aj, O., Gg, Q. & De, H. Integrin Clustering Matters: A Review of Biomaterials Functionalized with Multivalent Integrin-Binding Ligands to Improve Cell Adhesion, Migration, Differentiation, Angiogenesis, and Biomedical Device Integration. *Adv Healthc Mater* 7, e1701324–e1701324 (2018).
47. Haase, K. et al. Extracellular Forces Cause the Nucleus to Deform in a Highly Controlled Anisotropic Manner. *Sci Rep* 6, 21300 (2016).
48. Pennacchio, F. A., Nastaly, P., Poli, A. & Maiuri, P. Tailoring Cellular Function: The Contribution of the Nucleus in Mechanotransduction. *Frontiers in Bioengineering and Biotechnology* 8, (2021).
49. Cheng, Y., Zhu, S. & Pang, S. W. Directing Cell Migration with Patterned Nanostructures. in *2021 IEEE 34th International Conference on Micro Electro Mechanical Systems (MEMS)* 579–582 (2021).
50. Wilson, C. J., Clegg, R. E., Leavesley, D. I. & Percy, M. J. Mediation of Biomaterial–Cell Interactions by Adsorbed Proteins: A Review. *Tissue Engineering* 11, 1–18 (2005).
51. Bray, D., Levin, M. D. & Morton-Firth, C. J. Receptor clustering as a cellular mechanism to control sensitivity. *Nature* 393, 85–88 (1998).
52. Chang, A. C. et al. Single Molecule Force Measurements in Living Cells Reveal a Minimally Tensioned Integrin State. *ACS Nano* 10, 10745–10752 (2016).
53. Pankov, R. et al. Integrin Dynamics and Matrix Assembly: Tensin-Dependent Translocation of  $\alpha 5\beta 1$  Integrins Promotes Early Fibronectin Fibrillogenesis. *Journal of Cell Biology* 148, 1075–1090 (2000).
54. Kawakami, K., Tatsumi, H. & Sokabe, M. Dynamics of integrin clustering at focal contacts of endothelial cells studied by multimode imaging microscopy. *Journal of Cell Science* 114, 3125–3135 (2001).
55. Bae, G. et al. Receptor-Level Proximity and Fastening of Ligands Modulates Stem Cell Differentiation. *Advanced Functional Materials*, 2200828 (2022).
56. Lamalice, L., Le Boeuf, F. & Huot, J. Endothelial Cell Migration During Angiogenesis. *Circulation Research* 100, 782–794 (2007).
57. Schnittler, H. et al. Actin filament dynamics and endothelial cell junctions: the Ying and Yang between stabilization and motion. *Cell Tissue Res* 355, 529–543 (2014).
58. Zhao, W. et al. Nanoscale manipulation of membrane curvature for probing endocytosis in live cells. *Nat Nanotechnol* 12, 750–756 (2017).
59. Galic, M. et al. External push and internal pull forces recruit curvature-sensing N-BAR domain proteins to the plasma membrane. *Nat Cell Biol* 14, 874–881 (2012).
60. Luo, J. et al. The influence of nanotopography on cell behaviour through interactions with the extracellular matrix – A review. *Bioactive Materials* 15, 145–159 (2022).
61. Lehtimäki, J. I., Rajakylä, E. K., Tojkander, S. & Lappalainen, P. Generation of stress fibers through myosin-driven reorganization of the actin cortex. *eLife* 10, e60710 (2021).
62. Maninová, M. & Vomastek, T. Dorsal stress fibers, transverse actin arcs, and perinuclear actin fibers form an interconnected network that induces nuclear movement in polarizing fibroblasts. *The FEBS Journal* 283, 3676–3693 (2016).
63. Prasain, N. & Stevens, T. The actin cytoskeleton in endothelial cell phenotypes. *Microvasc Res* 77, 53–63 (2009).
64. Katoh, K., Kano, Y. & Ookawara, S. Role of stress fibers and focal adhesions as a mediator for mechano-signal transduction in endothelial cells in situ. *Vasc Health Risk Manag* 4, 1273–1282 (2008).
65. Wolpe, A. G., Ruddiman, C. A., Hall, P. J. & Isakson, B. E. Polarized Proteins in Endothelium and Their Contribution to Function. *JVR* 58, 65–91 (2021).
66. van Geemen, D. et al. F-Actin–Anchored Focal Adhesions Distinguish Endothelial Phenotypes of Human Arteries and Veins. *Arteriosclerosis, Thrombosis, and Vascular Biology* 34, 2059–2067 (2014).
67. Gallant, N. D., Michael, K. E. & García, A. J. Cell Adhesion Strengthening: Contributions of Adhesive Area, Integrin Binding, and Focal Adhesion Assembly. *MBoC* 16, 4329–4340 (2005).
68. Dejana, E. Endothelial cell–cell junctions: happy together. *Nat Rev Mol Cell Biol* 5, 261–270 (2004).
69. Taha, A. A., Taha, M., Seebach, J. & Schnittler, H.-J. ARP2/3-mediated junction-associated lamellipodia control VE-cadherin–based cell junction dynamics and maintain monolayer integrity. *MBoC* 25, 245–256 (2014).
70. Al-Yafeai, Z. et al. Endothelial Fibronectin Deposition by  $\alpha 5\beta 1$  Integrins Drives Atherogenic Inflammation. *Arterioscler Thromb Vasc Biol* 38, 2601–2614 (2018).
71. Angiogenin Enhances Cell Migration by Regulating Stress Fiber Assembly and Focal Adhesion Dynamics. *PLOS ONE* 6, e28797 (2011).
72. Porcù, E. et al. The Novel Antitubulin Agent TR-764 Strongly Reduces Tumor Vasculature and Inhibits HIF-1 $\alpha$  Activation. *Sci Rep* 6, 27886 (2016).
73. Phng, L.-K., Stanchi, F. & Gerhardt, H. Filopodia are dispensable for endothelial tip cell guidance. *Development* 140, 4031–4040 (2013).
74. DeLisser, H. M. Modulators of endothelial cell filopodia. *Cell Adh Migr* 5, 37–41 (2011).

75. Gerhardt, H. et al. VEGF guides angiogenic sprouting utilizing endothelial tip cell filopodia. *J Cell Biol* 161, 1163–1177 (2003).
76. Chen, S. et al. Actin Cytoskeleton and Focal Adhesions Regulate the Biased Migration of Breast Cancer Cells on Nanoscale Asymmetric Sawteeth. *ACS Nano* 13, 1454–1468 (2019).
77. Bridgewater, R. E., Norman, J. C. & Caswell, P. T. Integrin trafficking at a glance. *J Cell Sci* 125, 3695–3701 (2012).
78. De Franceschi, N., Hamidi, H., Alanko, J., Sahgal, P. & Ivaska, J. Integrin traffic – the update. *Journal of Cell Science* 128, 839–852 (2015).
79. Lee, E. & Knecht, D. A. Visualization of actin dynamics during macropinocytosis and exocytosis. *Traffic* 3, 186–192 (2002).
80. Mana, G., Valdembri, D. & Serini, G. Conformationally active integrin endocytosis and traffic: why, where, when and how? *Biochem Soc Trans* 48, 83–93 (2020).
81. Moreno-Layseca, P., Icha, J., Hamidi, H. & Ivaska, J. Integrin trafficking in cells and tissues. *Nat Cell Biol* 21, 122–132 (2019).

# Chapter 5      Conclusions & Outlook

## 5.1 Conclusions of this Thesis

This thesis studies the influence of nano-controlled ligand presentation using DNA scaffolds on integrin  $\alpha_5\beta_1$  receptor binding and adhesion cluster formation based on integrin  $\alpha_5\beta_1$  expression levels. In integrin  $\alpha_5\beta_1$  receptor binding, components of ligand spacing and rigidity were tested on HUVEC, CHO and HeLa in activated and resting conditions, and resulting efficacies and trends in signal localisation discussed. In the study of adhesion cluster formation, we present ligand geometries of different valencies and spacings and inter-ligand geometry spacings of 60nm and below. We define the boundaries between local and global ligand presentation that result in the two types of adhesion cluster formation observed.

In Chapter 2, we developed a workflow to extract integrin  $\alpha_5\beta_1$  inter-receptor spacings by modelling experimental data on cells of different integrin  $\alpha_5\beta_1$  expression levels. We combined image processing and linked experimental data from cell binding assay and extracted theoretical distributions of integrin  $\alpha_5\beta_1$  nearest neighbour spacings. The modelled distributions of integrin  $\alpha_5\beta_1$  nearest neighbour inter-receptor distances resulted in distinct regimes of receptor clustering in the sub-60nm regime across HUVEC, CHO and HeLa cells. As the regimes were sufficiently distinct, ligand spacings for presentation on DNA scaffolds were selected to probe the distinct nanoscale spatial regimes in selective engagement of clusters of cell adhesions.

In Chapter 3, we attempt to selectively engage integrin adhesion clusters with engineered nanomaterials that display a spatially controlled ligand presentation. Here, we demonstrated the ability to modulate integrin binding efficacy with rigid ligand spatial presentation below 40nm. On activated HUVECs and HeLa, an increase in binding efficacy is observed for  $\sim 7$ nm spacings with efficacies that tapered with increased ligand spacings. Activated CHOs showed increasing efficacies with increased ligand spacings (max. 36nm). HUVECs in resting conditions did not show a preference for any spacings in the regime tested. CHO and HeLa cells however showed a deviation in staining localisation at 7nm, with the former localising in the nuclear region and cell periphery and the latter forming clusters across the cell surface. We hypothesised that in non-cancerous cells (HUVEC and CHO), binding arose from unliganded integrins co-clustering with ligated integrins.<sup>1</sup> In HeLa cells however, the unliganded clusters likely arise from integrin upregulation.<sup>2</sup> Taken together, this approach shows that spatially constrained bivalent ligand

presentation in the sub 40nm regime bind to integrin clusters with higher efficiencies than their flexible counterparts in some cell types, e.g. HUVEC and HeLa when activated.

In Chapter 4, we define regimes of local ligand geometries versus global ligand geometry spacing for selective adhesion cluster formation on randomly immobilised scaffolds of 60nm. To this extent, we detail boundaries in inducing polarised adhesion formation versus homogenous adhesion cluster distribution on HUVECs through local versus global ligand geometries. When geometries were spaced more than 35nm apart, polarised adhesion formation was observed, with cytoskeletal formation being dependent on ligand valency. When geometries were presented in spacings inferior to 35nm, homogenous distributions of smaller adhesion clusters was observed, with noticeable influence of valency. Geometries bridging the two conditions resulted in subpopulations of cells exhibiting polarised or homogeneous adhesion cluster formation.

## 5.2 Discussion and Future Directions

As integrins are known to be spatially regulated, reporting on a potential link between the spatial distribution of the integrin  $\alpha_5\beta_1$  could shed light on the mechanisms that govern integrin clustering and signalling. Probing the spatial tolerance of the integrin  $\alpha_5\beta_1$  adhesion system could weigh in on the debate<sup>3</sup> between the protumoural versus tumour suppressive role of the receptor in cancer and/or other diseases.<sup>4</sup> The resulting distribution of receptor spacings and in turn their ligands could guide the design of integrin  $\alpha_5\beta_1$  expression based therapies. The spatial distribution of the integrin  $\alpha_5\beta_1$  receptors could also be investigated in the context of 2D versus 3D cell culture matrices, providing a more clinically relevant platform for future investigations.<sup>5</sup> The distributions of integrin  $\alpha_5\beta_1$  interreceptor spacings could also enhance our understanding of force transduction within adhesions and on the cell as a whole, as well as the dynamics in the diffusion of integrins on the cell surface.<sup>6,7</sup> Endocytic pathways of spatially distinct integrin  $\alpha_5\beta_1$  adhesion could also be investigated with particles confined to the modelled spacings probing the different clusters of adhesions.<sup>8</sup>

### 5.2.1 Extension of the Bivalent Scaffold System.

The Rigid Bivalent Scaffold binding experiments and HUVEC cell response to RGD ligand geometries could be conducted with markers for the different stages of maturity to weigh in on the distribution of binding sites within different clusters of adhesions. For instance, nascent adhesions ( $<0.25\mu\text{m}$ ) composed of integrins, paxilin and talin could be distinguished from focal complexes and adhesions ( $\sim 0.5\text{-}5\mu\text{m}$ ) with additional  $\alpha$ -actinin,<sup>9</sup> focal adhesion kinase (FAK),<sup>10</sup> phospho-paxilin,<sup>10</sup> vinculin<sup>11</sup>, zyxin<sup>12</sup> and fibrillar adhesions with tensin.<sup>13-15</sup>

The Rigid Bivalent Scaffold could also be used to probe the composition and spatiotemporal distributions of integrins and/or other proteins within these adhesion through heteroligand presentation with ligands of respective receptor selectivity.<sup>16-18</sup> For instance, Amrosetti et al.

employed DNA nanoassemblies to probe Her2 membrane receptor nanodomains.<sup>19</sup> Specific binding arising from the tailoring of ligand presentation on the scaffolds could be incorporated as targeting elements in the design of precision nanomedicines.<sup>20</sup> In addition these relatively small scaffolds could be used in super-resolution imaging as probes for the nanoscale localisation of the bound receptors. Besides, higher valency Rigid Scaffolds with ligand spacings reflecting the highest regime of selectivity from the Bivalent Scaffold assays could be designed to enhance the “super-selective” behaviour of the targeting system.<sup>21</sup> Targeting elements incorporated for therapeutic applications could include spatial findings presented here.<sup>22,23</sup> Of note, recent studies on cancer cells showed a dependence on nanoscale ligand spacing,<sup>24</sup> actin cytoskeleton organisation<sup>25</sup> and drug type on survival with cancer cell adhesion being cell cycle dependent.<sup>26</sup>

### 5.2.2 Cell studies in 3D

As we now have an understanding of the factors relating to integrin  $\alpha_5\beta_1$  conformational changes,<sup>27–29</sup> with this study elaborating on the influence of ligand spacing and rigidity on cell states at rest and whence activated, follow up investigations could probe the kinetics of integrin  $\alpha_5\beta_1$  receptor binding on live cells, in concert with ligands binding to the synergy adhesion site<sup>30–32</sup> and Manganese ions for improved affinity.<sup>27</sup> A follow up study in 3D could potentially further our understanding of integrin  $\alpha_5\beta_1$  receptor engagement in artificial ECMs (aECMs)<sup>33</sup> potentially including temporal elements that could facilitate translation to clinical environments for tissue engineering applications.<sup>34</sup>

The next steps in providing a complete overview on selective cell response to sub-adhesion integrin ligand geometries would be to analyse HUVECs for longer periods of time, accounting for endogenous ECM protein deposition or in complete media change upon cell adhesion.<sup>35</sup> Modulating cell densities seeded to in investigating HUVEC response in the presence of cell-cell junctions could also shed light on the adhesion/stress fibre formation in conditions closer to or mimicking that of endothelial cells in vivo. The potential incidence or absence of stress fibre formation in response to ligand geometries could be analysed in terms of motility and endothelial function.<sup>36,37</sup>

### 5.2.3 Expanding the Multivalent Scaffold studies

In mimicking native Fibronectin (FN) engagement of integrins  $\alpha_5\beta_1$  on HUVECs, experimental methods could be adapted to include Manganese ions and integrin  $\alpha_5\beta_1$  synergy peptides incorporated onto the Multivalent Scaffold in studying adhesion and stress fibre formation.<sup>27,30</sup> As the synergy peptide binding flanks that of the RGD binding site, the individual peptides could be couples to opposing primes of complementary dsDNA handle/antihandles to a single receptor. Alternatively, in mimicking the spacing of the 9<sup>th</sup> and 10<sup>th</sup> type III domains on Fibronectin, the PHSRN synergy peptide could be spaced at 5nm from RGD.<sup>31,38</sup> Live HUVEC tracking of adhesion on liganded Multivalent Scaffolds via holotomography<sup>39</sup> could also provide insight on the motility, adhesion and presence of cell junctions on cell response to ligand presentation. Live

cell staining of the actin cytoskeleton could be incorporated in studying the dynamics of actin cytoskeleton formation as a result.<sup>40</sup> The F-actin distribution in cells could also be quantitatively analysed using a Fiji plugin developed by Zonderland et al., regardless of cell shape and taking into account F-actin localisation and thickness.<sup>41</sup> Heterogeneous ligand display could also be fine-tuned to selectively target cell response, e.g. integrins  $\alpha_v\beta_3$  for endothelial cell migration and angiogenesis<sup>42</sup> and  $\alpha_4\beta_1$  for venous endothelial adhesion and promotion of cell survival and proliferation<sup>43</sup> taking into account the nanoscale proximity in clustering/co-clustering of the respective receptors. Building on this, integrin subtype distribution and function could also be interrogated in their reportedly different localisations on the endothelium with the Multivalent Scaffold, e.g. integrins  $\alpha_2\beta_1$  and  $\alpha_5\beta_1$  found predominantly on inter-endothelial junctions and integrins.  $\alpha_5\beta_1$  and  $\alpha_v\beta_3$  being found on the abluminal endothelium. Any selective binding observed from these receptor(s) engagement could be used as therapeutic targets.<sup>43</sup> For instance, in the case of integrin  $\alpha_5\beta_1$ , fibronectin is reportedly upregulated in regions of atherosclerotic lesions and angiogenesis.<sup>44,45</sup> Nevertheless, each integrin subtype would need to be evaluated respectively as, nanospacing has been reported to influence cellular properties linked to respective subtypes.<sup>24</sup>

Otherwise, the current studies of cell response to the Multivalent Scaffolds could be expanded by mixing blank (ligand-free) scaffolds with liganded scaffolds. This would afford control over local ligand valency whilst exploring the influence of global ligand presentation on adhesion cluster formation. The impact of such ligand presentation on adhesion cluster size, turnover and cell migration will inform us on the intelligent design of future systems targeting integrin receptors. Of note, such an experimental platform could be easily adapted in the study of other ligand-receptor systems.

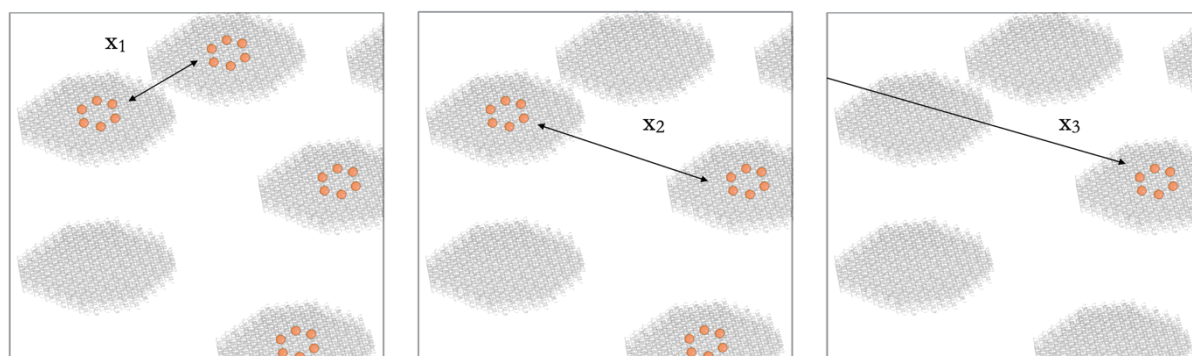


Figure 5.1 Expanding Multivalent Scaffold assays. Combining blank and liganded scaffolds for the study of adhesion type formation.

#### 5.2.4 Toward selective artificial ECMs

Incorporation of adhesion island hotspots into artificial ECMs (aECMS) could further translate our findings from 2D to 3D, allowing for assessment of the influence of aECM rigidity, extending the inter-ligand spacings probed below 30nm as previously conducted by Oria et al.,<sup>46</sup>

incorporating local adhesive hotspots by Dems et al.<sup>47</sup> In addition, we could weigh in on the optimal range of hydrogel rigidity with the rigid presentation of ligands at high local densities (in the regime of single integrin receptors) on the Multivalent Scaffold expanding the influence of ligand valency, spacing (global vs local) and density in a controlled manner in 3D. Ligand - patterned hydrogels to elicit selective responses in angiogenesis could also be designed based on the findings of HUVEC engagement to the liganded Multivalent Scaffolds.<sup>15,48</sup> Here, designing precision biomaterials with additive manufacturing accounting for boundaries in ligand presentation for the modulation of cell binding and/or adhesion could further advance the regulatory approval of these biomaterials for clinical applications.<sup>5,49</sup>

### 5.3 Bibliography

1. Changede, R., Cai, H., Wind, S. J. & Sheetz, M. P. Integrin nanoclusters can bridge thin matrix fibres to form cell–matrix adhesions. *Nature Materials* 18, 1366–1375 (2019).
2. Hou, J., Yan, D., Liu, Y., Huang, P. & Cui, H. The Roles of Integrin alpha5beta1 in Human Cancer. *OTT* 13, 13329–13344 (2020).
3. Schaffner, F., Ray, A. M. & Dontenwill, M. Integrin  $\alpha 5 \beta 1$ , the Fibronectin Receptor, as a Pertinent Therapeutic Target in Solid Tumors. *Cancers (Basel)* 5, 27–47 (2013).
4. Gilcrease, M. Z. Integrin signaling in epithelial cells. *Cancer Letters* 247, 1–25 (2007).
5. Maynard, S. A., Winter, C. W., Cunnane, E. M. & Stevens, M. M. Advancing Cell-Instructive Biomaterials Through Increased Understanding of Cell Receptor Spacing and Material Surface Functionalization. *Regen. Eng. Transl. Med.* 7, 533–547 (2021).
6. Sun, Z., Costell, M. & Fässler, R. Integrin activation by talin, kindlin and mechanical forces. *Nat Cell Biol* 21, 25–31 (2019).
7. Sun, Z., Guo, S. S. & Fässler, R. Integrin-mediated mechanotransduction. *Journal of Cell Biology* 215, 445–456 (2016).
8. Mana, G., Valdembri, D. & Serini, G. Conformationally active integrin endocytosis and traffic: why, where, when and how? *Biochem Soc Trans* 48, 83–93 (2020).
9. Ye, N. et al. Direct observation of  $\alpha$ -actinin tension and recruitment at focal adhesions during contact growth. *Exp Cell Res* 327, 57–67 (2014).
10. Pasapera, A. M., Schneider, I. C., Rericha, E., Schlaepfer, D. D. & Waterman, C. M. Myosin II activity regulates vinculin recruitment to focal adhesions through FAK-mediated paxillin phosphorylation. *Journal of Cell Biology* 188, 877–890 (2010).
11. Chen, C. S., Alonso, J. L., Ostuni, E., Whitesides, G. M. & Ingber, D. E. Cell shape provides global control of focal adhesion assembly. *Biochemical and Biophysical Research Communications* 307, 355–361 (2003).
12. Legerstee, K., Geverts, B., Slotman, J. A. & Houtsmuller, A. B. Dynamics and distribution of paxillin, vinculin, zyxin and VASP depend on focal adhesion location and orientation. *Scientific Reports* 9, 10460 (2019).
13. Gardel, M. L., Schneider, I. C., Aratyn-Schaus, Y. & Waterman, C. M. Mechanical Integration of Actin and Adhesion Dynamics in Cell Migration. *Annu Rev Cell Dev Biol* 26, 315–333 (2010).
14. Zamir, E. & Geiger, B. Molecular complexity and dynamics of cell-matrix adhesions. *Journal of Cell Science* 114, 3583–3590 (2001).
15. Moreno-Layseca, P., Icha, J., Hamidi, H. & Ivaska, J. Integrin trafficking in cells and tissues. *Nat Cell Biol* 21, 122–132 (2019).
16. Tang, Q. & Han, D. Obtaining Precise Molecular Information via DNA Nanotechnology. *Membranes* 11, 683 (2021).
17. Li, X. et al. DNA-Based Molecular Engineering of the Cell Membrane. *Membranes* 12, 111 (2022).
18. Huang, J. et al. Arranging Small Molecules with Sub-Nanometer Precision on DNA Origami Substrates for the Single-Molecule Investigation of Protein-Ligand Interactions. *Small Structures* (2020).
19. Ambrosetti, E. et al. A DNA-nanoassembly-based approach to map membrane protein nanoenvironments. *Nat. Nanotechnol.* 16, 85–95 (2021).
20. Tian, X., Angioletti-Uberti, S. & Battaglia, G. On the design of precision nanomedicines. *Science Advances* 6, eaat0919 (2020).



21. Scheepers, M. R. W., IJzendoorn, L. J. van & Prins, M. W. J. Multivalent weak interactions enhance selectivity of interparticle binding. *PNAS* (2020).
22. Singh, J. P. & Young, J. L. The cardiac nanoenvironment: form and function at the nanoscale. *Biophys Rev* 13, 625–636 (2021).
23. Wang, Z. et al. DNA nanotechnology-facilitated ligand manipulation for targeted therapeutics and diagnostics. *Journal of Controlled Release* 340, 292–307 (2021).
24. Young, J. L. et al. Integrin Subtypes and Nanoscale Ligand Presentation Influence Drug Sensitivity in Cancer Cells. *Nano Lett.* 20, 1183–1191 (2020).
25. Kubiak, A. et al. Stiffening of DU145 prostate cancer cells driven by actin filaments – microtubule crosstalk conferring resistance to microtubule-targeting drugs. *Nanoscale* 13, 6212–6226 (2021).
26. Ungai-Salánki, R. et al. Single-cell adhesion strength and contact density drops in the M phase of cancer cells. *Sci Rep* 11, 18500 (2021).
27. Schumacher, S. et al. Structural insights into integrin  $\alpha 5\beta 1$  opening by fibronectin ligand. *Science Advances* 7, eabe9716 (2021).
28. Miyazaki, N., Iwasaki, K. & Takagi, J. A systematic survey of conformational states in  $\beta 1$  and  $\beta 4$  integrins using negative-stain electron microscopy. *Journal of Cell Science* 131, jcs216754 (2018).
29. Su, Y. et al. Relating conformation to function in integrin  $\alpha 5\beta 1$ . *Proc. Natl. Acad. Sci. U.S.A.* 113, E3872-3881 (2016).
30. Kapp, T. G. et al. A Comprehensive Evaluation of the Activity and Selectivity Profile of Ligands for RGD-binding Integrins. *Sci Rep* 7, 39805 (2017).
31. Aota, S., Nomizu, M. & Yamada, K. M. The short amino acid sequence Pro-His-Ser-Arg-Asn in human fibronectin enhances cell-adhesive function. *Journal of Biological Chemistry* 269, 24756–24761 (1994).
32. Liu, Y. et al. HUVEC cell affinity evaluation and integrin-mediated mechanism study on PHSRN-modified polymer. *Colloids and Surfaces B: Biointerfaces* 84, 6–12 (2011).
33. Dhavalikar, P. et al. Review of Integrin-Targeting Biomaterials in Tissue Engineering. *Advanced Healthcare Materials* 9, 2000795 (2020).
34. Albertazzi, L. et al. Spatiotemporal control and superselectivity in supramolecular polymers using multivalency. *Proc. Natl. Acad. Sci. U.S.A.* 110, 12203–12208 (2013).
35. Gallant, N. D., Michael, K. E. & García, A. J. Cell Adhesion Strengthening: Contributions of Adhesive Area, Integrin Binding, and Focal Adhesion Assembly. *MBoC* 16, 4329–4340 (2005).
36. Dejana, E. Endothelial cell–cell junctions: happy together. *Nat Rev Mol Cell Biol* 5, 261–270 (2004).
37. Schnittler, H. et al. Actin filament dynamics and endothelial cell junctions: the Ying and Yang between stabilization and motion. *Cell Tissue Res* 355, 529–543 (2014).
38. Mardon, H. J. & Grant, K. E. The role of the ninth and tenth type III domains of human fibronectin in cell adhesion. *FEBS Letters* 340, 197–201 (1994).
39. Silva, L. M. R. et al. *Besnoitia besnoiti* infection alters both endogenous cholesterol de novo synthesis and exogenous LDL uptake in host endothelial cells. *Sci Rep* 9, 6650 (2019).
40. Belin, B. J., Goins, L. M. & Mullins, R. D. Comparative analysis of tools for live cell imaging of actin network architecture. *BioArchitecture* 4, 189–202 (2014).
41. Zonderland, J., Wieringa, P. & Moroni, L. A quantitative method to analyse F-actin distribution in cells. *MethodsX* 6, 2562–2569 (2019).
42. Kim, S., Harris, M. & Varner, J. A. Regulation of integrin  $\alpha v\beta 3$ -mediated endothelial cell migration and angiogenesis by integrin  $\alpha 5\beta 1$  and protein kinase A. *J Biol Chem* 275, 33920–33928 (2000).
43. Calzada, M. J. et al.  $\alpha 4\beta 1$  Integrin Mediates Selective Endothelial Cell Responses to Thrombospondins 1 and 2 In Vitro and Modulates Angiogenesis In Vivo. *Circulation Research* 94, 462–470 (2004).
44. Stenman, S., von Smitten, K. & Vaheri, A. Fibronectin and atherosclerosis. *Acta Med Scand Suppl* 642, 165–170 (1980).
45. Kumar, V. B. S., Viji, R. I., Kiran, M. S. & Sudhakaran, P. R. Angiogenic Response of Endothelial Cells to Fibronectin. in *Biochemical Roles of Eukaryotic Cell Surface Macromolecules* (eds. Sudhakaran, P. R. & Surolia, A.) 131–151 (Springer, 2012).
46. Oriá, R. et al. Force loading explains spatial sensing of ligands by cells. *Nature* 552, 219–+ (2017).
47. Dems, D. et al. Multivalent Clustering of Adhesion Ligands in Nanofiber-Nanoparticle Composites. *Acta Biomaterialia* 119, 303–311 (2021).
48. Giraudo, M. V. et al. Angiogenic Potential in Biological Hydrogels. *Biomedicines* 8, 436 (2020).
49. Guzzi, E. A. & Tibbitt, M. W. Additive Manufacturing of Precision Biomaterials. *Advanced Materials* 32, 1901994 (2020).

# Curriculum Vitae

Eva Eugene Kurisinkal

Lausanne 1004, Switzerland

[eva.kurisinkal@gmail.com](mailto:eva.kurisinkal@gmail.com)

## Education & Work Experience

- Ph.D in Materials Science & Bioengineering | EPFL, Switzerland | 2018 – 2022
- International Consortium Research Assistant | Optogenetrapy | ETH Zürich, Switzerland | 2017
- Double M.Sc. in Polymer Science & Sustainable Materials | Université de Strasbourg, France & Albert-Ludwigs-Universität Freiburg, Germany | 2015-2017
- Master's thesis | ETH Zürich, Switzerland | 2016-2017
- B.Sc in Physics, Mathematics & Chemistry | Université de Strasbourg & École Européenne de Chimie, Polymères et Matériaux, France | 2012-2015
- Preparation for Tertiary Education in France (DUPSEE) | Institut Universitaire de Technologie de Colmar, Centre d'Etudes des Langues de Colmar, France | 2011-2012
- Junior College in preparation for GCSE A Levels | Meridian Junior College, Singapore | 2011

## Scholarships & Awards

- Alsace Boussole Scholarship (2015-2017)
- Université Franco-Allemande/Deutsch-Französische Hochschule (2015-2017)
- PETRONAS Malaysia excellence scholarship (2011-2017)
- ASEAN Singapore excellence scholarship (2011)

## Skills

- Materials: HPLC, DNA Nanoparticle design & characterisation, AFM, NMR
- Biology: in vitro cell culture, Confocal Microscopy, Solid-Phase Binding Assays, Molecular Biology techniques, Molecular Cloning, Enzymatic Assays, Flow Cytometry, DNA Preparation, Bioconjugation, Image Processing.
- IT: Proficient in Microsoft, GraphPadPRISM, Adobe Illustrator, Fiji.
- Project Management: PRINCE2 Foundation & AgilePM Foundation certified.
- Languages: English (Native), French (Fluent, C2), German (Intermediate, B1/2), Malay (Fluent, C2).

## Outreach

- 25th Annual Meeting of the SSB+RM: Resorbable Biomaterials | Muttentz | May 2019
- International Biointerfaces Conference | Zurich | August 2018
- Swiss-Japanese Symposium on NanoBioEngineering and Medicine | Lausanne | September 2018
- EPFL/ETHZ Bioengineering Days | Lausanne | September 2018
- ECM Matrix Summer School | Zurich | September 2018

## Publications

- **Kurisinkal, E.E.**, Caroprese, V., Koga, M.M., Morzy, D., Bastings, M.M.C. Selective Integrin  $\alpha 5\beta 1$  Targeting Through Spatially Constrained Multivalent DNA-Based Nanoparticles, *Molecules*, 27(15), 4968 (2022)

- Nievergelt, A. P., Nievergelt, A.P., Kammer, C., Brillard, C., **Kurisinkal, E.E.**, Bastings, M.M.C., Karimi, A., Fantner, G.E. High-Speed Atomic Force Microscopy: Large-Range HS-AFM Imaging of DNA Self-Assembly through In Situ Data-Driven Control. *Small Methods* 3, 1970022 (2019).
- Bila, H., **Kurisinkal, E.E.** & Bastings, M.M.C. Engineering a stable future for DNA-origami as a biomaterial. *Biomater. Sci.* 7, 532–541 (2019).
- Bastings, M.M.C., Hermans, T.M., Spiering A.J.H., Kemps, E.W.L., Albertazzi, L., **Kurisinkal, E.E.**, Dankers, P.Y.W., Quantifying Guest-Host Dynamics in Supramolecular Assemblies to Analyze Their Robustness. *Macromol Biosci* 19, e1800296 (2019).

#### Extracurricular activities

- Ski, beach volleyball, badminton